Study of meso-scale reversed flow events in the polar ionosphere by SuperDARN radars

Master Thesis in Space Physics
by
Kristian Reed

June, 2017

University of Bergen

The University Centre in Svalbard

Department of Physics and Technology,
University of Bergen, Norway

Abstract

In this study we have investigated Reversed Flow Events (RFEs) in the northern hemisphere polar cap. A RFE is an ∼50-250 km wide flow channel that opposes the large scale background flow. A total of 57 new RFEs were discovered using data from the Super Dual Auroral Radar Network (SuperDARN) for primarily December of 2014-2016. We found RFEs lasting up to 97 minutes, with an average duration of 11.4 minutes.

Most RFEs were found in the dawn and dusk region with 26 events in the 4-10 MLT dawn region (46%) and 14 in the 14-20 MLT dusk region (25%). 12 RFEs were identified within the 10-14 MLT dayside region (21%) and only 5 in the 20-04 MLT nightside region (9%). There was no significant spread in MLT based on IMF B_z, but in our study 79% of the RFEs with stable IMF prior to onset were observed during positive IMF B_z. For B_y there was a strong preference towards dawn and night for negative values, and day and dusk for positive values. Most RFEs were seen stationary during their existence, while at least one RFE moved poleward.

Depending on their location we have classified the reversed flow channels as either dayside RFEs, lobe cell RFEs (dawn and dusk) or nightside RFEs. Our findings agree with previous studies of dayside reconnection generated RFEs, but expand our knowledge of the phenomenon to a wider area of the polar cap.

Acknowledgements

This Thesis is the result after two years of Master study at the Department of Physics and Technology at the University of Bergen, Norway. The first year was focused on mandatory courses in electromagnetism and space physics, while the second was fully devoted to this thesis project.

I feel very privileged to have Prof. Kjellmar Oksavik as supervisor for my master due to his incredible support and encouragement during this research. Although I was told to find my own research topic and relevant literature, Kjellmar was always there guiding me when I met obstacles. Many of the ideas and work of this thesis is also a result of hourly long discussions of how to interpret my newest results and diagrams.

For help with software questions and data presentation I want to thank Dr. Christer van der Meeren, a recent PhD graduate at UiB.

I want to thank my family and friends for providing me support and encouragement in times of hard work and challenges. A special thanks to my fellow Space Physics master students for good discussions and a thriving learning environment.

The topic of this thesis was the result of spending the whole spring semester in 2016 at UNIS in Svalbard. Many thanks to highly motivated professors and students there that made my stay valuable and enriching. The landscape and nature at 78° north is also an experience for life.

I want to give a special thanks to Dr. Thomas Immel at the Space Sciences Laboratory for inviting me to do 4 months of my research at The University of California, Berkeley during the autumn of 2016. Their knowledge and expertise has been priceless for my research. Spending time in the US during the 2016 American Presidential Election was also something I will never forget.

I also want to thank my friends and colleagues Norah Kwagala and Katie Herlingshaw for the help with proofreading this thesis. I'm very thankful for your efforts.

Lastly I acknowledge the following agencies and institutions for providing valuable data and documentation for my research:

- **Virginia Tech** Providing SuperDARN data and the DaViTpy software toolkit that my research is based upon.
- **The National Aeronautics and Space Administration (NASA)** Goddard Space Flight Centre's OMNIWeb service providing Solar Wind and IMF conditions and the SSCWeb service for providing orbital spacecraft trajectories.

- **National Oceanic and Atmospheric Administration (NOAA)** Providing POES MEPED particle precipitation data.
- **European Space Agency (ESA)** Providing SWARM Level 2 Field-Aligned Current data.
- **John Hopkins University Applied Physics Laboratory (JHU/APL)** Providing DMSP SSUSI Ultraviolet auroral imaging data.

Kristian Reed

Bergen, June 2017

Contents

List of Abbreviations

AACGM	Altitude Adjusted Corrected Geogmagnetic Coordinates
ACF	Autocorrelation Function
CRB	Convection Reversal Boundary
DMSP	Defence Meteorological Satellites Program
EISCAT	European Incoherent Scatter
EUV	Extreme Ultraviolet
FUV	Far Ultraviolet
FAC	Field Aligned Current
FOV	Field Of View
FTE	Flux Transfer Event
GD	Gradient drift
GSM	Geocentric Solar Magnetospheric
GNSS	Global Navigation Satellite System
HFA	Hot Flow Anomaly
HF	High Frequency
IMF	Interplanetary Magnetic Field
ISR	Incoherent Scatter Radar
KH	Kelvin-Helmholtz
MEPED	Medium Energy Proton and Electron Detector
MHD	Magnetohydrodynamics
MLAT	Magnetic Latitude
MLT	Magnetic Local Time
OCB	Open Closed field line Boundary
PIF	Pulsed Ionospheric Flow
PMAF	Poleward Moving Auroral Form
RFE	Reversed Flow Event
SuperDARN	Super Dual Auroral Radar Network
TPA	Transpolar Arc
UT	Universal Time

Chapter 1

Introduction

With increased travel to Arctic regions, society is increasingly dependent on satellite based navigation and communication. As the sea ice extent in polar regions decreases, shipping routes through polar regions become more attractive for shipping companies. The number of flights in polar routes is expanding constantly, as our world gets more interconnected and there is more tourism and business between the western and eastern hemispheres. They all have in common that they are increasingly dependent on reliable real-time communication and navigation services to assure safe travel.

Common for all satellite-based navigation and communication services is that the signal needs to traverse the ionosphere, the outer layer of our atmosphere. The ionosphere is very sensitive to disturbances from magnetic storms. These disturbances will in many cases create problems for GPS and other Global Navigation Satellite Systems (GNSS) to provide reliable navigation signals. In severe cases solar storms can cause satellites to malfunction and even cause power grids on earth to fail [*Daglis*, 2012].

In this thesis, we will study one type of ionospheric disturbance called Reversed Flow Events (RFEs). These events may be a trigger for smaller scale irregularities which cause the above mentioned navigation and communication issues. That is one motivation for advancing our knowledge about the occurrence, characteristics and importance of RFEs.

Some unanswered fundamental questions are how RFEs are generated, where they are found, and their role for energy transfer in the magnetosphere-ionosphere system. The RFE channels themselves are a meso-scale phenomena, and in the magnetosphere-ionosphere system different spatial scales play a role:

Large scale Important to understand the ionospheric response of magnetic reconnection and solar wind forcing. Relevant for determining position and direction of global ionospheric current systems.

Meso scale Relevant for understanding flow patterns in the polar cap ionosphere and it's connection to other physical phenomena such as ion-upflow, PMAF, RFE and other transients in the ionosphere.

Small scale Important for development of instabilities, which create scintillation in GNSS signals. Increasingly important since GNSS and radio communication is widely used in polar regions.

1.1 Objectives

Listed below are key scientific questions that will be investigated in this thesis.

- Where can reversed flow channels be found, and how long do they last?
- Under which interplanetary magnetic field conditions are RFEs observed?
- What is the connection between magnetic local time and RFE occurrence?

These questions are also fitting well into the overall goals of the research group at the Birkeland Centre for Space Science (BCSS) that me and my supervisor are a part of. The overall objective of this group is to answer the question: *How do we get beyond the large-scale static picture of the ionosphere?*. Our goal of identifying transient ionospheric flow channels is therefore part of the core mission that researchers here in Bergen and around the world is working on. In that sense it shows that the objectives of this thesis is relevant and connected to the work of the rest of the space physics community.

To address these questions, we will use case studies and data from a range of ground based and satellite instruments.

The theory presented in the next chapter, and the instruments and spacecraft used in the following chapter are all part of the necessary toolbox needed to answer these questions which have been driving our research. After presenting our results, we will discuss some aspects around the fundamental questions including the physical phenomena responsible for reversed flows. At the end we will look at our result in a larger perspective and attempt to categorize the RFEs based on generation mechanism.

Chapter 2

Theory

In this chapter we will provide a background in space physics for the topics covered in this thesis. The reader is assumed to have basic knowledge of plasma physics and magnetohydrodynamics to understand the content of this thesis. For a general introduction of space physics the reader is advised to *A Brief History of Solar-Terrestrial Physics* by *Kivelson and Russell* [1995].

First we will introduce the energy transfer from the Sun to the Earth environment. Then, the structure of the ionosphere and the coupling to the magnetosphere will be explained. Afterwards the polar cap ionospheric convection patterns will be described before different types of flow channels will be presented. The reversed flow channels will be described in more detail before potential generation mechanisms for Reversed Flow Events (RFE) are discussed.

2.1 The Sun and solar wind

The ionospheric phenomenon of RFE is believed to have its origin in the energy from the solar wind. Therefore, we will first introduce a short overview of how this energy is transferred to the Earth's ionosphere.

The Earth has an average distance of 149 million km to the sun, which corresponds to about 500 s or 8.3 min with a light speed of $c = 3 \times 10^8$ m/s.

Due to the high temperatures of over 2 million °K in the outer corona of the Sun, the gravitational force cannot hold back the ionised plasma particles. These particles will be released from the Sun in the form of the Interplanetary Magnetic Field (IMF) and solar wind plasma consisting of mostly electrons, protons and alpha particles with thermal energies between 1.5 and 10 keV. The solar wind particles moving with the magnetic field has a velocity normally ranging from 400-750 km/s [e.g.,., *Feldman et al.*, 2005]. Due to the Sun's rotational period of 27 days, the solar wind will appear to be travelling in the shape of a spiral called the Parker spiral after the astrophysicist Eugene Parker, which in his work *Parker* [1958] predicted the shape of the IMF. After leaving the Sun, the solar wind with embedded magnetic field will move with the speeds previously mentioned and travel for ∼2 - 4 days before it reaches the Earth's magnetosphere. An illustration of the solar wind arriving at the Earth is shown in Figure 2.1.

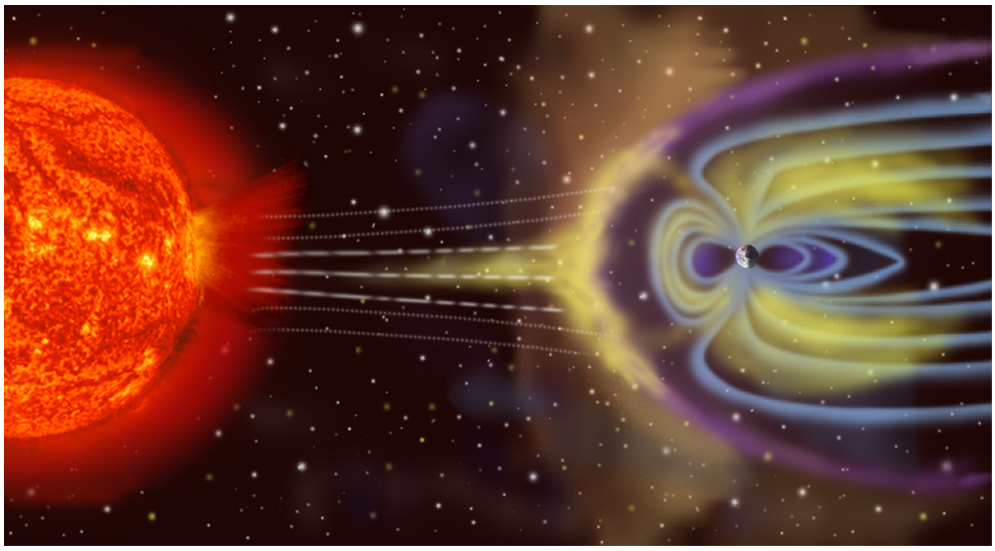

Figure 2.1: Artist illustration of the solar wind arriving the Earth's magnetosphere [from `http://sci.esa.int/jump.cfm?oid=41473`, downloaded on 30 January 2017]

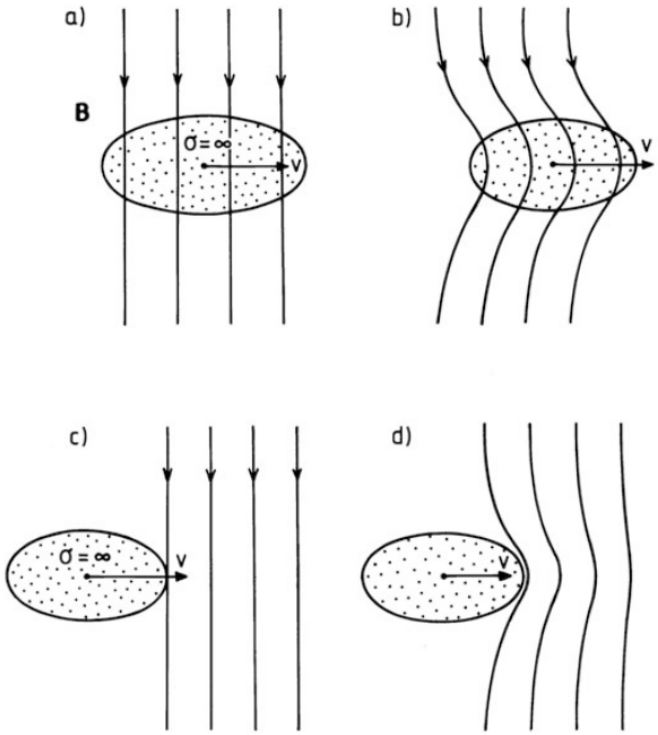

Figure 2.2: Illustration of the frozen-in field concept. In a-b we see how the magnetic field lines will bend as the plasma moves, and in c-d the fields cannot penetrate the highly conducting plasma and is pushed ahead of it [from *Brekke*, 2013].

2.1.1 Frozen-in magnetic field

The solar wind plasma is highly conducting, which results in something called the frozen-in magnetic field [*Alfvèn*, 1942].

If a particle is moving with a speed $\mathbf{v}$ in a rest frame S with electric and magnetic fields $\mathbf{E}$ and $\mathbf{B}$, the fields in a reference frame S' moving with the particles will then be:

$$\mathbf{E'} = \mathbf{E} + \mathbf{v} \times \mathbf{B} \tag{2.1}$$

and

$$\mathbf{B'} = \mathbf{B} - \frac{\mathbf{v} \times \mathbf{E}}{c^2}. \tag{2.2}$$

Since the conductivity of the plasma $\sigma \to \infty$ we have by Ohm's law that there is no current, and in the moving reference system $\mathbf{E'} = \mathbf{0}$. This gives us

$$\mathbf{E} = -\mathbf{v} \times \mathbf{B}, \tag{2.3}$$

which is called the frozen-in condition. By inserting this into Faraday's law it can be shown that the magnetic field follows the plasma motion perpendicular to the field lines and vice versa. An illustration of how the frozen-in concept works is shown in Figure 2.2.

This frozen-in condition explains how the Interplanetary Magnetic Field (IMF) is travelling together with the solar wind, and as we will see later, how the plasma in the Earth's upper atmosphere, the ionosphere, will be forced to move together with the field lines as they traverse the polar caps.

2.2 The Earth's magnetosphere

The magnetosphere is the area around the Earth governed by the magnetic field set up by the Earth itself. A sketch of the Earth's magnetosphere is shown in Figure 2.3.

The Earth is generating its own magnetic field that shields the surface from the otherwise harmful solar storms. According to the Dynamo theory [*Russell*, 1993] the flow of molten iron in the Earth's outer core is convecting and rotating due to Earth's rotation and thermal dissipation from the mantle. Due to this movement of the Earth's core, a magnetic field is created, which to a first order approximation is a dipole field, falling of as $1/r^3$ where r is the distance from the centre of the Earth.

Chapman and Ferraro [1931] introduced the concept of a magnetopause, the outermost layer of the magnetosphere. The magnetopause is located where the solar wind pressure equals the pressure from the magnetosphere, $\rho_{SW} v_{SW}^2 = 2B_{MS}^2/\mu_0$. Here, ρ_{SW} and v_{SW} are the density and speed of the incoming Solar wind, B_{MS} the Earth's magnetic field strength at the boundary and μ_0 the permeability in vacuum. The magnetosphere, which would look like a dipole field in free space, is largely compressed on the side facing the Sun and stretched on the side pointing away because of the influence from the solar wind, as seen in Figure 2.3. Because of this, the magnetopause will extend to around 65000 km, or 8-10 Earth radii on the dayside, and to several hundred Earth radii on the nightside.

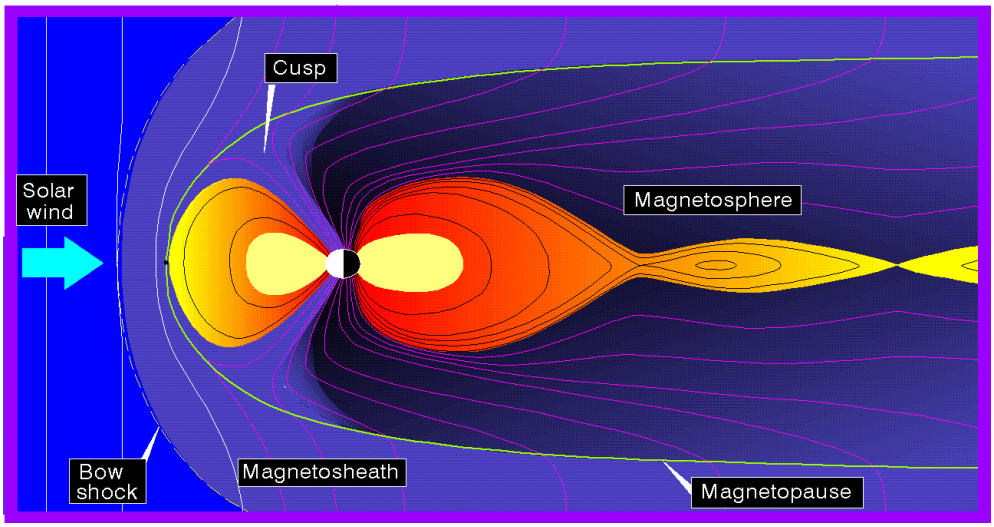

Figure 2.3: The Earth's magnetosphere. From the left we can see the bow shock, where the solar wind speed quickly drops, and the magnetopause, where the Earth's magnetospheric pressure equals the one from the solar wind. Between the bow shock and the magnetopause we have the magnetosheath which is characterized by a weaker magnetic field that the solar wind can penetrate. [From `http://image.gsfc.nasa.gov/poetry/magnetism/magnetism.html`, downloaded on 17.01.2017]

While the magnetic field strength on the Earth's surface is well mapped, it is still poorly understood how the magnetic field changes over time and what processes contribute [*Roberts et al.*, 2013]. Even though the Dynamo theory is thought to be the dominating process, we still have little knowledge of the composition of the Earth's core, which makes it hard to make numerical simulations of the convection processes taking place. How the shape of the magnetosphere looks is also strongly dependent on how the magnetosphere interacts with the solar wind, which is also not fully understood. The satellite mission Cluster mission launched in 2000 has answered a lot of these questions due to its unique ability to measure plasma fluctuations in three dimensions. A summary of the scientific highlights up until today can be found in *Escoubet et al.* [2015]. Recently another four spacecraft satellite mission, the Magnetospheric Multiscale (MMS) launched in 2015 aims to solve some of the many still unanswered questions. One of the most important goals of MMS is to conduct a definitive experiment to determine what causes magnetic field lines to merge in a collisionless plasma [*Burch et al.*, 2016].

Table 2.1: Common properties of the different layers of the dayside ionosphere [*Johnson*, 1969].

Region	Altitude[km]	Density[m^{-3}]
D	60-90	$10^8 - 10^{10}$
E	90-150	$10^{10} - 10^{11}$
F	150-600	$10^{11} - 10^{12}$

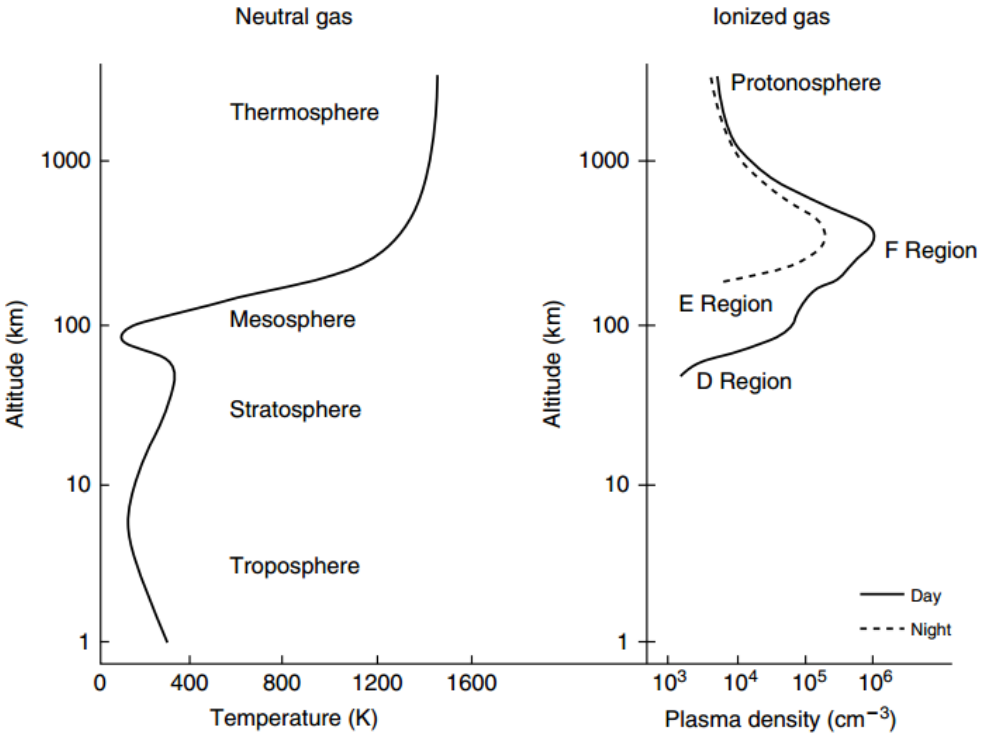

Figure 2.4: Temperature in different height intervals of the atmosphere, and density profiles of the ionosphere for different layers. The density profile shows higher density at day in solid line compared to night in dashed line due to solar UV ionization [from *Kelley*, 2009].

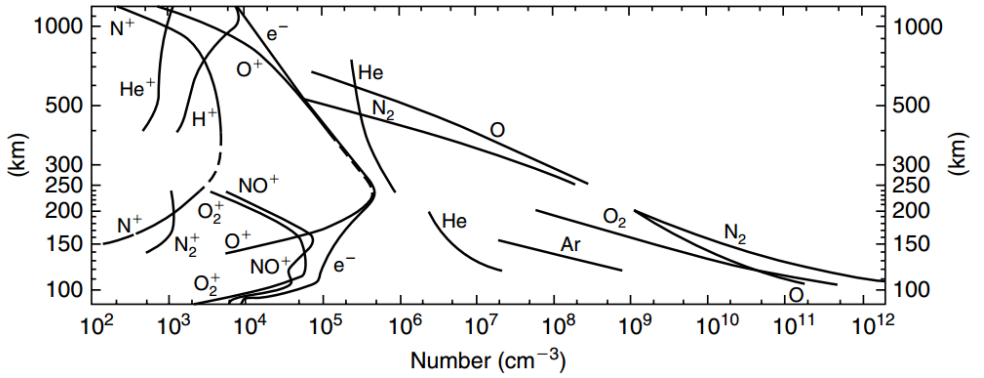

Figure 2.5: Density of different elements of both neutral and charged particles in the atmosphere for different heights. Note that even with high ion density from 100-500 km, there are still more neutral particles than charged ones [from *Johnson*, 1969].

2.3 Ionosphere

The upper part of the Earth's atmosphere is called the ionosphere, and it ranges from about 60 km up to ∼1000 km. The ionosphere is characterised by a significant portion of ionised plasma from solar Extreme UltraViolet radiation (EUV) radiation, compared to the lower part of the atmosphere. Production and loss varies with altitude, which results in different altitudes having different plasma densities. Due to equal production of positive and negative charges, the Earth's ionosphere will have charge neutrality on large scale. Because of this, the electron and ion densities will be equal and often referred to collectively as the plasma density.

The plasma frequency $\omega_p = \sqrt{N_e e^2/m_e \varepsilon_0}$, where N_e is the above mentioned plasma density, e the elementary charge, m_e the electron mass and ε_0 the permittivity in vacuum, is an important property to determine the characteristics of the ionosphere. Because of its electron density dependency, radiowaves sent into the ionosphere will be reflected at the altitude where the signal frequency is of the same order of magnitude as the plasma frequency. By using an ionogram that scans the ionosphere over a wide range of frequencies, the altitude at different layers of the ionosphere can be determined by the altitude of the backscattered signal of different frequencies. A plot of the average density of different layers of the ionosphere can be seen in Figure 2.4. Figure 2.5 shows the individual density profiles of the different particle species in the upper atmosphere.

The F region is the uppermost region of the ionosphere and typically contains the maximum plasma density. For this thesis, the F region between 150 - 400 km is the most important region. Key properties of the different regions of the ionosphere can be seen in Table 2.1.

2.4 Solar wind energy transfer

If there was no magnetosphere and atmosphere around the Earth, all the solar wind plasma would have direct access to the Earth's surface. That is the case for the moon, and it is thought to be the reason for why there are no habitable conditions existing on Mars today [e.g., *Summons et al.*, 2011].

Even though Earth is shielded from most of the solar wind by the magnetosphere, there is still a coupling between the incoming solar wind magnetic field and the terrestrial magnetic field [eg. *Burch and Drake*, 2009]. Several theories have been put forward for how the particles and magnetic fields from the seemingly repelling magnetosphere are injected into the Earth's ionosphere as described by e.g., *Dungey* [1961], *Cowley and Lockwood* [1992], *Burch et al.* [2016] and *Trenchi et al.* [2016].

When the incoming solar wind magnetic field is antiparallell to the terrestrial magnetic field, the field lines will merge is a process called magnetic reconnection first described by *Sweet* [1958]. A close up illustration of how magnetic field lines reconnect is shown in Figure 2.6. Here, oppositely directed field lines from left and right will merge at t=0 and convect up and downward. Usually this happens when there is a strong southward IMF component (pointing in the negative Z-direction in GSM coordinates, as described in Appendix A.1) in the solar wind, and the interplanetary magnetic field lines will be oppositely directed to the Earth's magnetic field lines. Here the field lines from IMF will reconnect with the terrestrial field lines close to the dayside magnetopause. This phenomena of static reconnection is shown in the red areas

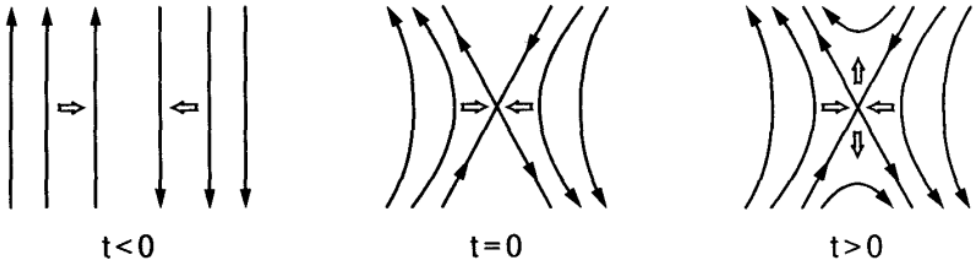

Figure 2.6: Close up sketch of the phenomena of magnetic reconnection. Black long arrows indicate magnetic field lines, and the short ones movement of the field lines. We see that at t=0 field lines coming from left and right will merge and move up and downwards in the diagram for t>0 [Figure from *Baumjohann and Treumann*, 1999].

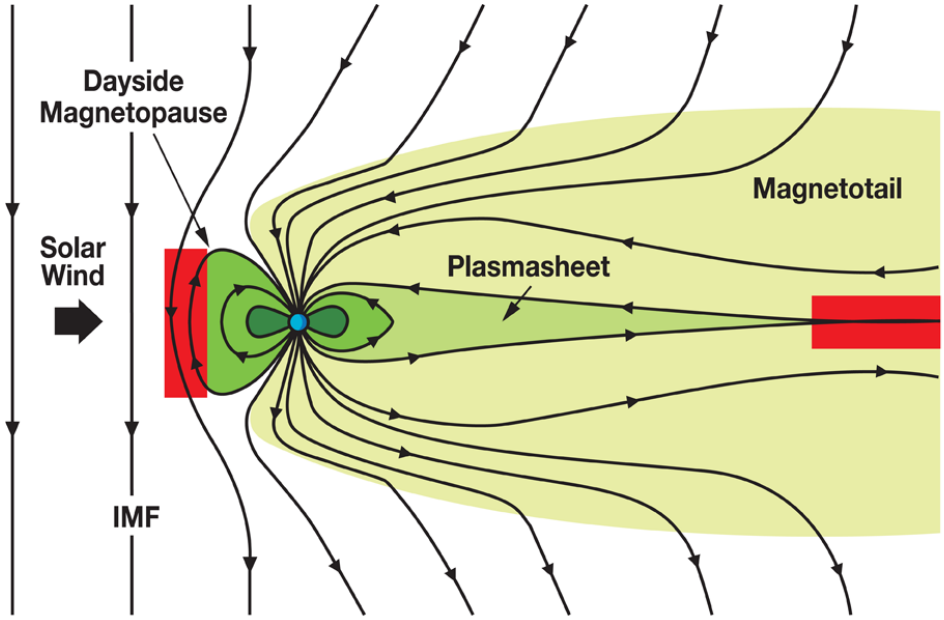

Figure 2.7: Magnetic reconnection for southward IMF. From the left we see the solar wind and IMF reconnecting in the left red area at the dayside magnetopause. As the open field lines convect over the polar cap they reconnect in the nightside magnetotail and become closed again [from `https://mms.gsfc.nasa.gov/science.html` downloaded on 17 January 2017].

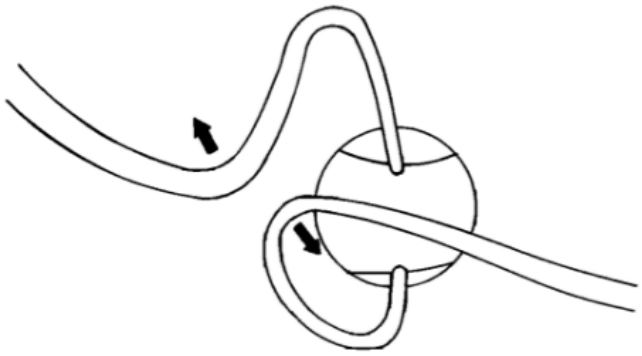

Figure 2.8: Magnetic Flux tubes in the northern and southern hemispheres created by a localized burst of reconnection near the magnetopause [from *Southwood*, 1987].

in Figure 2.7.

2.4.1 Static reconnection

Early attempts to explain the large scale convection of plasma in the polar cap ionosphere were presented as a result of dayside magnetopause reconnection by *Dungey* [1961]. Here, a static picture of uniform convection of magnetic flux over the polar cap takes place. This is called the Dungey cycle. Because of the frozen-in magnetic field concept, the plasma in the ionosphere will follow the movement of these reconnecting field lines [eg. *Volland*, 1978]. In the nightside magnetotail the open field lines will be closed by reconnection again, see Figure 2.7, and the magnetic field lines are forced back to the dayside because of continuity [*Dungey*, 1961].

Ionospheric convection is attributed to magnetic reconnection between the geomagnetic and Interplanetary Magnetic Field and is dependent on the IMF orientation [*Cowley and Lockwood*, 1992]. Reconnection in the dayside magnetopause creates "open" magnetic flux that is connected to the solar wind magnetic field. For the steady state approach an equal amount of open field lines later reconnects in the cross tail current sheet which re-closes the magnetic flux. This model describes a steady convection of plasma in the F-region ionosphere for quiet solar wind conditions. This model for the ionospheric convection was retained for decades since it was difficult to challenge the theory with limited remote or in situ measurements.

2.4.2 Transient reconnection

As radar and satellite measurements became available, it was observed from the ISEE satellite observations that the reconnection process didn't precede exactly constant and steady. *Russell and Elphic* [1978] noticed rapid bipolar oscillations in the component of the magnetic field perpendicular to the magnetopause. They interpreted this as a result of the reconnection process being impulsive, giving rise to the phenomena called a Flux Transfer Event (FTE). *Russell and Elphic* [1978] interpreted the perturbations as spatially and temporally localized reconnection events. The location of FTEs is highly dependent on the IMF orientation, but they are most often observed during southward IMF [e.g., *Wang et al.*, 2006]. FTEs can further be classified by whether they are happening in the magnetosheath or at the magnetopause. As the IMF field

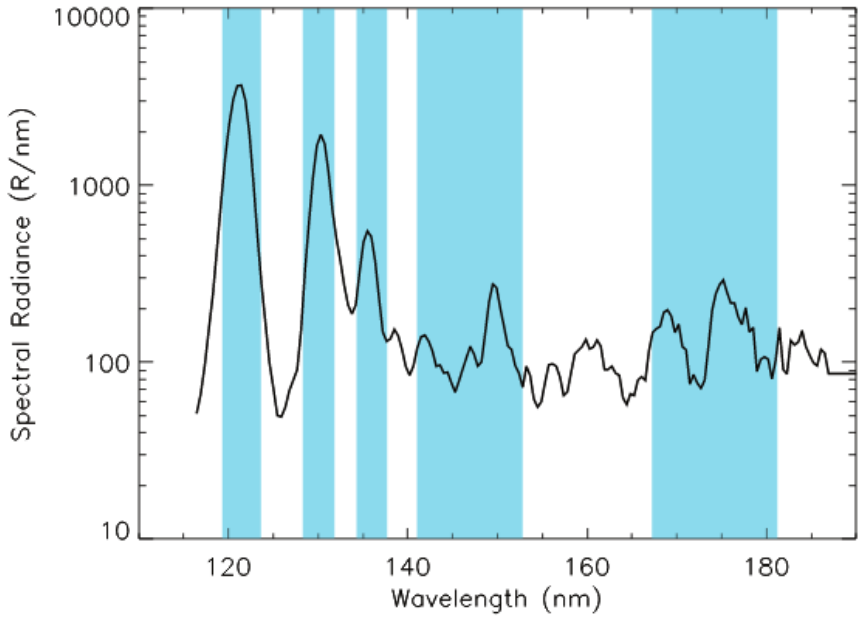

Figure 2.9: The radiance of the FUV aurora from the TIMED spacecraft, which uses the same instrument as that on DMSP that we use data from. The blue shading shows the passbands of the detector which matches the peak emission lines [from *Christensen et al.*, 2003].

lines connect to the terrestrial ones, which give rise to a flux tube connecting to the northern and southern hemispheres [*Paschmann et al.*, 1982], see Figure 2.8. In the ionosphere the signature can be seen as an equatorward bulge in the boundary between the open and closed flux [*Southwood*, 1987].

With increasing computational powers, magnetohydrodynamics (MHD) simulations have been performed to investigate the generation mechanisms of FTEs. *Dorelli and Bhattacharjee* [2009] used such a model to investigate whether FTEs can form under steady IMF conditions. Their simulations concluded that FTEs can form spontaneously under southward IMF conditions which makes the magnetosphere unstable, but not for northward IMF.

Further development in sensing of the ionosphere supported the theory of nonsteady reconnection. *Cowley and Lockwood* [1992] presented an enhanced ionospheric convection model where pulsed reconnection enhances the plasma flow over the polar cap. This explains how the convection will change in response to differences in the IMF B_y and B_z components, and indeed isn't steady as *Dungey* [1961] proposed.

2.4.3 The Aurora

Although optical observations of auroral emissions is not a significant part of this thesis, we will use the imagery of ultraviolet (UV) aurora to determine the location of the open closed field line boundary (OCB) in the polar cap. The OCB is the boundary where equatorward magnetic field lines are connected to the Earth in both hemispheres, and poleward field lines are only connected to the Earth on one side (and the IMF on the other side). Thus, we need a brief introduction to the production of auroral emissions.

Electrons and protons causing the visible aurora will precipitate along the magnetic field lines towards the magnetic poles of the Earth [e.g., *Arnoldy*, 1974]. When they

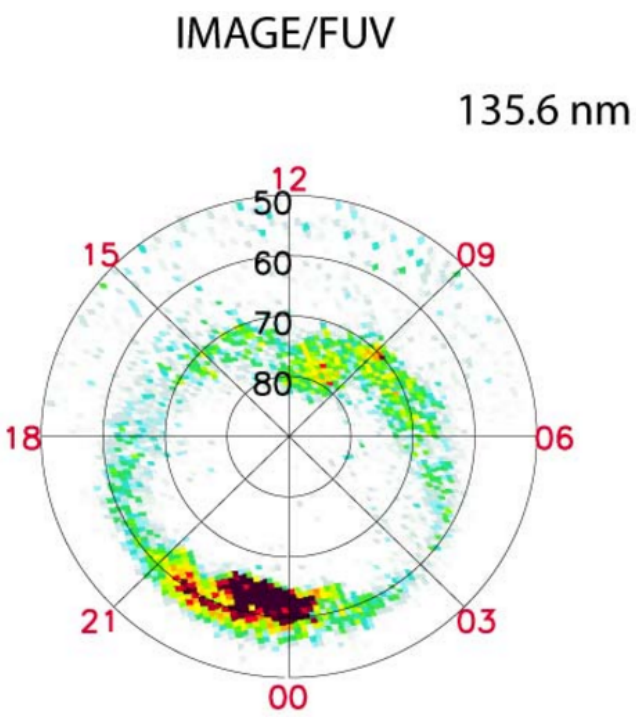

Figure 2.10: FUV aurora seen in the northern hemisphere by the IMAGE satellite. Red denotes stronger aurora, and the projection is MLT coordinates with noon pointing up [from *Østgaard et al.*, 2005].

reach the ionosphere they will excite neutral molecules and atoms. It is when these exited molecules relax to lower energy state that photons are produced, with wavelengths dependent on the energy level of excitement. The auroral oval is a good way to identify the OCB, due to the precipitation region that is laying on the boundary [e.g., *Boakes et al.*, 2008]. As a result, we know that poleward of the auroral oval there will be open field lines.

Seen on the Earth's surface the two most common emission lines during particle precipitation are the 557.7 nm green line, and 630.0 nm red line originating from atomic oxygen excitation [e.g., *Störmer*, 1955]. These are produced when the atomic oxygen exited to 4.17 eV relaxes first to 1.96 eV emitting a photon of 557.7 nm giving green light, and then further relaxes down to the ground state by emitting a 630.0 nm red photon.

For our study, however, we will use the Far UltraViolet (FUV) emissions recorded by spacecrafts for full polar coverage. There are 5 FUV emission lines of interest, the atomic lines of Hydrogen (121.6 nm), Oxygen (130.4 nm and 135.6 nm) and two Lyman-Birge-Hopfield (LBH) emission lines for molecular N_2 at 140-150 nm and 165-180 nm [*Meier*, 1991], see Figure 2.9. LBH emissions result from collisions of high energy electrons and protons with molecular N_2 giving rise to emssions over a large range of wavelengths from 100-260 nm [*Lofthus and Krupenie*, 1977]. A more extensive study of UV auroral emissions can be found in e.g., *Meier* [1991], *Christensen et al.* [2003] and *Young et al.* [2010]. An image of the entire polar FUV auroral oval from the IMAGE spacecraft is shown in Figure 2.10.

Milan et al. [2003] did an extensive multi-instrument analysis of the OCB location

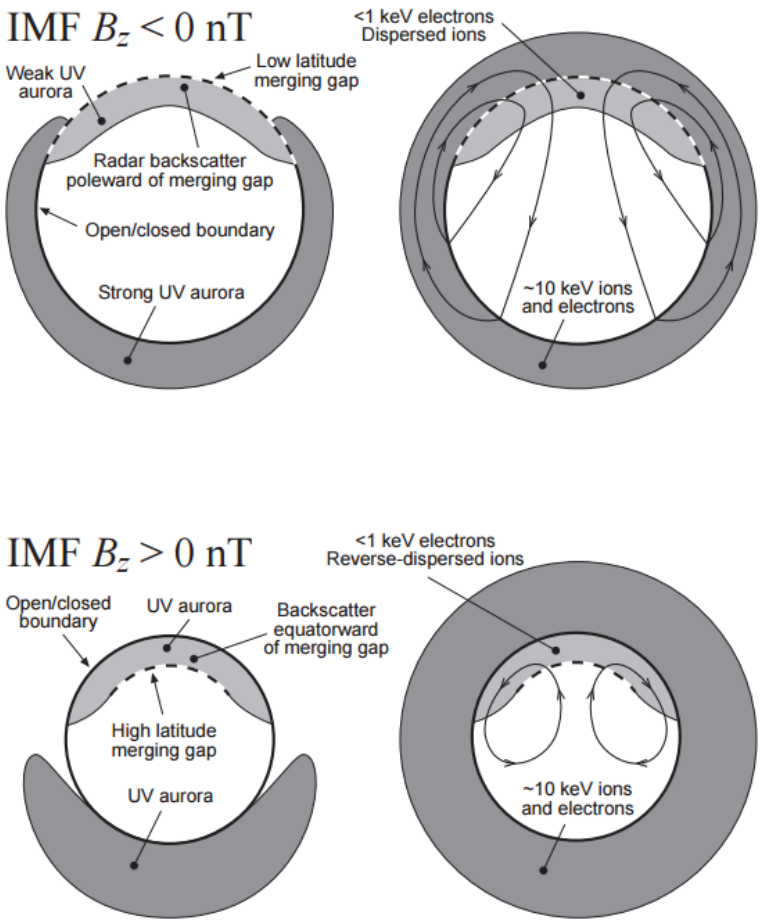

Figure 2.11: Location of the UV aurora in relation to the OCB for various IMF B_z directions. The left panels show the location of the UV aurora, while the right panels show the energy of precipitating particles in their respective locations. Noon MLT is up on the figure [from *Milan et al.*, 2003].

for various IMF conditions. Their findings are consistent with precipitation of low energy particles (< 30 keV) of magnetoheath origin on open field lines, and is also in good alignment with the poleward boundary of the UV auroral luminosity on the nightside. On the dayside the UV auroral intensity is generally weaker and swamped out by dayglow from the Sun, and lay either poleward or equatorward of the "merging gaps", which is the reconnection sites depending on the IMF direction. A schematic description of the location of UV aurora in relation to the OCB is shown in Figure 2.11.

2.5 Ionospheric convection and flow channels

Due to the frozen-in condition and low neutral density in the F region ionosphere, both electrons and ions will move in the same direction by the $\mathbf{E}\times\mathbf{B}$ drift. When the magnetic field lines move over the polar cap, the high latitude ionospheric plasma is forced to follow the convection of magnetic field lines [*Dungey*, 1961]. Initially this was thought to follow a steady pattern as described by the Dungey cycle and shown in Figure 2.12.

Later there has been extensive research about high latitude ionospheric convection

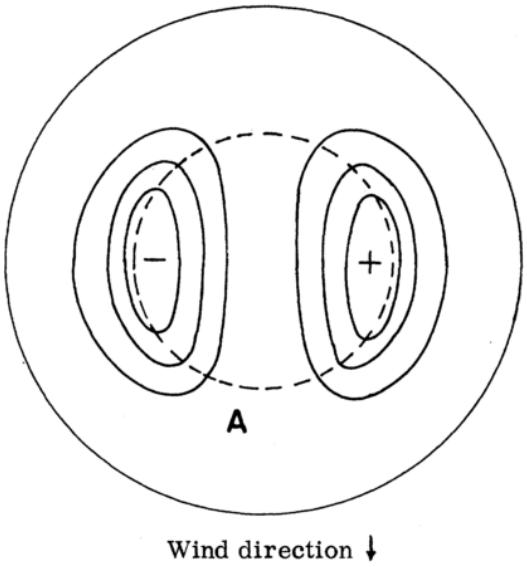

Figure 2.12: The static Dungey convection cycle for southward IMF. The view is from above the magnetic north pole, with 12 MLT on the top [from *Dungey*, 1961].

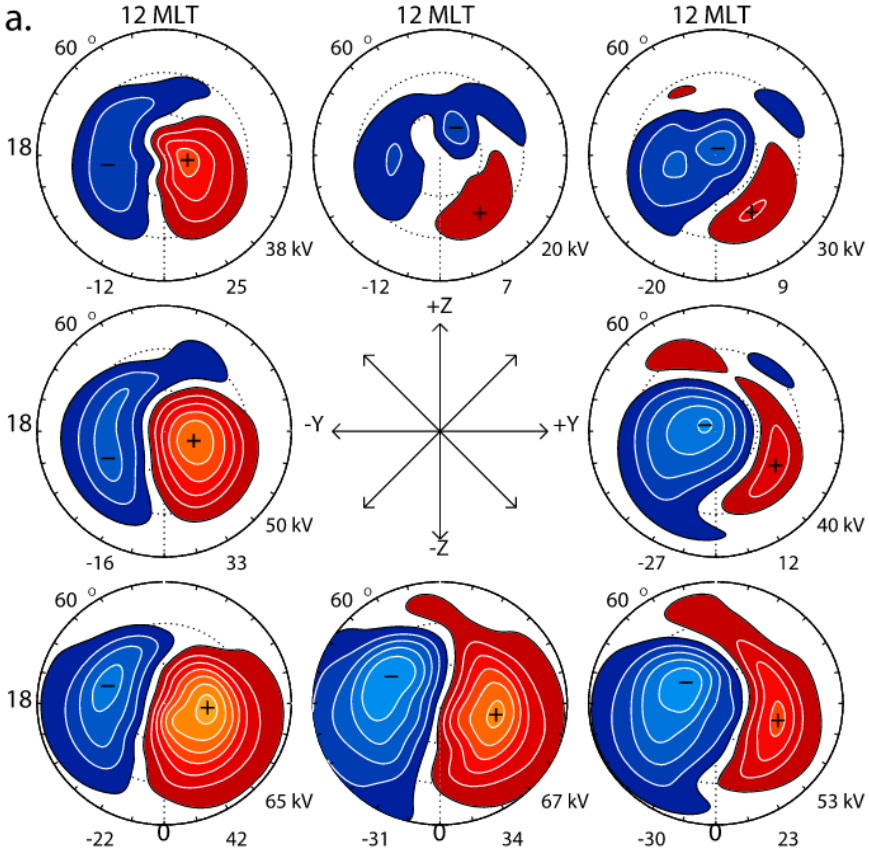

Figure 2.13: Average convection patterns and electric potential sorted by IMF clock angle in the northern hemisphere polar cap. The view is in MLT coordinates with noon up [from *Cousins and Shepherd*, 2010].

[e.g.,. *Heppner and Maynard*, 1987; *Cowley and Lockwood*, 1992; *Weimer*, 1995; *Ruohoniemi and Baker*, 1998; *Lester et al.*, 2006; *Cousins and Shepherd*, 2010]. The model by *Dungey* [1961] was primarily a qualitative model made by earlier observations of a regular interplanetary magnetic field by the Pioneer V of 1960. One of the best known empirical studies from literature came decades later, with electric field measurements from the DE-2 satellite of 1981 and described in *Heppner and Maynard* [1987]. Here equipotential lines from the electric field measurements were drawn for various orientations of the IMF. These equipotential lines in turn govern the plasma flow over the polar cap, due to the $\mathbf{E}\times\mathbf{B}$ drift of ionospheric plasma. Mathematical models based on spherical harmonics coefficients from the DE-2 mission have later been developed by *Weimer* [1995] for improved understanding of the dynamics of the system.

From being a purely static convection model, the ionospheric convection is now believed to be highly dynamic depending on the direction of the solar wind has as shown by *Cousins and Shepherd* [2010] in Figure 2.13. Here we can see the equipotential lines of the polar cap electric field for various IMF clock angle orientations based on long time statistical data of line of sight ion drift from the Super Dual Auroral Radar Network (SuperDARN) radars [*Greenwald et al.*, 1995; *Chisham et al.*, 2007]. The SuperDARN will be more extensively described in Chapter 3.1. The two cell convection model by *Dungey* [1961] is most closely represented by southward IMF and close to zero IMF B_y in the bottom centre panel of Figure 2.13.

For the plasma convection proposed by *Dungey* [1961] to occur on the dayside, there has to be inflow of open flux, which is open field lines from dayside reconnection (displayed as the dayside reconnection site in Figure 2.7), in the dayside cusp area. For variations in IMF B_y there will be a shift of the cusp inflow region in the dayside polar cap [e.g., *Heelis*, 1984; *Ruohoniemi and Greenwald*, 2005]. For positive IMF B_y the inflow region is shifted postnoon, and similarly prenoon for negative values.

From recent studies done by radar instruments it has been possible to show that inside this large scale convection pattern there are smaller non-uniform features such as Flow Channel Events (FCEs) which we will present more in depth [*Sandholt et al.*, 2004]. However, to understand this, we will first briefly describe the current systems going in and out of the ionosphere.

2.5.1 Magnetosphere-ionosphere current systems

We established in chapter 2.4.1 that the ionospheric flow is closely linked to magnetospheric reconnection. As a result of precipitating particles in the ionosphere, there will be set up currents which can be measured by magnetometers on the ground and in space. Kristian Birkeland wrote in 1908 about currents in the aurora [*Birkeland*, 1908], and these field-aligned currents have since been named the Birkeland currents. When there is strong reconnection in the magnetotail, the cross tail current will subsequently increase, which is the current connecting to the ionosphere in the nightside.

Due to high conductivity along magnetic field lines, currents will flow as poleward Region-1 [*Iijima and Potemra*, 1976] currents down to the ionosphere where they move over the polar cap ionosphere as Pedersen currents. The Region-1 current is then connected to another field aligned current system called the Region-2 current closing at somewhat lower latitudes via the partial ring current, see Figure 2.14. As electrons have higher mobility and will move faster than the heavier ions, there will be created a second horizontal current, the Hall current from the $\mathbf{E}\times\mathbf{B}$ drift of the electrons, but

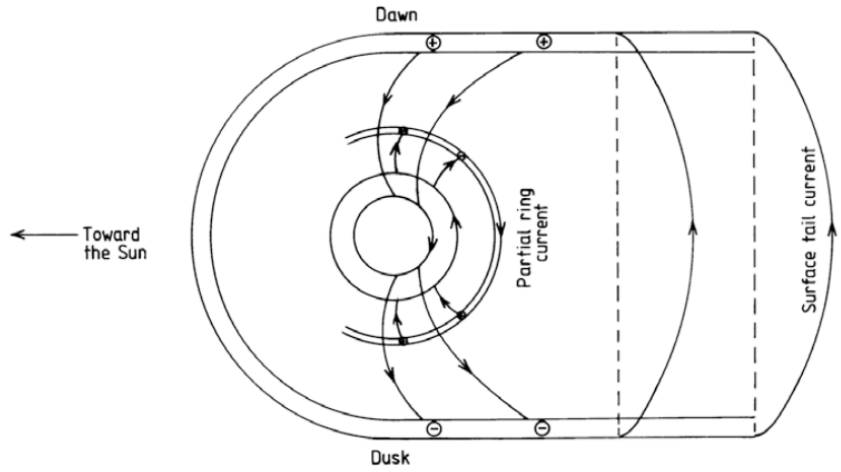

Figure 2.14: A possible closure of the magnetosphere-ionosphere current system. Region-1 currents flow from the outer magnetosphere to the poleward boundary of the ionosphere as Region-1 currents. The Region-2 currents from the partial ring current arrive in the ionosphere at lower latitudes [from *Brekke*, 2013].

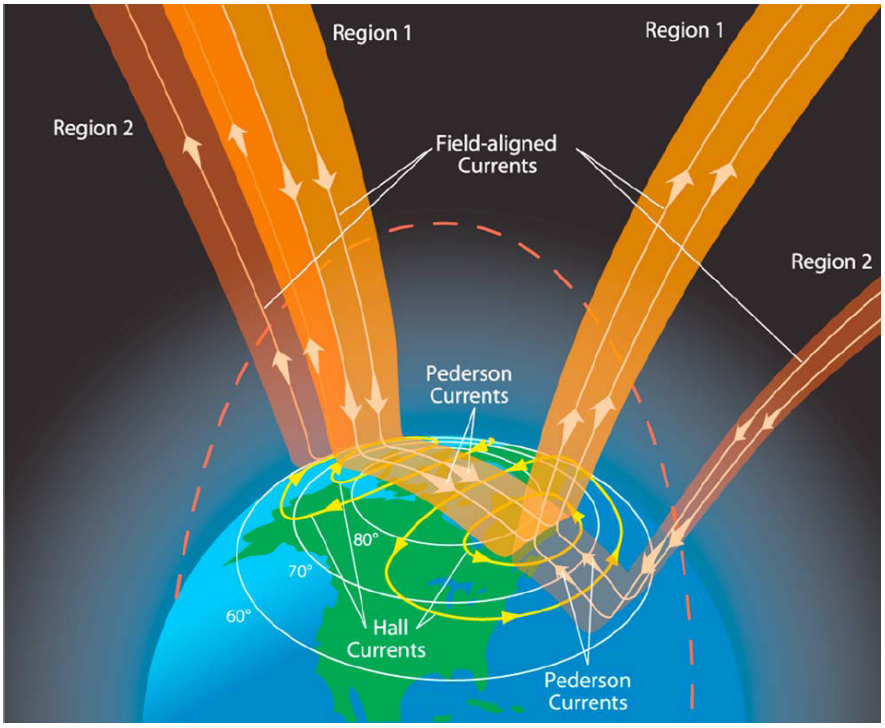

Figure 2.15: A schematic view of how the currents from Figure 2.14 map down to the Earth. We see the innermost Region-1 currents which are closed in the tail-current, and the Region-2 current closed in the partial ring current [from *Le et al.*, 2010].

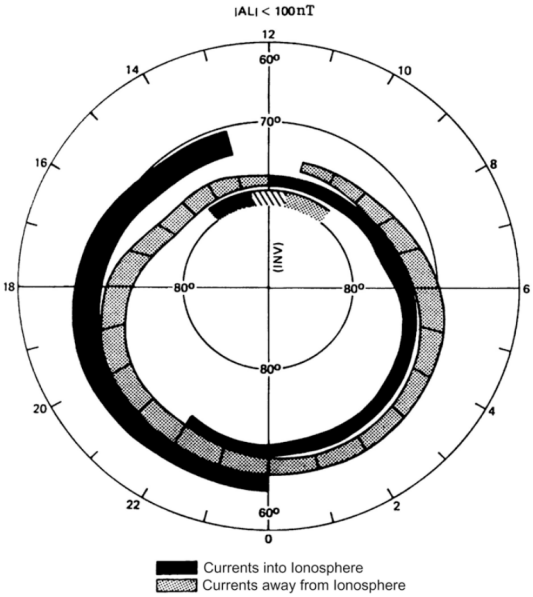

Figure 2.16: Average currents into and out of the ionosphere for southward IMF. The innermost currents, into the ionosphere on the morning side, and out of the ionosphere on the evening side corresponds to the Region-1 currents in Figure 2.15, and the outermost is the Region-2 currents [from *Iijima and Potemra*, 1976].

in the opposite direction. The Hall current, which is an important contribution to the auroral electrojet, is visible in ground magnetometers around magnetic midnight travelling eastward pre-noon and westward post-noon [*Le et al.*, 2010]. An illustration of the ionospheric currents can be seen in Figure 2.15, while the location of Region-1 and Region-2 currents into and out of the polar cap ionosphere is shown in Figure 2.16.

2.5.2 IMF dependency of convection

For IMF $B_z \ll 0$ (pure southward), the ionospheric convection is relatively well understood with two large convection cells as described by *Dungey* [1961].

When the IMF $B_z \gg 0$ (pure northwards), the ionospheric convection pattern diverges from the usual two cell convection. Depending on the magnitude of the magnetic field, and in particular the B_y component, several additional convection cells may be created. This has to do with the fact that for northward IMF reconnection does not take place in the equatorial plane (in the red area to the left in Figure 2.7). *Reiff and Burch* [1985] carried out statistical work for various IMF conditions from the Dynamics Explorer spacecraft mission from 1981 to study the ionospheric interaction with reconnection in the magnetosphere. Their findings can be seen in Figure 2.17. For northward IMF, reconnection will take place further downstream in the magnetosphere and closer to the magnetic poles. When IMF B_y is close to zero we get what is called dual lobe reconnection, caused by simultaneous reconnection in both hemispheres and closing of open field lines in the polar cap [*Imber et al.*, 2006]. This results in separate lobe cells in the convection pattern as seen in panel (B) of Figure 2.17. For IMF B_y strongly positive or negative we will instead get single lobe reconnection as seen in panels A and C of the same figure. However, it is important to notice that the convection patterns are only statistical results, and not necessary the actual instantaneous convection pattern

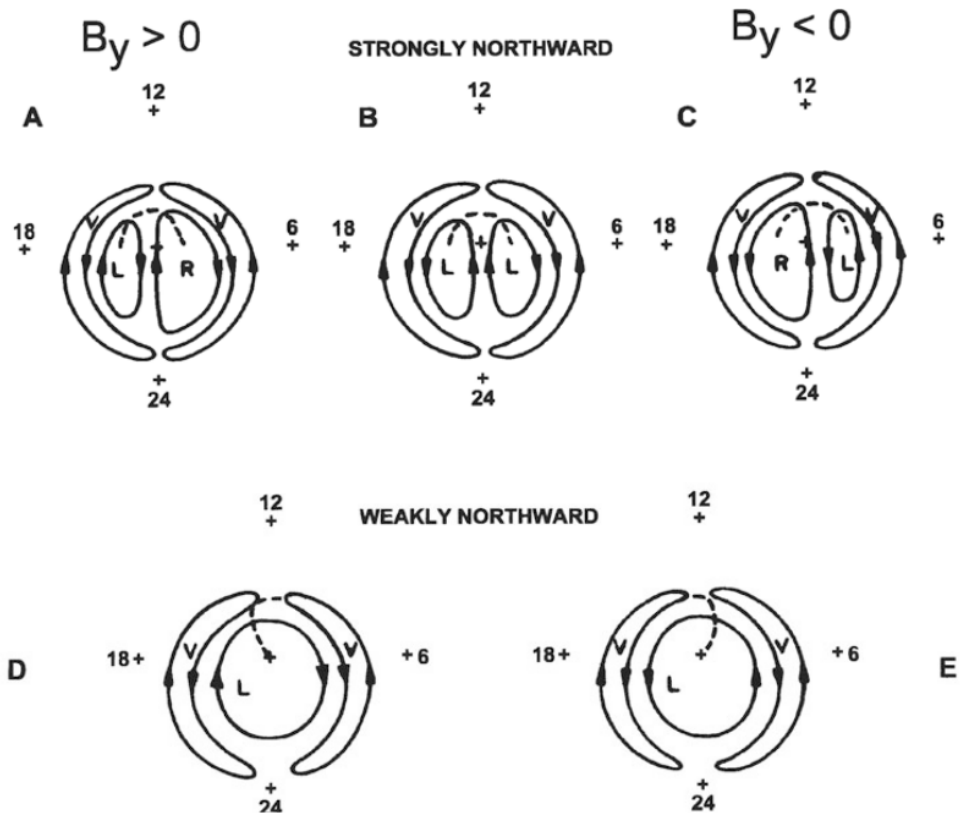

Figure 2.17: Schematic ionospheric convection cells in the northern hemisphere for positive and negative IMF B_y during weakly and strongly northward IMF ($B_z > 0$). We see that there are single lobe cells developing during weakly northward IMF in panel (D) and (E), and dual lobe cells during strongly northward marked with 'L' in (A) and (C) [from *Reiff and Burch*, 1985].

for a given event since statistics tend to eliminate deviations.

As we will see later in our results, such lobe cells may in fact generate a large portion of the observed reversed flow channels. A schematic view of lobe cell reconnection is shown in Figure 2.18. Optical and ground based radar measurements of the resulting sunward flow channels have later been studied by e.g., *Sandholt et al.* [1998] and *Liu et al.* [2015].

2.5.3 Dayside flow transients

Ionospheric signatures of Flux Transfer Events (FTE) have been observed since the beginning of European Incoherent Scatter (EISCAT) observations by *van Eyken et al.* [1984]. A description of EISCAT's working principles and characteristics can be found in *Rietveld et al.* [1991]. The signatures, often referred to as poleward moving transients [*Sandholt et al.*, 1990], are commonly divided into Flow Channel Events (FCE) [*Pinnock et al.*, 1993], Pulsed Ionospheric Flows (PIFs) [*Provan et al.*, 1998] and Poleward Moving Radar Auroral Forms (PMRAFs) [*Milan et al.*, 2000].

During daytime aurora *Sandholt et al.* [2004] categorized three types of enhanced flows found together with daytime aurora. This includes (i)*Enhanced sunward return flow on closed field lines*, (ii)*Enhanced flow on newly opened flux containing FTEs* and (iii)*Enhanced flow on old open field lines due to the solar wind magnetosphere dynamo*

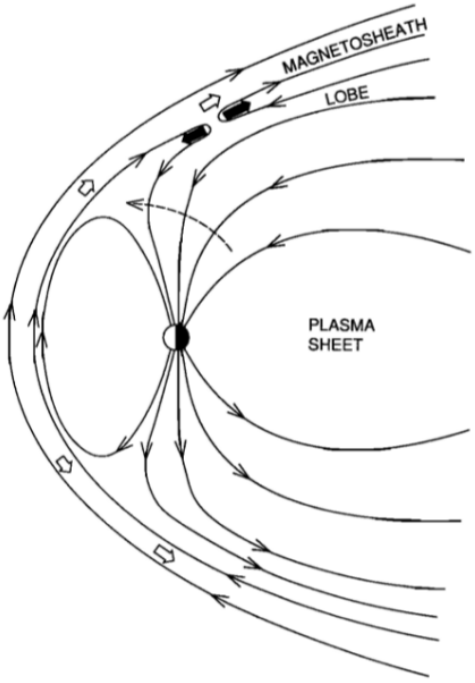

Figure 2.18: Reconnection in the northern lobe during positive IMF B_z. Solid lines mark the magnetic field lines, and dashed arrow marks the sunward flow direction of the plasma flow [from *Gosling et al.*, 1991].

in the high latitude boundary layer. All these flow types are somewhat connected since they contain enhanced flow in the same direction as the large-scale flow pattern.

These different types of enhanced flow will now be examined in greater detail.

i) Enhanced flow on closed field lines

Lockwood et al. [1993] used the EISCAT VHF radar to locate channels of sunward return flow on closed field lines. The 630.0 nm meridian-scanning photometer in Ny-Ålesund was used to follow the flow channels. *Moen et al.* [1995] did similar observations, and managed to measure a flow vector, see Figure 2.19. They observed this return flow at lower latitudes in both the morning and afternoon sector and attributed the cause to pulsed reconnection on the magnetopause.

ii) Enhanced flow on newly-opened field lines

Southwood [1987] presented a model for how the ionospheric footprint of an FTE would look like. According to that model, newly reconnected fast moving flux will set up a local twin vortex flow disturbance, see Figure 2.20. There will be an upward Field-Aligned Current (FAC) at the clockwise flow shear, and a downward FAC at the counter clockwise flow shear, and the two are connected via a horizontal Pedersen current.

For the Southwood model there should be at least three observable signatures; (1) newly open fast moving centre flux, (2) FAC on the flanks of the newly opened flux, and (3) return flow on either side.

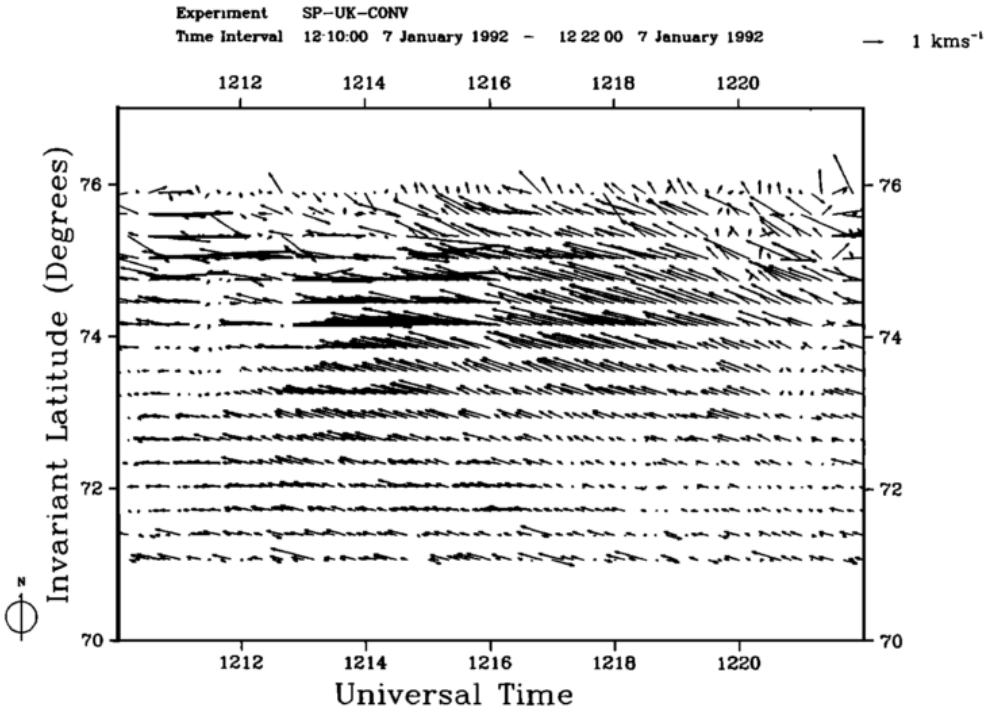

Figure 2.19: EISCAT VHF flow vectors derived by combining line of sight velocities from Beam 1 and Beam 2 showing enhanced sunward return flow on closed field lines. The plot shows the time developement of flow vectors at different latitudes. The lower latitudes are a part of the background flow, while the enhanced flow can be seen at higher latitudes in the top of the diagram [from *Moen et al.*, 1995].

iia) Flow Channel Events (FCEs) *Pinnock et al.* [1993] presented several transient velocity patterns in the cusp ionosphere. Polar Anglo-American Conjugate Experiment (PACE) HF radar data were used in combination with DMSP F9 polar orbiting satellites to measure channels of at least 900 km length in the anti-sunward direction and 100 km width. Weak return flow was observed outside the channel, consistent with the Southwood model. The flow is explained in terms of tension pull on newly open flux according to the Southwood model [*Pinnock et al.*, 1993, 1995]. *Chisham et al.* [2000] have later confirmed these findings.

iib) Pulsed Ionospheric Flows (PIFs) *Provan et al.* [1998], *Provan and Yeoman* [1999], and *McWilliams et al.* [2000] observed Pulsed Ionospheric Flow (PIFs) in the SuperDARN Hankasalmi radar. Poleward of the Convection Reversal Boundary (CRB) transient PIFs were observed, and interpreted as an ionospheric signature of FTEs on the newly reconnected field lines as they are pulled anti-sunward by the ionospheric flow. These observations have later also been seen by DMSP satellites [*Provan et al.*, 2002] and Cluster [*Wild et al.*, 2001]. *Provan and Yeoman* [1999] made a statistical analysis from the SuperDARN Hankasalmi radar over 2 years, and found the statistical occurrence of PIFs, see Figure 2.21. They reported that the azimuthal extent of the PIF was 4-4.5 hours (1500 km) around magnetic noon, but pointed out that due to only line of sight measurements it is impossible to measure the velocity vector from a single point. This flow is fundamentally the same as the FCE, described by *Provan et al.*

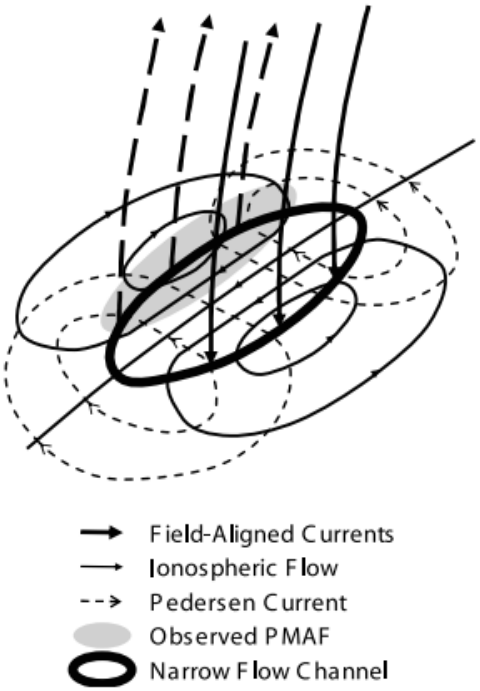

Figure 2.20: Sketch of FTE signatures in the ionosphere after a fluxtube reconnects at the dayside magnetopause. We can see the downward Field Aligned Currents (FACs) on closed field lines, and upward FAC on open field lines co-located with a PMAF. The solid lines of ionospheric flow is the plasma flow visible with the SuperDARN radars [from *Oksavik et al.* [2004], after *Southwood* [1987]].

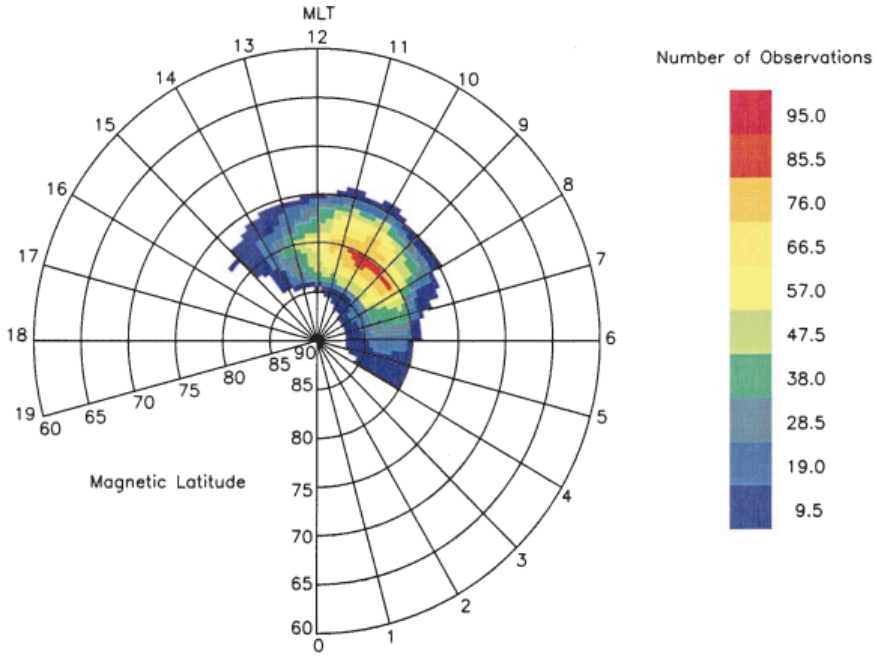

Figure 2.21: Occurrence distribution of PIF signatures in local times, as observed by the SuperDARN Hankasalmi radar from March 1995 to February 1997. The data is recorded predominantly under positive IMF B_y conditions resulting in a shift of events pre-noon [from *Provan and Yeoman*, 1999].

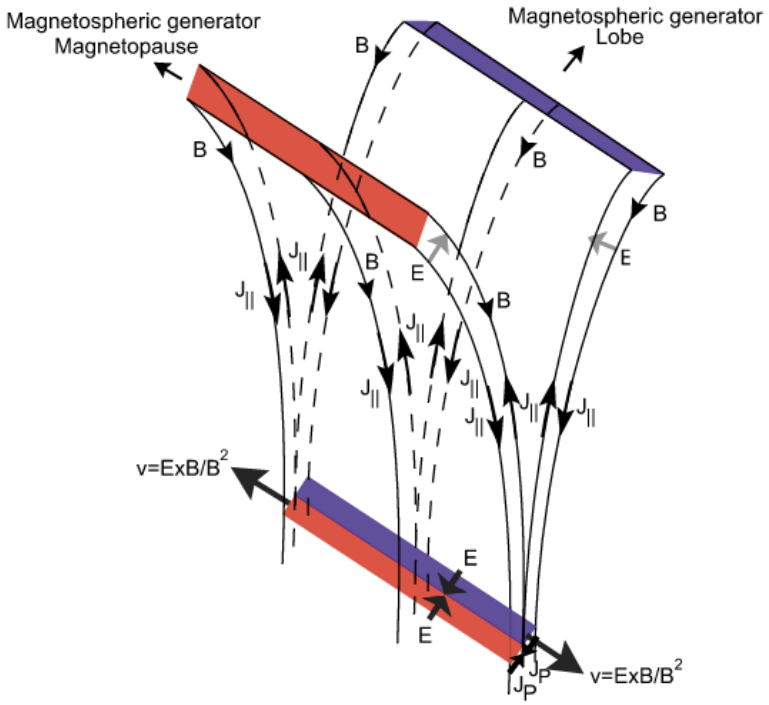

Figure 2.22: A sketch of eastward and westward flow channels couple through different generator regions in the magnetopshere. Note that both flows have the same direction as the magnetic pull, so they are not reversed flows [from *Rinne et al.*, 2010].

[2002] to also be a result of the magnetic tension force from the IMF B_y component.

iic) FTE flow channel FTE flow channels, which are on newly open field lines represent a patch of newly open flux [*Moen et al.*, 2012]. When the IMF B_y switches quickly between positive and negative, individual reconnection pulses will map down to different places in the ionosphere, which according to *Lockwood et al.* [2001] can be seen as a train of channels adjacent to each other. Individual FTE channels have been observed with the EISCAT Svalbard Radar (ESR) by *Rinne et al.* [2010] enabling high resolution tracking of individual FTE channels.

Rinne et al. [2010] notes that since there is a very sharp flow reversal boundary on each side of the flow channel, this implies the existence of a Field Aligned Current (FAC) sheet, see Figure 2.22. Since these flows are corresponding to different reconnection regions, they also have their own FTE generator. These flows will stay as long as the generators and FAC are active, which is until the magnetic tension of the newly reconnected flux tube has been released.

iii) Enhanced flows on old-open field lines

When magnetic flux from the inflow region convects in the anti-sunward direction far inside the polar cap it is called old open flux. From radar and satellite observations it has been seen that there can develop enhanced flow within the old open flux [e.g., *Stern*, 1984; *Sandholt et al.*, 2004; *Farrugia et al.*, 2004; *Sandholt and Farrugia*, 2007]. *Sandholt et al.* [2010] attribute the flow channel events to momentum transfer from the high-latitude and flank boundary layers of the magnetosphere, on the downstream

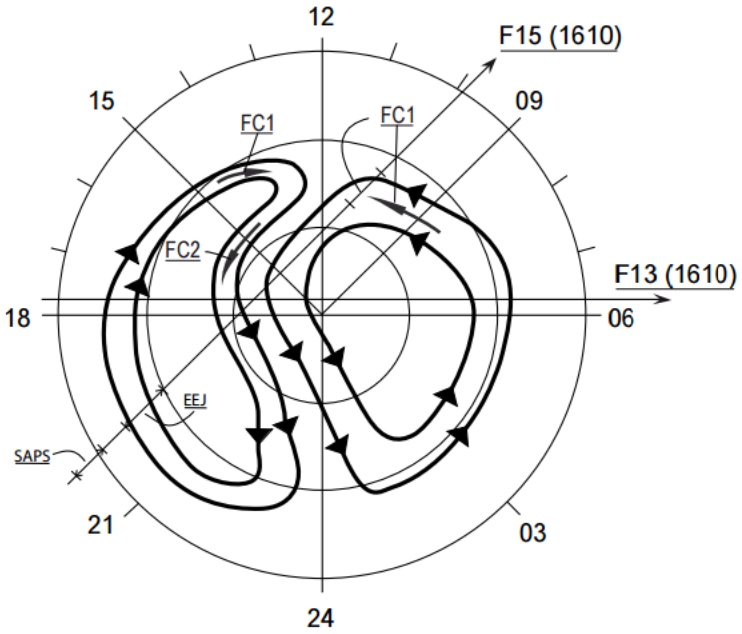

Figure 2.23: Enhanced flow on the old open flux, marked as FC2 in the Figure. The figure shows the situation when $B_y < 0$ for southward IMF conditions [from *Sandholt et al.*, 2010].

side of the cusp, via Birkeland currents. In that case, it is a result of the solar wind magnetosphere dynamo in the high latitude boundary layer. The flow channels were observed to last for 5-10 minutes, and for B_y negative it was seen to enhance the flow only on the dusk side, see Figure 2.23.

2.5.4 Poleward moving auroral forms

Polar Moving Auroral Forms (PMAFs) are the visual signature of the solar wind moving past Earth [*Vorobjev et al.*, 1975; *Fasel*, 1995; *Sandholt et al.*, 1998]. Specifically, it's the result of localized dayside magnetic reconnection events [*McWilliams et al.*, 2000; *Carlson et al.*, 2006]. In this sense, the PMAF is not a distinct flow channel, but the optical signature of newly open flow channels. They are rarely seen far inside the polar cap, but may exist as high density F-region plasma patches seen in airglow [*Lorentzen et al.*, 2010]. The importance of PMAFs is that they are associated with an upward Birkeland current [*Oksavik et al.*, 2005], and thus are connected to the flux tube of the FTE. This is also confirmed by observations from satellite conjunctions showing that these auroral forms are associated with enhanced fluxes of magnetosteath ions and electrons [e.g., *Sandholt and Newell*, 1992; *Moen et al.*, 1996; *Farrugia et al.*, 2003]. Similarly as the polar cap inflow region is affected by IMF B_y, the PMAFs can be dominated by a dawn-dusk motion [*Karlson et al.*, 1996; *Moen et al.*, 1995, 1996].

Another event related to PMAF is ion-upflow, which is ions quickly moving upwards in the ionosphere and has been extensively studied in the polar ionosphere [e.g., *Shelley et al.*, 1976; *Moore et al.*, 1986; *Pollock et al.*, 1990]. *Moen et al.* [2004] observed that there is an one-to-one correspondence between ion-upflow events and individual PMAFs. Because of their relation to PMAFs, *Moen et al.* [2012] conclude that precip-

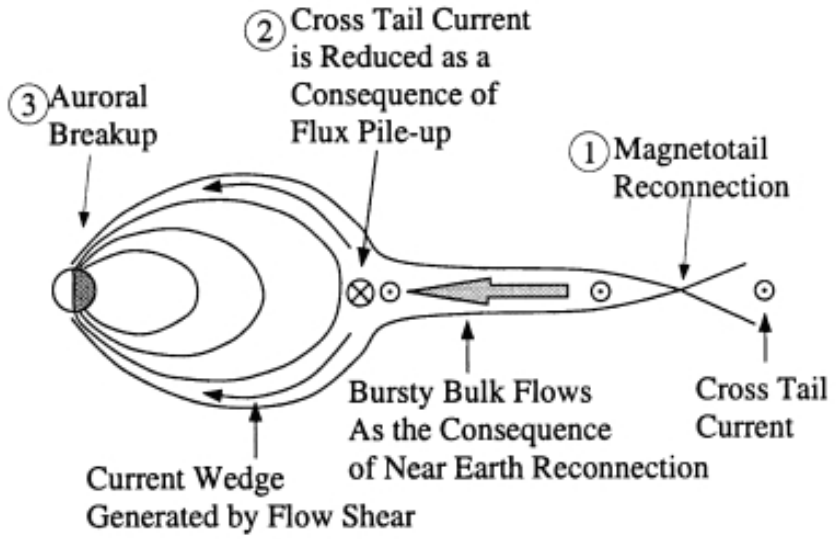

Figure 2.24: Schematic view of how the bursty bulk flow is generated as a consequence of magnetotail reconnection between 1) and 2) in the figure. Later this causes auroral breakup and auroral streamsters seen in 3) [Downloaded from `http://www.igep.tu-bs.de/forschung/weltraumphysik/projekte/themis/wissziel_en.html` on 27.04.2017].

itating magnetosteath electrons contribute with energy for ion-upflow in FTEs.

As we will study in more depth later, there is a close connection between ionospheric flow channels and PMAF [*Lockwood et al.*, 1990], FTEs [*Milan et al.*, 2000] and the RFEs [*Moen et al.*, 2008].

2.5.5 Nightside flow channels

Reversed flow channels seen in the nightside polar cap can not be related to dayside reconnection due to their location on already open field lines far from the dayside OCB. There are several types of flow enhancements seen in the nightside ionosphere, which is important for understanding the development of nightside reversed flows. Here we will explain auroral streamers and Bursty Bulk Flow (BBF).

Auroral streamers are north-south aligned auroral thin arcs in the nightside ionosphere [e.g., *Nakamura et al.*, 2001; *Sergeev et al.*, 2004]. *Nakamura et al.* [2001] reports that the auroral streamers are observed in relation to auroral expansion and eastward flow bursts at midnight MLT. These flow channels are also observed to have a time scale of 2.5 min on average, and are accompanied by large flow shears.

The auroral streamer is interpreted as an ionospheric phenomenon of eastward BBF [e.g., *Angelopoulos et al.*, 1992; *Nishimura et al.*, 2011]. BBFs are mid-tail plasma sheet flow enhancements with embedded flow bursts down to 1 minute duration [*Baumjohann et al.*, 1989]. These fast flows are thought to play a key role in magnetotail flux transport and nightside reconnection [*Nagai et al.*, 1998].

Figure 2.24 shows a sketch of how the BBF is affecting the ionosphere and resulting in auroral streamers. Fast flow channels seen by SuperDARN in the nightside ionosphere might be a result of this BBF happening in the inner tail magnetosphere.

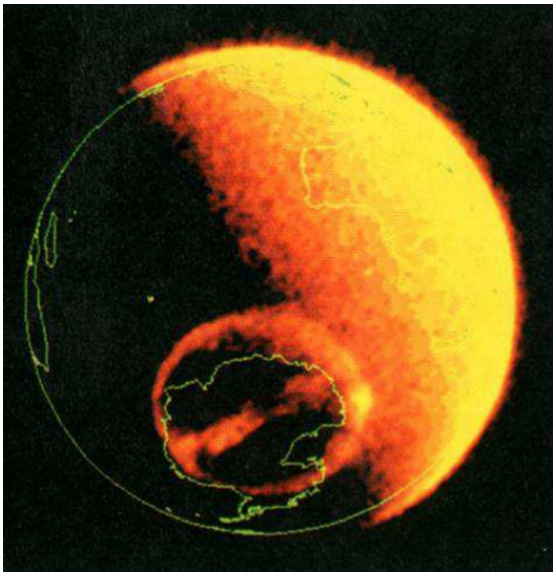

Figure 2.25: Theta aurora observed by the FUV instrument of the Dynamics Explorer (DE) 1 spacecraft in 1983 over the southern hemisphere [from *Frank and Craven*, 1988].

2.5.6 Transpolar arcs

Arcs of aurora originating in the nightside polar cap and extending far into the otherwise dark polar cap are called TransPolar Arcs (TPAs) after first being observed by *Frank et al.* [1982]. These usually short lived visible features may extend all the way into the dayside polar cap, for which they are called theta aurora. A figure of a TPA extending all the way across the polar cap can be seen in Figure 2.25.

The usual transpolar arc is also primarily occurring under quiet geomagnetic conditions and northward IMF with reconnection in the lobes [*Berkey et al.*, 1976]. The IMF B_y strength up to several hours prior to appearance of an arc is shown by *Fear and Milan* [2012b] to influence the MLT location of the TPA. The same study observes dawn and duskward motion induced by fluctuating IMF B_y.

As discussed in *Fear and Milan* [2012b] there exist several competing models for the generation of TPAs, and whether they form on open or closed filed lines. In one such model of TPAs forming on closed field lines by *Milan et al.* [2005], the TPA forms as a tongue of closed magnetic flux embedded in the open field line polar cap. This is thought to occur for northward IMF and a significant B_y, resulting in twisted reconnection in the tail. As the reconnection proceeds, the TPA gradually extends towards higher latitudes.

Of our interest are strong azimuthal flows along the nightside auroral oval, which are observed during twisted tail reconnection and thus also simultaneously with TPAs [*Milan et al.*, 2005], see panel (b) and (c) of Figure 2.26.

According to the *Milan et al.* [2005] model there should be azimuthal flow towards midnight MLT, e.g. opposite the direction of asymmetric convection cycle as predicted by *Dungey* [1961]. *Fear and Milan* [2012a] tested this assumption by identifying enhanced flows from the SuperDARN radars simultaneously with TPAs seen by the IMAGE spacecraft [*Mende et al.*, 2000]. They confirmed the existence of reversed flows azimuthal along the nightside auroral oval towards magnetic midnight.

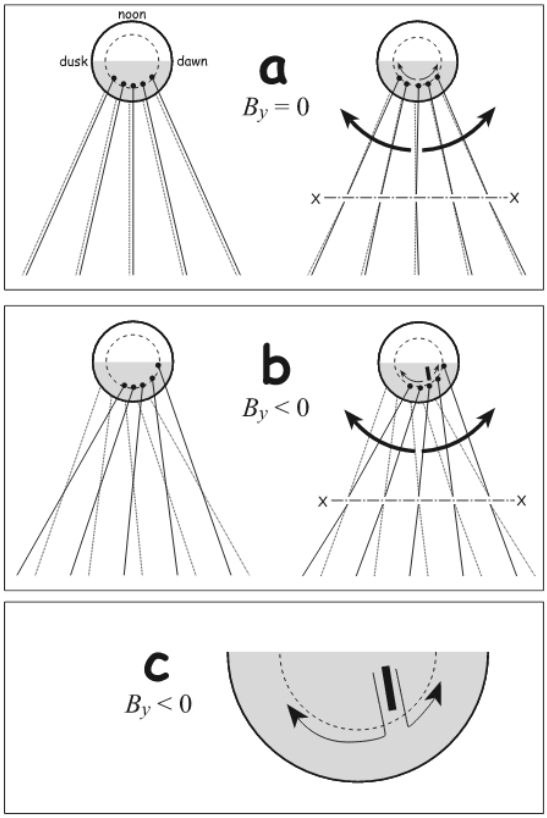

Figure 2.26: Schematic illustration of TPA formation after the *Milan et al.* [2005] model of twisted tail reconnection. (a) shows tail reconnection for B_y close to zero. In (b) we see twisted tail reconnection for $B_y < 0$. The area where the TPA and azimuthal flow originates is enlarged in (c). From *Fear and Milan* [2012a] originally after *Milan et al.* [2005].

Fear et al. [2014] recently observed electron plasma originating from closed field lines mapping down to the observed TPAs with a dual spacecraft study. This strengthens the theory that TPAs originate on closed field lines in accordance with the model of *Milan et al.* [2005].

2.6 Reversed Flow Event (RFE)

2.6.1 Definition, characteristics and examples

The flow events described by *Sandholt et al.* [2004] have all in common that they describe enhanced flow in the same direction as the background flow.

Rinne et al. [2007] discovered a new and fourth category of enhanced flow in the opposite direction of the background flow called Reversed Flow Events (RFEs). By analysing 11 days of the winter cusp ionosphere, their study identified 21 RFEs. For such an event the flow needs to be greater than 250 m/s in opposite direction of the background convection, with a minimum of 500 m/s shear flow. A summary of all their observations can be seen in Table 2.2.

Rinne et al. [2007] observed RFEs in 40% of the radar scans within one hour of magnetic noon. Their study was carried out with the EISCAT Svalbard radar, and the 21 RFEs were found in about 16 % of the 767 scanned plots. The RFEs were found to last ∼19 minutes on average. Their study describes a series of RFEs in January and December 2001 previously also analysed by *Oksavik et al.* [2004, 2005].

Reversed Flow Event (RFE) Definition

A Reversed Flow Event (RFE) is defined as an elongated segment of enhanced F-region ion flow in the opposite direction to the large scale background flow. The original

Table 2.2: RFEs found in EISCAT by *Rinne et al.* [2007]. The MLT for the events are not given by the authors, but this corresponds to a maximum of UT +2 hours for scans west of the radar, and UT + 4 hour for scans east of the radar.

Nr.	Site	Start time [yyy/mm/dd]	UT [hh:mm]	Duration [min]	IMF (B_y, B_z)
1	esr	2001/01/16	10:07	9	-, -
2	esr	2001/01/20	06:45	4	-, -
3	esr	2001/12/15	07:36	7	+, -
4	esr	2001/12/15	09:24	3	+, -
5	esr	2001/12/15	10:03	55	+, +
6	esr	2001/12/16	07:31	6	+, +
7	esr	2001/12/16	08:03	49	+, +
8	esr	2001/12/16	08:39	9	+, +
9	esr	2001/12/16	08:52	38	+, +
10	esr	2001/12/16	10:16	29	+, +
11	esr	2001/12/16	10:51	9	+, +
12	esr	2001/12/18	06:43	7	+, -
13	esr	2001/12/18	07:54	9	+, -
14	esr	2001/12/18	09:38	29	+, -
15	esr	2001/12/18	09:51	29	+, -
16	esr	2001/12/28	10:07	37	+, -
17	esr	2001/12/20	06:19	3	+, -
18	esr	2001/12/20	10:25	26	+, -
19	esr	2001/12/20	10:41	16	+, -
20	esr	2001/12/21	07:38	17	+, -
21	esr	2001/12/21	08:55	17	+, -

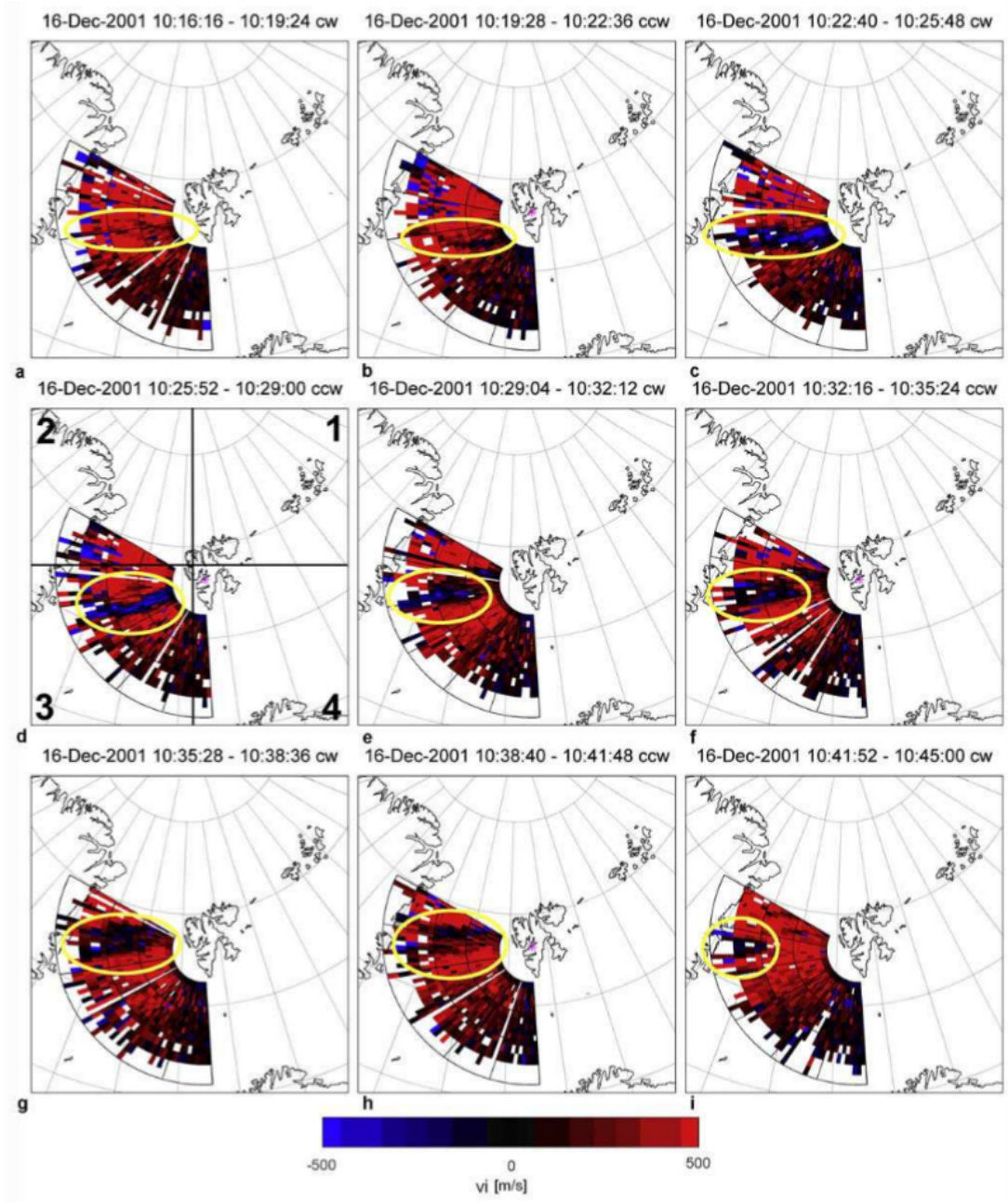

Figure 2.27: Overview of the development of an RFE as seen with the EISCAT Svalbard Radar, on 16 December 2001 at 10:16 UT. The event lasted 29 minutes for both positive IMF B_y and B_z. The fan plots of ion velocities are projected on geographic coordinates. Positive red values indicate line of sight flow velocity away from the radar while blue is flow velocity towards the radar. The RFE can be seen as blue eastward flow in the otherwise westward flow marked with yellow circles [from *Rinne et al.*, 2007].

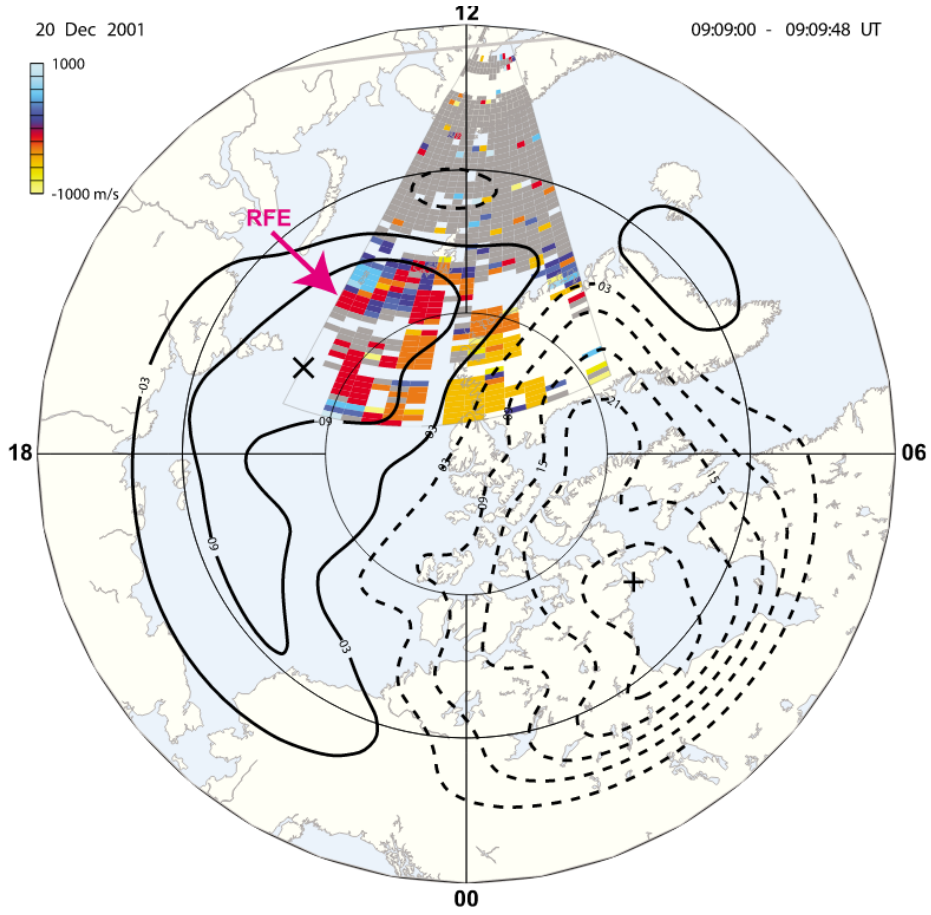

Figure 2.28: RFE seen on 20 December 2001 with the SuperDARN Hankasalmi radar [from *Oksavik et al.*, 2011].

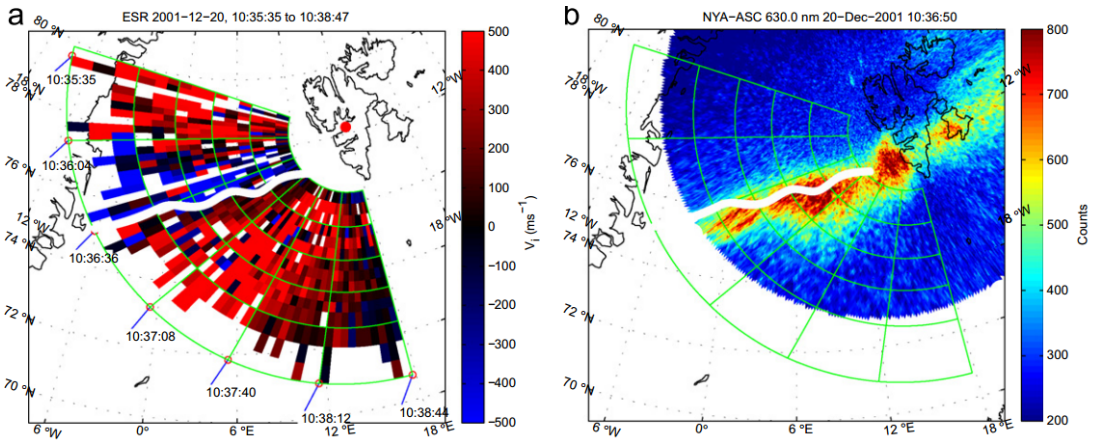

Figure 2.29: EISCAT Svalbard Radar scan in (a) and all-sky camera (b) seen during the same RFE. The white contour marks the flow shear reversal at the equatorward edge of the RFE, in alignment with the poleward edge of the PMAF [from *Moen et al.*, 2012].

ionospheric flow channel criteria set by *Rinne et al.* [2007] for flow channels to satisfy the RFE definition are as follows:

1. The RFE has to be evident in more than one radar beam direction (azimuth position). This criterion eliminates questionable measurements.

2. The line-of-sight ion drift velocity inside the RFE must be $>$ |250| m/s for at least one scan during the lifetime of the event.

3. The longitudinal extent of an RFE has to exceed 400 km in the radar field of view.

4. The RFE has to stay in clear contrast to the background flow, i.e., the background flow must exhibit uniform and opposite velocities $>$ |250| m/s in the area surrounding the RFE for at least one scan.

5. The RFE has to be embedded within the background flow for at least one scan (this criterion avoids large-scale convection reversals being detected as RFE).

In contrast to the flow channels reported by *Sandholt et al.* [2004], RFEs flow longitudinally and oppose the magnetic tension pull, and therefore according to *Moen et al.* [2008] are unlikely to represent newly open flux. Consequently, the RFE is a principally different category of flow channel.

Moen et al. [2008] reported two different types of RFEs: i) One moving into the polar cap on the poleward boundary of a PMAF and ii) RFEs moving longitudinally together with the cusp boundary.

The problem with the EISCAT azimuthal scan is that the antenna has to physically move from one side to the other, which takes up to 4 minutes at maximum speed.

Rinne et al. [2007] observed the RFEs to be 50-250 km wide in latitude and often longer in longitude than the ESR field of view (600 km). The RFEs were all observed between 40° and 240° By/Bz defined clock angle with 95% opposing the IMF dependent magnetic tension force *Heppner and Maynard* [1987]. An example of the RFEs observed by *Rinne et al.* [2007] can be seen in Figure 2.27. Here the RFE can be seen as blue eastward flow towards the radar in the otherwise westward flow expected from the large scale convection seen by the SuperDARN radars.

It has long been thought that these transients features would be hard to see in SuperDARN radar data because of their relative narrow nature until *Oksavik et al.* [2011] discovered one RFE in SuperDARN data from the Hankasalmi Finland radar. Their event was a case study from 20 December 2001 and shown in Figure 2.28. The RFE is displayed as a red anti-sunward directed enhancement in a region of expected sunward flow in the post-noon inflow region.

A summary of all RFEs found by *Rinne et al.* [2007] is displayed in Table 2.2. Events are shown with their start date and time in UT as well as their duration in minutes. The last column shows if IMF B_y and B_z is positive or negative. We see that 14 out of 21 events happen for southward IMF, as well as 19 events for positive IMF B_y. However, *Rinne et al.* [2007] concludes that RFEs occur independent of the IMF B_y and B_z polarity, and that they form one by one and never in pairs.

Figure 2.29 shows an RFE previously detected by *Rinne et al.* [2007] and later analysed by *Moen et al.* [2012] in relation to a PMAF. The equatorward edge of the RFE is seen to co-locate with the sunward edge of the PMAF.

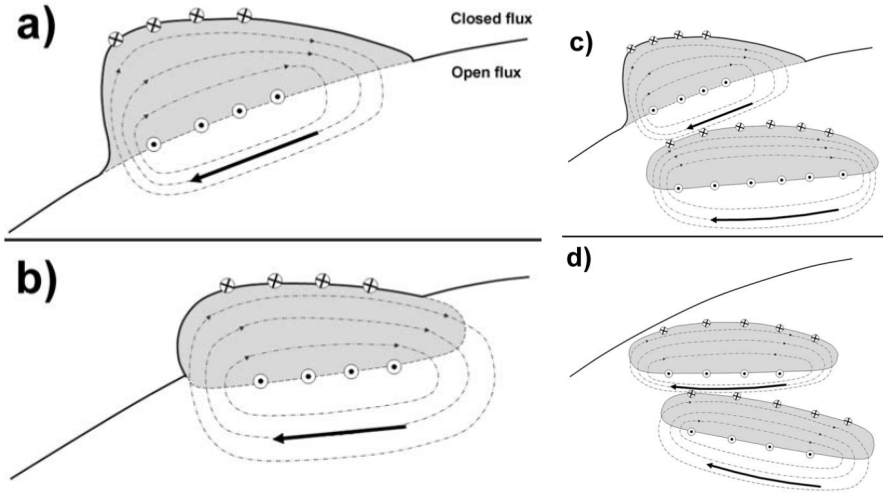

Figure 2.30: Generation of a single return flow by an asymmetric Southwood FTE model for IMF $B_y > 0$. a) shows how an newly opened flux represented with grey shading enters the polar cap. Circled dots and crosses represents the location of upward and downward FACs. b) shows the FTE at a later stage when it has been pulled into the polar cap. c) shows a second FTE entering the polar cap, while d) shows both FTEs propagating into the polar cap and elongating to the plasma convection [from *Rinne et al.*, 2007].

2.6.2 Relation to Southwood FTE

As the observed RFEs are phenomena near the cusp inflow region, *Rinne et al.* [2007] describes it as a signature of magnetic reconnection. Specifically it is a result of the Southwood FTE model [*Southwood*, 1987] (described in 2.5.3). In this model, there are expected to be two simultaneous return flows on each side of the center flux. *Rinne et al.* [2007], however, mostly found only one return flow. When both were present, they were not developing at the same time, and thus have to be considered as two different FTE events.

Since all RFEs observed by *Rinne et al.* [2007] were for strong B_y conditions, they suggested that the Southwood FTE model takes an asymmetric form where only the poleward cell of the Southwood FTE becomes visible, see Figure 2.30. In this way, it explains why only one return flow channel is observed for each FTE.

2.6.3 Possible generation via MI current loops

The generation of RFE can according to *Moen et al.* [2008] be explained as a region where two magnetosphere-ionosphere (MI) current loops, forced by independent voltage generators, couple through a poorly conducting ionosphere. The electric field arises in between large-scale currents loops, each mapping to a different reconnection site. Because of this, the RFE channel is a region with no precipitation, and particle impact ionization will not contribute to the Pedersen conductance. Figure 2.31 shows a sketch of the MI current system. Figure 2.32 shows how the RFE flow channel exist in a poorly conducting ionosphere between the current loops from Figure 2.31. *Moen et al.* [2008] suggested that the part of the RFE that is on the poleward side is on open flux, while the equatorward part is a subsequent FTE. The large E-field is a result of low Pedersen

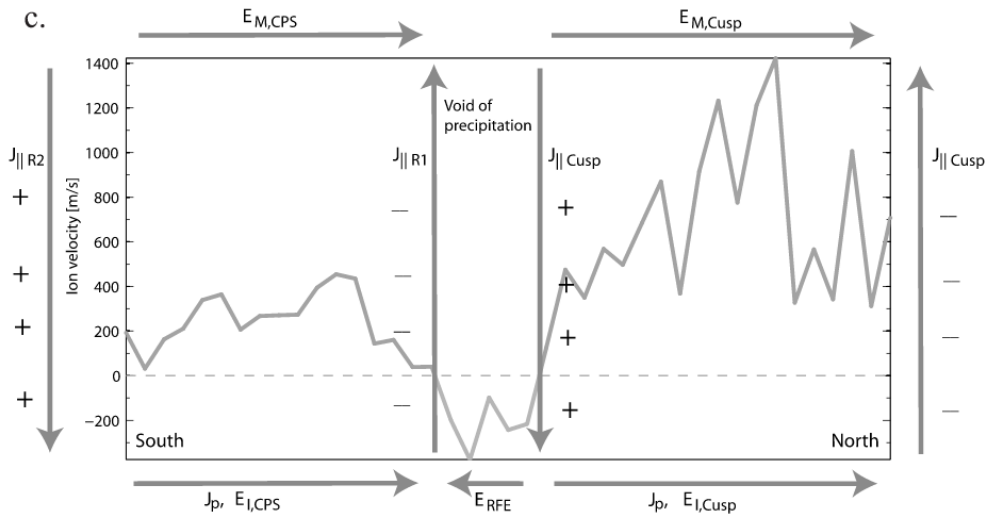

Figure 2.31: Schematic illustration of the RFE current systems relationship to the RFE flow shear. The two current loops on the left and right side are forced by separate voltage generators. The electric field of the RFE is located in a region of low conductivity and void of precipitation between the loops [from *Moen et al.*, 2008].

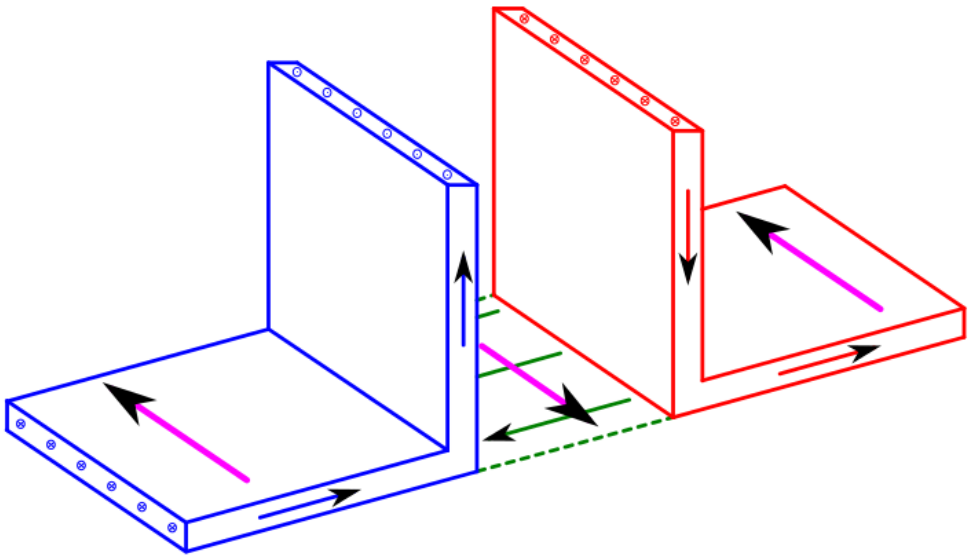

Figure 2.32: Independent currents seen in blue and red color thought to generate the RFE in green color as explained by *Moen et al.* [2008]. The blue current is the Region-1 current on closed field lines equatorward of the RFE, while the red current is on open field lines poleward of the RFE. The RFE is generated due the short circuit and electric field set up in the low conducting region between the current loops. The pink arrows show the flow direction with the RFE opposing the large scale flow [Figure from *Stausland*, 2014].

conductivity, which suggests that there should be a summer/winter asymmetry of RFE due to increased Pedersen conductivity in sunlit conditions which reduce chances of RFEs in summer.

2.6.4 Possible generation from inverted-Vs

Accelerated electron precipitation is thought to generate discrete auroral forms like PMAF according to *Moen et al.* [2012], which describes two acceleration mechanisms above the ionospheric cusp. Kinetic Alfven waves (KA waves) [*Chaston et al.*, 2007] are dispersive broad energy beams, while inverted-V type electron precipitation [*Lin and Hoffman*, 1982] gives rise to mono-energetic beams.

Moen et al. [2008] also suggested a second hypothesis that RFE channels may be the ionospheric footprint of an inverted-V type coupling region. Because the RFE flow disturbance is quasi-stationary and bipolar, it seems consistent with an inverted-V type potential structure [*Lin and Hoffman*, 1982]. This is electron acceleration events, which are called inverted-V type because it appears as an upside down V in electron spectrograms [*Newell*, 2000]. These structures are often observed near the dayside OCB on the immediate equatorward side of the cusp region, which contains trapped electrons [*Burch et al.*, 1990]. However, recently *Jacobsen et al.* [2010] observed an inverted-V acceleration consistent with Region-1 currents on open field lines. They didn't observe the inverted-Vs directly, but observed converging electric fields from the CLUSTER spacecraft as an indicator for inverted-V events at lower altitudes. This suggests that the RFE is a phenomenon of merging electric fields in the magnetosphere poleward of the OCB [*Jacobsen et al.*, 2010].

It is still unknown how and whether these two explanations are related and might work together. For example, the discontinuity in the magnetospheric electric field created in an MI current loop might create the precondition required for an inverted-V. Since there might be a lack of electrons to close the current through the existing potential, the inverted-V type accelerated electrons might feed this gap [*Moen et al.*, 2008].

Chapter 3

Instrumentation and Methods

In the following chapter we will give a description of the instruments used in this thesis. Physical properties, scientific advantages and limitations are discussed. SuperDARN is the most important instrument of this master project, and so it will therefore be explained in most detail.

3.1 SuperDARN

The Super Dual Auroral Radar Network (SuperDARN) is an international scientific radar network of coherent scatter HF radars covering both the northern and southern hemispheres. As of 2017 it consists of 23 radars in the northern hemisphere, and 12 in the southern.

SuperDARN is designed to detect backscatter from field-aligned decametre scale ionospheric irregularities. SuperDARN works as a Doppler-radar measuring the $\mathbf{E}\times\mathbf{B}$ drift speed in the F region ionosphere [*Greenwald et al.*, 1995; *Chisham et al.*, 2007]. The radar transmits a multipulse sequence of signals with pulse lengths usually ranging from $\sim$ 100 - 300 µs providing a range resolution of 15 - 45 km. The returned autocorrelation function is used to determine the line of sight Doppler velocity of the target in the ionosphere. From the backscattered signal other parameters like spectral width and the returned power are also determined. The spectral width is a measurement of fluctuations in the drift velocity, i.e. width of the Doppler spectrum. This can be used to locate the cusp region of open field lines. *Moen et al.* [2000, 2002] use spectral widths larger than 220 m/s as a discriminator for the cusp. This is potentially interesting for our study as well, as we are interested in determining if the RFE events are located on open or closed field lines. However, this is not an exact way to determine the OCB as there are many uncertainties [*Ponomarenko and Waters*, 2006]. Other authors like *Baker et al.* [1995] use for instance 250 m/s as the spectral width discriminator.

SuperDARN radars operate in the High Frequency (HF) band between 8.0 MHz and 22.0 MHz, corresponding to wavelengths of 14-37 m, and scans through 16 beams of azimuthal separation $\sim 3.24^\circ$ in[*Greenwald et al.*, 1995]. For the common scan mode one complete scan takes about $\sim$1 minute.

For our purpose, the three polar cap radars Clyde River (CLY), Inuvik (INV) and Rankin Inlet (RKN) are of most importance. After the Longyearbyen (LYR) radar started operating in 2016, we have also analysed data from this radar for December 2016 and January 2017. We have also found one event from the Hankasalmi (HAN)

Table 3.1: Overview of SuperDARN radars used in this thesis.

Name	code	Mag. lat[°]	Mag. lon[°]	Dir.	Start year
Clyde River	CLY	78.8	18.1	W	2012
Inuvik	INV	71.5	-85.1	E	2008
Rankin Inlet	RKN	72.6	-26.4	W	2007
Hankasalmi	HAN	59.1	104.5	W	1995
Longyearbyen	LYR	75.6	108.9	E	2016

radar. However, the signal from the HAN radar has a long propagation distance to reach the polar cap from it's location at 59.1° magnetic latitude. Because of this it will have much less backscatter from the polar cap. This radar is also more affected by bad reflection from ocean and land topography, since the signal needs to reflect several times between the ground and the ionosphere. A map of the coverage of all radars used in this thesis can be seen in Figure 3.1. The specific location, scan direction and start of operation are shown in Table 3.1.

Figure 3.2 shows an example of a typical ray-path of SuperDARN signals in the ionosphere. The HF radar signal is in principle reflected from the irregularities in the ionospheric plasma when the magnetic field lines are perpendicular to the signal. This is the case for the solid black lines marked with an arrow in the figure. When the angle between magnetic field lines and the emitted signal is too large, the signal will either cause ground scatter (shown to the right in the figure) or just go through the ionosphere (shown as grey lines).

Figure 3.3 shows a picture of an operating SuperDARN radar located in Longyearbyen, Svalbard. The radar is a phased-array radar, which means the azimuth angle of transmission can be electronically adjusted to make an entire scan of the field of view. The advantage with phased array radar is that it has no moving parts and can change azimuth angle very quickly.

3.1.1 Data fitting

An obvious drawback of single radar SuperDARN observations is the fact that the velocity is only the measured line of sight velocity, and not the true vector velocity. This often results in a problem when the radar is looking orthogonal towards the plasma flow, as the velocity is measured as zero just in front of the radar, and there is high velocity in the positive and negative direction on each side (when the plasma flow in reality is uniform and constant across the entire radar field of view).

SuperDARN radars transmit multipulse sequences to determine the Doppler velocity, spectral width and backscattered power. Plasma parameters are obtained via a frequency domain analysis of the power spectrum of the signal. To determine the physical properties of the received signal autocorrelation functions (ACFs) are used. Here we will only discuss the advantages and limitations of different AFCs for determining the plasma velocity. For for a full overview of how the radars are operating and the physical properties determined, the reader is referred to *Farley* [1972], *Greenwald et al.* [1985], *Barthes et al.* [1998], and references therein.

The ACF processing method used in this thesis is called FITEX2 (referred to as FITEX) [*Greenwald et al.*, 2008; *Ribeiro et al.*, 2013], which is improved over the original

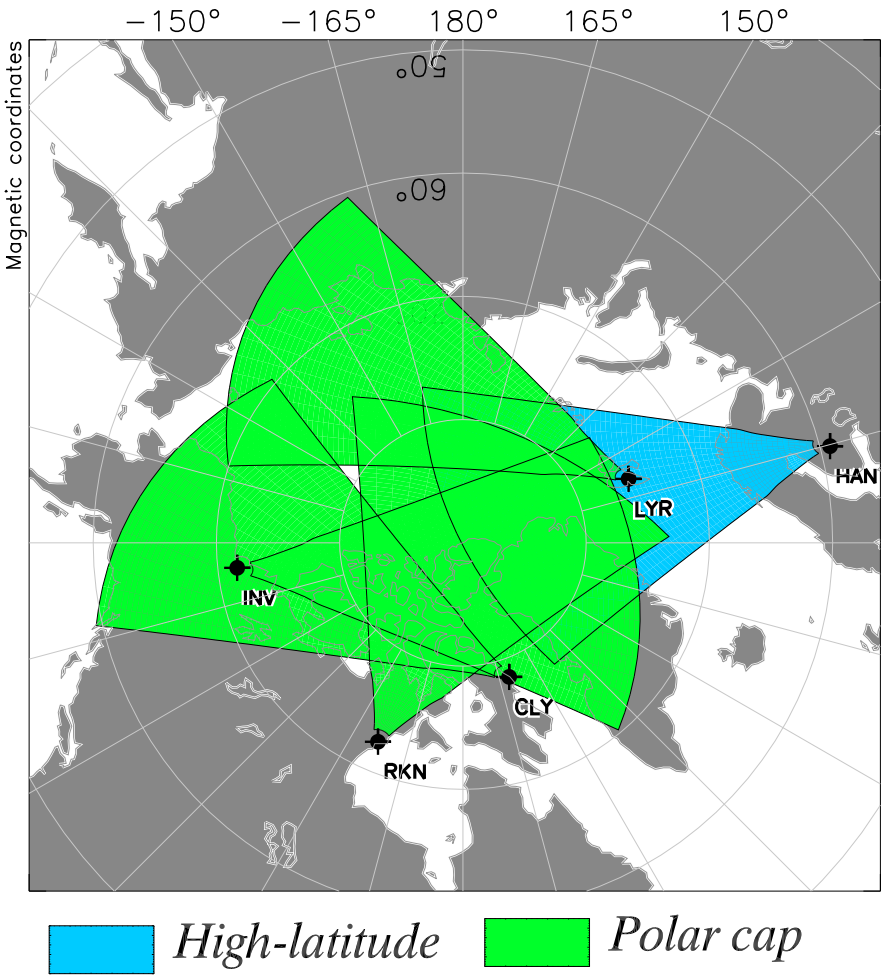

Figure 3.1: Coverage and field of view of the SuperDARN radars used in this thesis. The projection is in magnetic coordinates shows the northern hemisphere polar region.

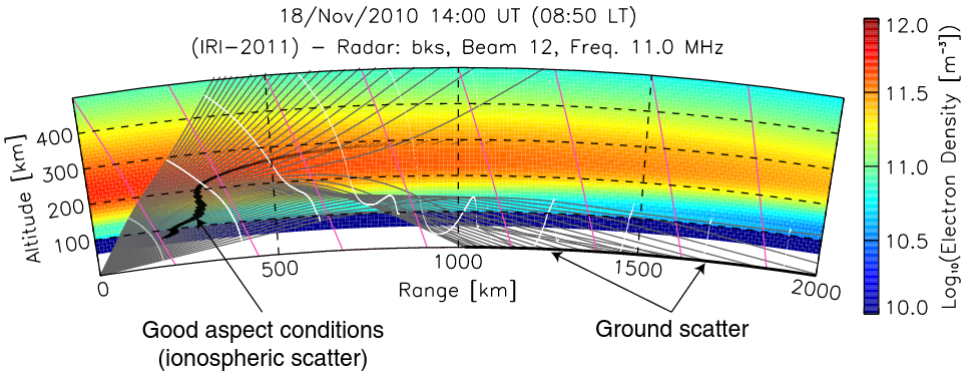

Figure 3.2: Example of ray-tracing of the SuperDARN backscatter signal from Blackstone radar on 18 November 2010 at 14:00 UT. The grey lines show the propagation for different rays responsible for ground scatter and good ionospheric scatter. Rays with highest elevation is lost without ionospheric backscatter [from *de Larquier et al.*, 2013].

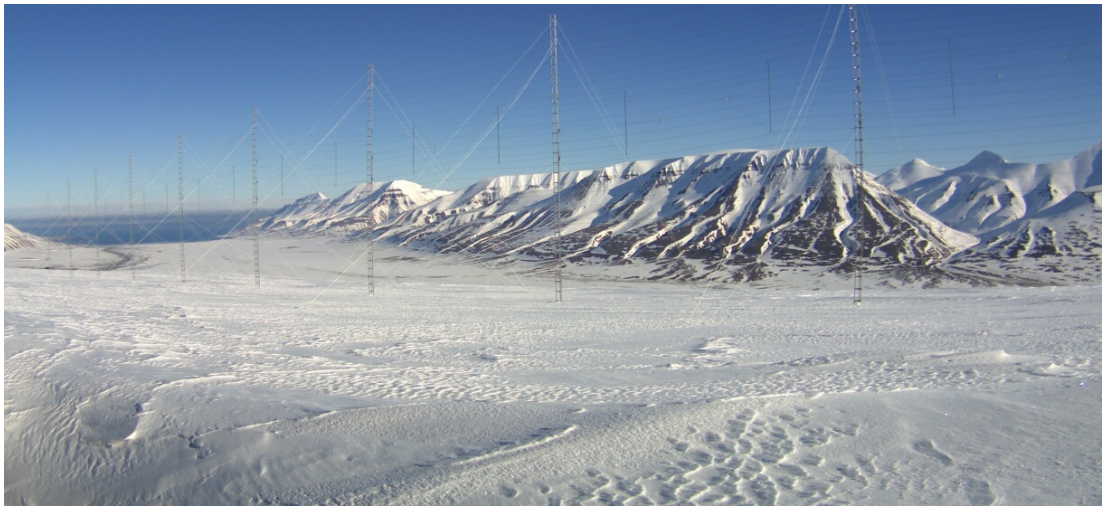

Figure 3.3: Photo of the SuperDARN radar in Longyearbyen, Svalbard that was officially opened on 19 October 2016. [photo provided by Mikko Syrjäsuo at UNIS]

FITACF method. The Doppler line of sight velocity is determined from a least square fit of the received lag profiles from the transmitted multipulse, which can range up to 24 lags per pulse [*Ribeiro et al.*, 2013]. To be able to determine the velocity there has to be a minimum of 4 "good" lags, meaning that the received signals are not affected by cross range interference or pulse overlap. The velocity of the range gate is successfully determined if the root-mean-square of the best fit is three standard deviations below the mean error across all fits. This error is the one we will be referring to when we discuss the results later.

Originally the FITACF method was used to determine the plasma velocities. However, it turns out for large velocities > 1000 m/s this method has a systematic error of producing flipped velocities based on an initial phase guess when the first two lags are "bad" [*Ribeiro et al.*, 2013]. This resulted in a large amount of artificial reversed flows with large errors. The FITEX method does not use any initial guesses and therefore does not make this systematic error.

3.2 Solar wind data

Magnetic data from the solar wind is recorded in order to monitor the direction and strength of the incoming solar wind when the SuperDARN radar data is collected. This is done thanks to the NASA OMNIWeb service[1]. These data are collected from satellites at the L1 Lagrange point $\sim$1.5 million km away from the Earth. This is about 1% of the distance between the Earth and the Sun. OMNIWeb data is timeshifted from the L1 point to the Earth's bowshock as described by *King and Papitashvili* [2005]. This is done according to the bow shock model of *Farris and Russell* [1994]. The initial ACE data has a 16-sec resolution, but for the data used in this thesis it is averaged over one minute for the relevant time period.

[1] http://omniweb.gsfc.nasa.gov

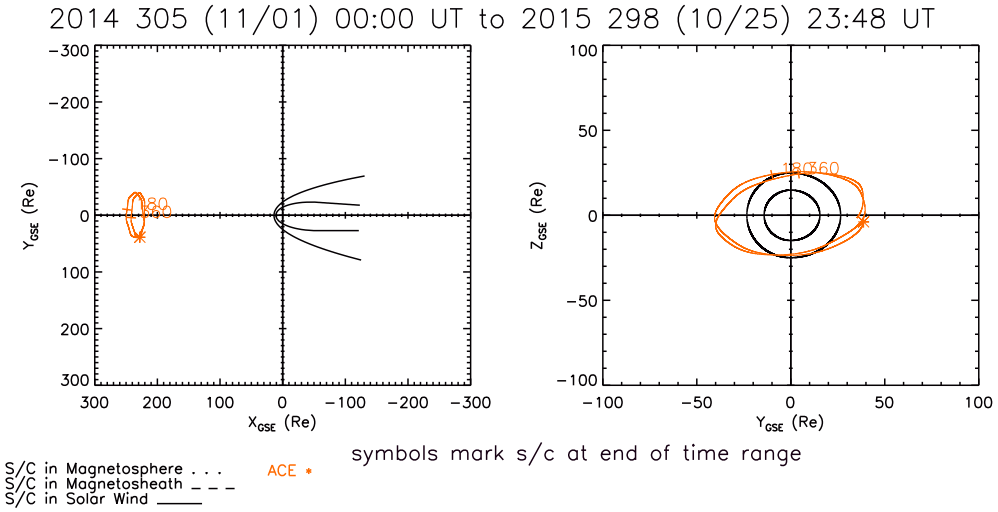

Figure 3.4: Orbit of the ACE satellite during a full year in 2014-2015. We can see how the orbit around the L1 point is not circular, but rather elliptic. Downloaded from `https://sscweb.gsfc.nasa.gov` on 27 April 2017

.

3.2.1 ACE satellite

There are several satellites orbiting around the L1 point. In this thesis we are mostly interested in magnetic field data from the years 2014-2017. For that purpose the Advanced Composition Explorer (ACE) [*Stone et al.*, 1998] launched on 05 February 1998 will be most relevant. As an redundancy, data from earlier missions IMP-8 and WIND are also available for times when ACE data is unavailable.

Figure 3.4 shows the orbit of the ACE spacecraft during an entire year. We can see that the spacecraft makes about 2 orbits during one terrestrial year. The offset from the equatorial plane is being corrected for in the OMNI data from NASA providing the solar wind conditions.

ACE consists of several instruments, but the one providing magnetic field data is called MAG and consists of two flux-gate magnetometers mounted on the tip of two booms of the spacecraft for reduced noise and redundancy *Smith et al.* [1998]. ACE measures magnetic field strength in three dimensions in GSM coordinates, and thus has three orthogonal mounted flux-gate instruments for each sensor. The flux-gate magnetometer works by passing an alternating current through one of two parallel mounted coils of wires. The induced magnetic field in the secondary coil represents the magnetic field generated by the first coil, in addition to the external magnetic field. Since we know the input magnetic field from the first coil, the magnitude of the external field representing the magnetic field from the solar wind can be calculated.

In some cases the ACE data in unavailable due to maintenance or orbital manoeuvres, and then the Wind satellite data will be filled in.

3.2.2 IMF uncertainty

In the IMF OMNI plots that will be presented in Chapter 4 we have included data from one hour before the events to make sure the relevant time of the solar wind is covered. The IMF data are timeshifted to the expected position of the Earth's bowshock based

on the GSM V_x component flow speed towards the Earth measured by the satellite. This timeshift is usually about 50-70 minutes for normal solar wind speeds between 350-500 km/s. In addition, there is a further delay of at least 5-8 minutes until we can see the ionospheric response [*Moen et al.*, 1999]. This depends on the location of the bow shock, which usually lies around 90 000 km away from the Earth. However, for positive B_z reconnection will take place in the lobes further towards the nightside of the Earth, adding an additional time delay to the propagation time from the observation at L1 until the response in the ionosphere.

Accounting for a plausible error in the measured solar wind speed of 10% at 500 km/s gives a change of ± 5 min in the propagation time. Even after adding other uncertainties as the position of bow shock of the Earth, it is very likely that the onset of the ionospheric response is within the time span shown in the OMNI plots. Furthermore, we also tried to pay close attention to any sharp transition in the orientation of the IMF that may affect our conclusions.

3.3 DMSP satellite data

The Defense Meteorological Satellite Program (DMSP) is a meteorological and space weather satellite program with several tens of satellites launched between 1962 and 2014. There is a wide range of scientific instruments on board the DMSP satellites. For our interest the newest generation of satellites (F16-F19) launched in 2003 - 2014 containing a series of ultraviolet imaging sensors is the most important. The satellites are in polar sun-synchronus orbits at 840 km altitude with an orbital period of 102 min. This orbit goes through the uppermost region of the ionosphere, and causes the orbit to approximately be fixed in local time.

3.3.1 SSUSI

The Special Sensor Spectrographic Imager (SSUSI) is the instrument on-board DMSP that is of interest for UV imaging. SSUSI contains a line scanning imaging spectrograph (SIS) covering the far ultraviolet spectrum, which is the sensor we will use. The spectrometer records auroral emissions in 5 different channels depending on wavelength, namely 121.6, 130.4, 135.6, 140-150 and 165-180 nm [*Paxton et al.*, 1992]. The SIS is a circle spectrograph consisting of a cross-track scan mirror, and a telescope mirror. A drawing of the instrument is shown in Figure 3.5. The lens has a 11.8° field of view resulting in a 153 km wide cross track line scan. With 16 spatial sensors will this give 10 km x 10 km resolution with 156 pixels from horizon to horizon. A full description of the instrument can be found in *Paxton et al.* [1992].

Figure 3.6 shows an example of auroral intensity in the UV-spectrum as seen by the DMSP satellite after several passes over northern Canada.

Due to scattering of sunlight there will be contamination of non-auroral UV detection in the spectrometer as dayglow [e.g. *Strickland et al.*, 2004]. To remove this contribution from the detected signal, a model for dayglow intensities is developed. However, due to uncertainties in this model, the minimum intensity threshold for detection of FUV aurora is higher on the dayside. For the 121 nm emissions the threshold is 2000 R (Rayleigh) against a 10 kR background, while for the nightside it is only 500 R for a 1 kR background [*Paxton et al.*, 1992]. This is one of the reasons why most

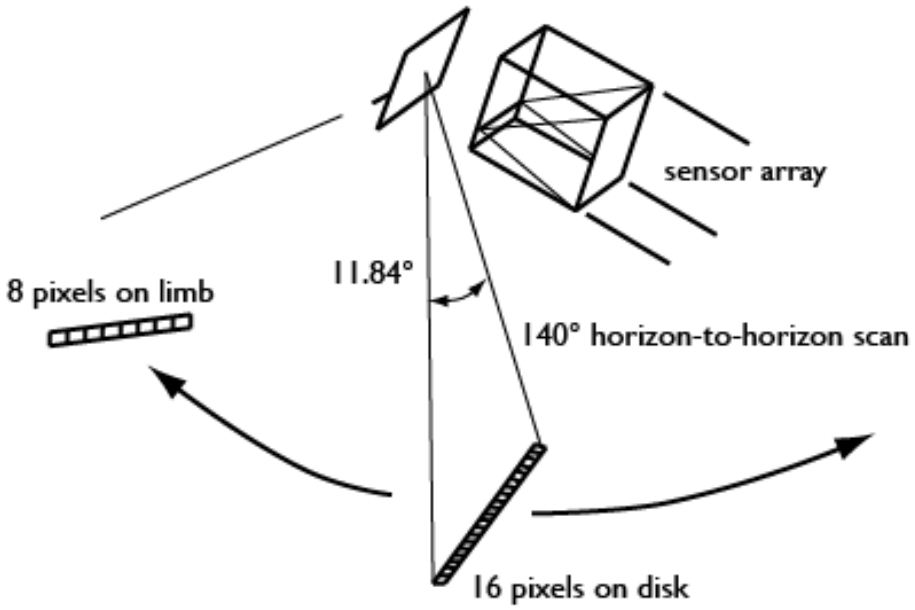

Figure 3.5: Drawing of the SSUSI instrument that makes a 153 km wide cross track line scan of 16 pixels as the satellite passes over the auroral oval [downloaded from `http://ssusi.jhuapl.edu/instrument_system_description` on 27 April 2017

.

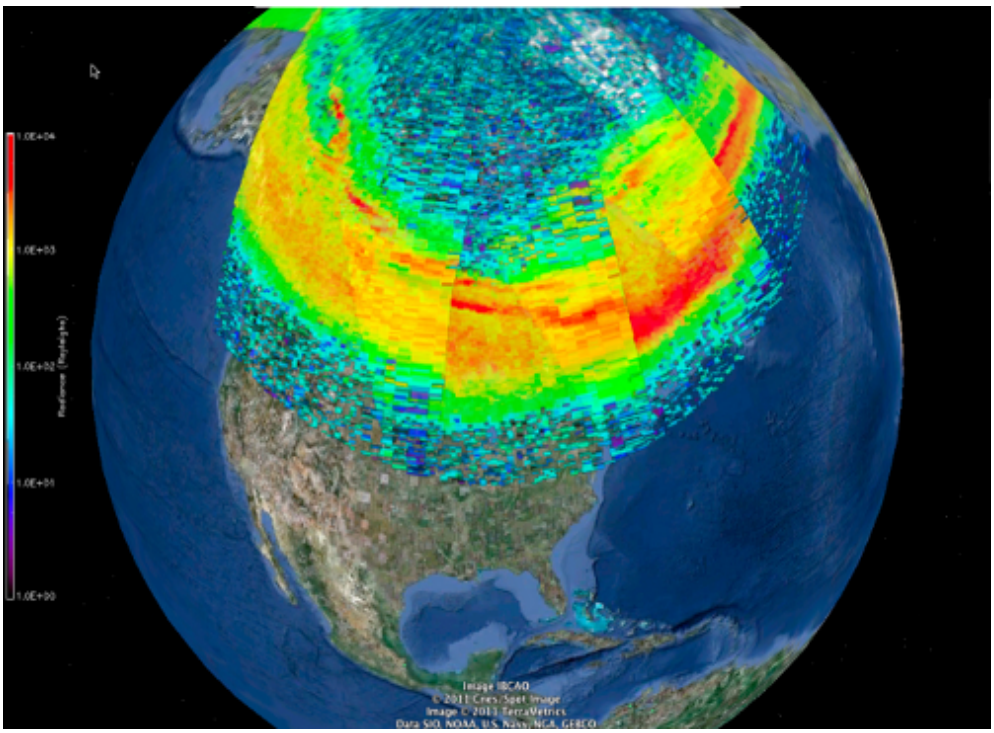

Figure 3.6: Example of auroral emission observed by DMSP spacecraft in the northern hemisphere [downloaded from `https://ssusi.jhuapl.edu/` on 09 May 2017].

of our measurements are from December, when the dayside dayglow is at a minimum around winter solstice.

3.4 SWARM

SWARM is a three spacecraft European Space Agency (ESA) mission with the main goal to study the Earth's magnetic field [*Friis-Christensen et al.*, 2006]. SWARM A and C are in polar orbits of 450 km altitude with 93 min orbital period, while SWARM B is in a slightly higher orbit at 513 km and 95 min orbital period. All three satellites were launched simultaneously on 22 November 2013. There are several different instruments on board, with the Vector Field Magnetometer (VFM) and Electric Field Instrument (EFI) being the most important for our purpose. Unfortunately, after talking to one of the lead scientists of the EFI instrument, Dr. Johnathan Burchill from University of Calgary, we learned that the charged particle detectors representing the EFI were quite unreliable and did not give satisfying results from the first two years of operation. There were therefore no EFI data available for the time of our SuperDARN measurements.

3.4.1 Vector Field Magnetometer

The magnetometer is a fluxgate type magnetometer consisting of a 3-axis Compact Spherical Coil (CSC) mounted on the tip of the optical bench of the spacecraft. An illustration of the spacecraft can be seen in Figure 3.7. For this thesis we have used the Level-2 Field Aligned Current (FAC) data which is derived using the spatial gradient of the geomagnetic field data from the VFM instrument. This is first done by using Ampere's law to find the vertical current density:

$$j_z = \frac{1}{\mu_0}\left[\frac{\partial B_y}{\partial x} - \frac{\partial B_x}{\partial y}\right] \tag{3.1}$$

where j_z is the current density, μ_0 the magnetic permeability, and B the magnetic field strength. The Z-axis is pointing vertically downward, X-axis is northward, and Y-axis is eastward. The FAC density is then found by taking into account the magnetic inclination angle I so that:

$$j_{FAC} = -\frac{j_z}{\sin I} \tag{3.2}$$

However, for our purposes we generally look at the FAC at high latitudes where the inclination is close to 90°, and the FAC density is almost identical to the vertical current density in Equation 3.1. For detailed information about how the FAC is calculated the reader is referred to *Ritter et al.* [2013]. That paper also explains how the multi-constellation spacecraft can be used to make more accurate readings of the FAC fluctuations.

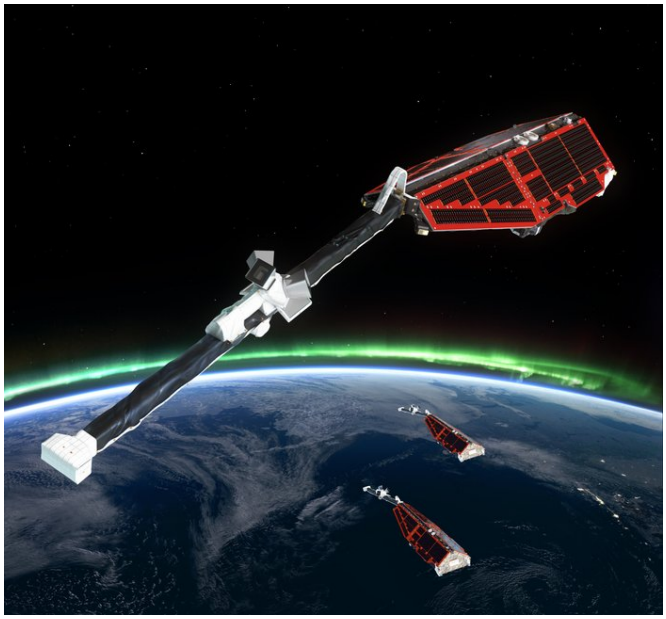

Figure 3.7: Illustration of the three satellite SWARM constellation flying over the polar cap. The VFM instrument is mounted to the left at the end of the optical bench [downloaded from `http://www.esa.int/spaceinimages/Images/2012/03/Swarm` on 27 April 2017].

3.5 NOAA POES and MetOp spacecrafts

The National Oceanic and Atmospheric Administration (NOAA) Polar Orbiting Environmental Satellites (POES) are sun-synchronous polar orbiting satellites in an orbit of 850 km altitude, and the orbital period is 102 min. As of 2017 the constellation consists of 3 operational satellites launched between 1998 and 2009 with a variety of weather monitoring instruments. For our purpose we will focus on the Space Environment Monitor (SEM-2) instrument that measures the flux of precipitating particles into the ionosphere.

NOAA has also provided the SEM-2 instrument for the ESA led polar orbiting meteorological satellites MetOp-A and B launched in 2006 and 2012. These satellites contain the same SEM-2 instruments as the POES satellites. SEM-2 consists of two instruments, the Total Energy Detector (TED) measuring soft particles for energies up to 20 keV and the Medium Energy Proton and Electron Detector (MEPED) measuring energetic ions for energies up to 6900 keV. For our study, we will only use data from the MEPED detector that is used to identify the polar cap area of open field lines in areas with no visual DMSP coverage.

3.5.1 MEPED

MEPED is a solid state detector measuring electron energies from 30 - 1000 keV and ions from 30 - 6900 keV. A full technical description of the instrument can be found in *Evans and Greer* [2000]. This instrument is known to degrade its sensitivity over time [*Galand and Evans*, 2000; *Sandanger et al.*, 2015], but for our purpose we are only interested to know the poleward boundary of the polar cap which is the boundary for open magnetic field lines. To determine the boundary we use electron energies > 30

keV for the 90° sensor which looks outside the loss cone. Particles outside the loss cone will not be lost and mirror in the magnetic field below the satellite. The > 30 keV boundary is used as an "electron trapping boundary" indicating the location of the "last" magnetic field line that is considered to contain trapped particles. Electrons with energies > 30 keV have their origin in the magnetosphere, and will move quickly back and forth along closed field lines. When a field line is opened due to magnetic reconnection, the electrons will escape and not longer be detected [*Lorentzen et al.*, 1996]. The area poleward of this electron trapping boundary is therefore used as locator for the open polar cap, called the open-closed field line boundary (OCB).

3.6 Data Analysis strategy

The work in this thesis is a combination of a statistical survey of SuperDARN flow velocity data, and case studies of specific events. A significant amount of time was spent to write the code enabling efficient detection of RFEs in the SuperDARN data set. Although RFEs have been seen in the SuperDARN dataset before, it was just a few cases that were found manually by looking through scan plots [*Oksavik et al.*, 2011]. Our work has therefore significantly increased the database of RFEs in SuperDARN.

We have developed a algorithm for systematical detection of RFEs based on the definition by *Rinne et al.* [2007]. We have chosen to analyse data from the polar cap SuperDARN radars consisting of Clyde River (CLY), Inuvik (IV) and Rankin Inlet (RKN) mainly for December 2014 and December 2015. Data from Longyearbyen (LYR) is also analysed in December 2016 and January 2016. For each radar, a total of about 60 days have therefore been analysed. The reason why December and January are chosen is because previous studies shows more SuperDARN backscatter during the polar night [*Imber et al.*, 2013], and a winter-summer asymmetry where RFEs don't develop under sunlit conditions [*Moen et al.*, 2008].

Originally only 7-10 days of the radar world day campaigns of 2014 and 2015 were analysed due to high data availability of conjugate observations such as the incoherent scatter radars EISCAT and RISR-N [*Bahcivan et al.*, 2010]. For 2014 we found a few cases of interesting RFEs over the RISR-N field of view, but unfortunately after contacting Roger Varney at SRI (which is responsible for operating the radar) we learned that the Generator Building at Resolute Bay caught fire, and there was no available data for the second half of the 2014 World Day.

The EISCAT radar is too far away for having any conjugate data with the three original polar SuperDARN radars. To increase our statistics we did a further search with our algorithm for the full months of December 2014 and December 2015.

A key reason for our focus on SuperDARN line of sight velocity data is because these data are not biased towards any large scale static models or assumptions for the ionospheric convection. It is in particular for small localised areas and short temporal scales that there is a knowledge gap in terms of understanding the actual flow of plasma in the ionosphere. With the SuperDARN line of sight dataset of a full scan in 60 seconds we have an excellent tool to address this topic.

Our second challenge was to find events with good data coverage and conjugate satellite and/or other ground based data. This is important both to verify the reliability of flow channels seen in SuperDARN data, but also to supplement with data such as auroral arcs from the DMSP satellite, and field aligned currents from SWARM. The

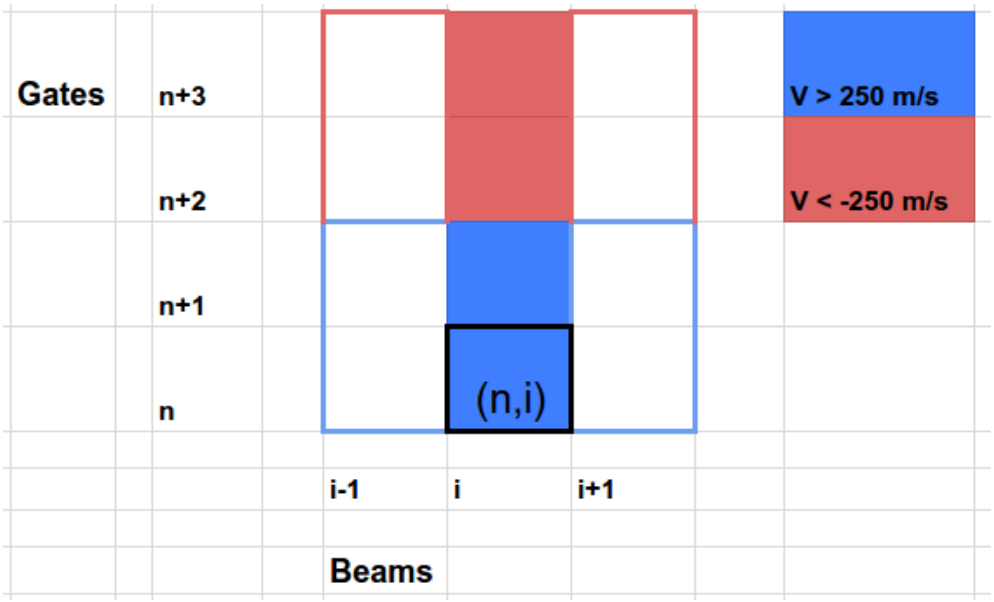

Figure 3.8: Illustration of how the algorithm operates to find RFEs. Range gate (n,i) represents the evaluated array in the flow matrix. To be marked as an RFE there need to be two consecutive range gates of velocity exceeding 250 m/s (or -250 m/s) and then at least two range gates of velocity in the opposite direction. For each of the flow domains at least one of the neighbour beams need to have similar velocity as well to make sure that it's not an error with one specific beam.

case studies of such special events will represent the second part of our results.

3.6.1 DaViTpy

The algorithms we have developed to discover Reversed Flow Events are written in the open source computer language Python[2]. The specific toolpack used for visualising the SuperDARN data is based on the Data Visualization Toolkit (DaViT) developed for IDL, and is now in the process of being made available through the Python programming language as DaViTpy.

DaViT, and initially DaViTpy, was a project developed at the university Virginia Tech to visualise and make use of the huge SuperDARN data sets produced by an increasing number of active radars. SuperDARN stores all raw and processed files at their servers at Virginia Tech, which is then being locally downloaded when researchers around the world request certain data sets. SuperDARN is a collaboration of several universities, and the development of DaViTpy is done together using the code sharing platform GitHub[3]. As of June 2017 the software library is actually not fully finished and still in Beta phase, with space physicists collaborating making the software better and more useful for everyone.

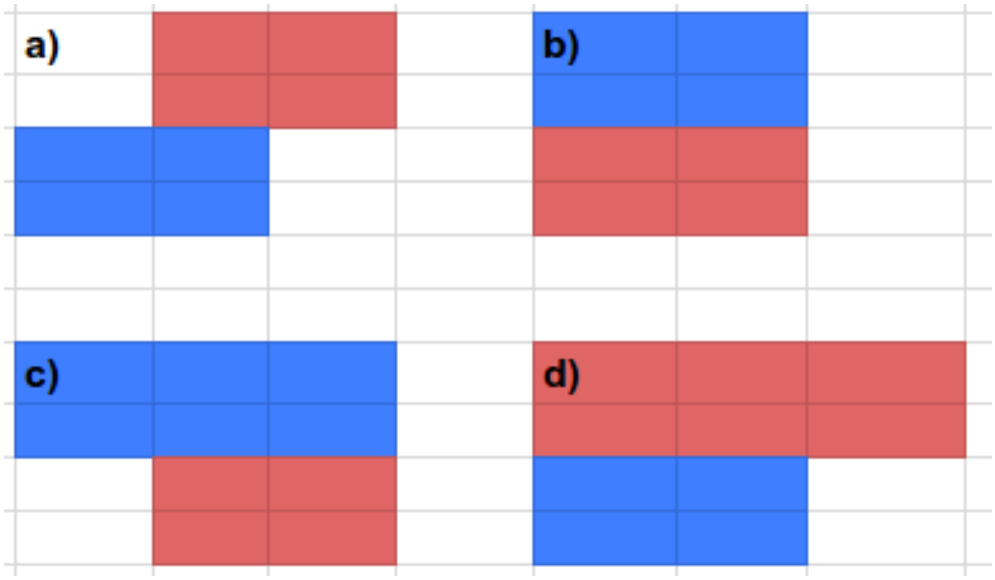

Figure 3.9: The areas a), b), c) and d) shows examples of different flow structures that all will be identified by the algorithm. Blue denotes flow towards the radar above 250 m/s, and red flow away from the radar with speed exceeding 250 m/s in opposite direction. Note that two consecutive range rages with flow in the same direction is common for all identified cases.

3.6.2 Search algorithm

For the work of this thesis we have focused on full radar scans from the above mentioned SuperDARN radars, which were used to determine if there were areas of reversed flow in opposite direction of the large scale flow with speeds exceeding 250 m/s in one direction, and surrounding flow of at least 250 m/s in the opposite direction. In the algorithm each radar scan is imported into an `m x n` matrix representing the number of beams (usually 16) times the number of range gates (usually 90). Successive range gates are then compared by the algorithm to see if they have a velocity shear of at least 500 m/s.

However, there are large portions of noise in the velocity data generating single range gates of a beam with large velocity shears. To mitigate this problem the algorithm was enhanced to only report reversed flows if there were at least two successive range gates with the same high velocity, and then at least two subsequent range gates of opposite velocity. To make sure this is not just random noise in one beam, the adjacent range gates are checked that at least one of them has the same high velocity as the centre beam.

The algorithm for determining if a matrix of velocity data potentially contains an RFE is available in Appendix C. The algorithm starts at the first range gate of the first beam, and then moves through all beams for each range gate. If the algorithm finds something, it returns the indices of the beam and range gate that satisfies the RFE selection criteria. If there are multiple flow shears in the scan, this is not evaluated, since the scan has already been marked as interesting and kept for later use. Figure 3.8 shows schematically how the algorithm evaluates a range gate in the search of RFEs.

[2]High-level general programming language first created by Guido van Rossum and released in 1991 `https://www.python.org/`

[3]The current version of DaViTpy can be freely downloaded from `https://github.com/vtsuperdarn/davitpy`

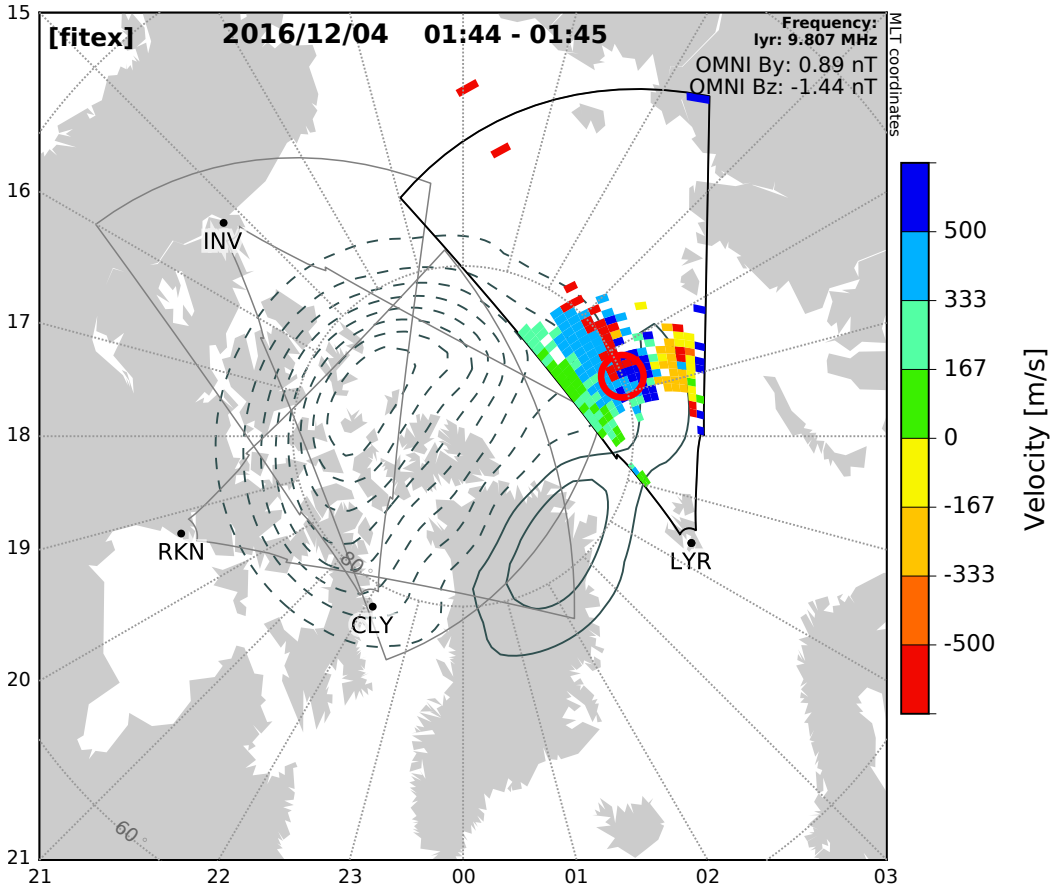

Figure 3.10: An example of how the algorithm has detected an RFE and a custom made plot has been generated. This particular example is from the Longyearbyen (LYR) radar from 04 December 2016. The red circle around 7 MLT denotes the flow shear marked as an RFE. On the top of the Figure is the scan type, date and time in UT, as well as the IMF conditions and the radar operating frequency.

Here at least two range gates of flow in each direction are marked with blue and red colors denoting opposite directions. Figure 3.9 shows different combinations of flow shear that all pass the algorithm for RFE detection.

For each RFE detected, the software adds an array in the RFE list structure, containing the radar site, beam, gate, magnetic longitude and latitude, as well as well as the MLT. UTC time stamps for the specific event are also recorded. Added from a custom made database is also IMF B_x, B_y and B_z which are stored in the RFE list.

When the software has finished analysing all scans in the pre-defined time range and for the selected radars, it continues to make plots marked with red circles identifying RFEs as well as embedding the IMF conditions and large-scale convection map from the SuperDARN database. An example can be seen in Figure 3.10, which shows RFE number 47 automatically detected by the developed software.

After all RFE scan plots are produced, a spreadsheet is also made for easy access and inspection. We have developed an extensive library of scripts and functions for collecting data and orbital parameters from SWARM, DMSP, NOAA and SWARM in addition to ground based data from SuperDARN and solar wind data from OMNI. Only the specific search algorithm is attached in Appendix C, but the entire software developed for

producing and plotting the results in this thesis is available in the GitHub repository at `https://github.com/ReedOnly/masterReed2017`. The search algorithm as an independent package also usable for finding enhanced flows and other features in the SuperDARN data can be found at `https://github.com/ReedOnly/superDARN-RFEfinder`.

Chapter 4

Results

This chapter presents the results and is divided into two parts. First we present several case studies of Reversed Flow Events (RFEs) found by the algorithm described in the instrumentation chapter. Afterwards follows a statistical summary of all identified RFEs, and the properties they have in common.

From December 2014 and December 2015, we have analysed in total 60 days of SuperDARN data from the three radars Clyde River (CLY), Inuvik (INV) and Rankin Inlet (RKN). The Longyearbyen SuperDARN radar started operating in 2016, and we have also analysed data from it in December 2016 and January 2017. The SuperDARN radars run 24 hours a day, and each radar produces one scan every minute, resulting in over 350 000 scans in the analysed time period. In this dataset we have identified 57 reversed flow events that satisfy the definition of *Rinne et al.* [2007] of flow of minimum 250 m/s in the opposite direction of the large-scale background flow, and a net flow shear of minimum 500 m/s.

Figure 4.1 shows a map with dots indicating the positions of identified RFEs in magnetic AACGM coordinates [*Baker and Wing*, 1989]. They are not sorted by IMF or MLT, so the Figure just shows the physical location relative to each radar. Most of the RFEs are found from radar scans from the Inuvik (INV), Rankin Inlet (RKN), and Clyde River (CLY) radars. For 2016 there are also a few examples from the Longyearbyen (LYR) radar. We also found one event that was detected by the Hankasalmi (HAN) radar in Finland. It has to be emphasized that the number of days for the three first radars is larger than that for HAN and LYR, so this map does not reveal anything about the occurrence rate of RFEs for different radars. The RFEs are also shown listed in Table 4.1. The events are numbered, which will be referred to when addressing specific events. Events later presented in case studies are marked in bold in the table. Full details about detected RFEs can be seen in Appendix B.

Both the INV and CLY radars have a field of view in a more zonal direction compared to the RKN which looks straight towards the magnetic pole. Because of geometry and the radars ability to only measure the line of sight velocity it should be expected that the CLY and INV radars will see more RFEs than the RKN radar. Previously, RFEs have mostly been seen in the east-west direction [*Rinne et al.*, 2007], which is not possible with the poleward aligned RKN radar. However, our analysis reveal that most RFEs are not flowing directly longitudinally, which allows them to be detected by the RKN radar as well. Because of its position, the RKN radar usually has good data coverage which increases the chances of seeing reversed flows.

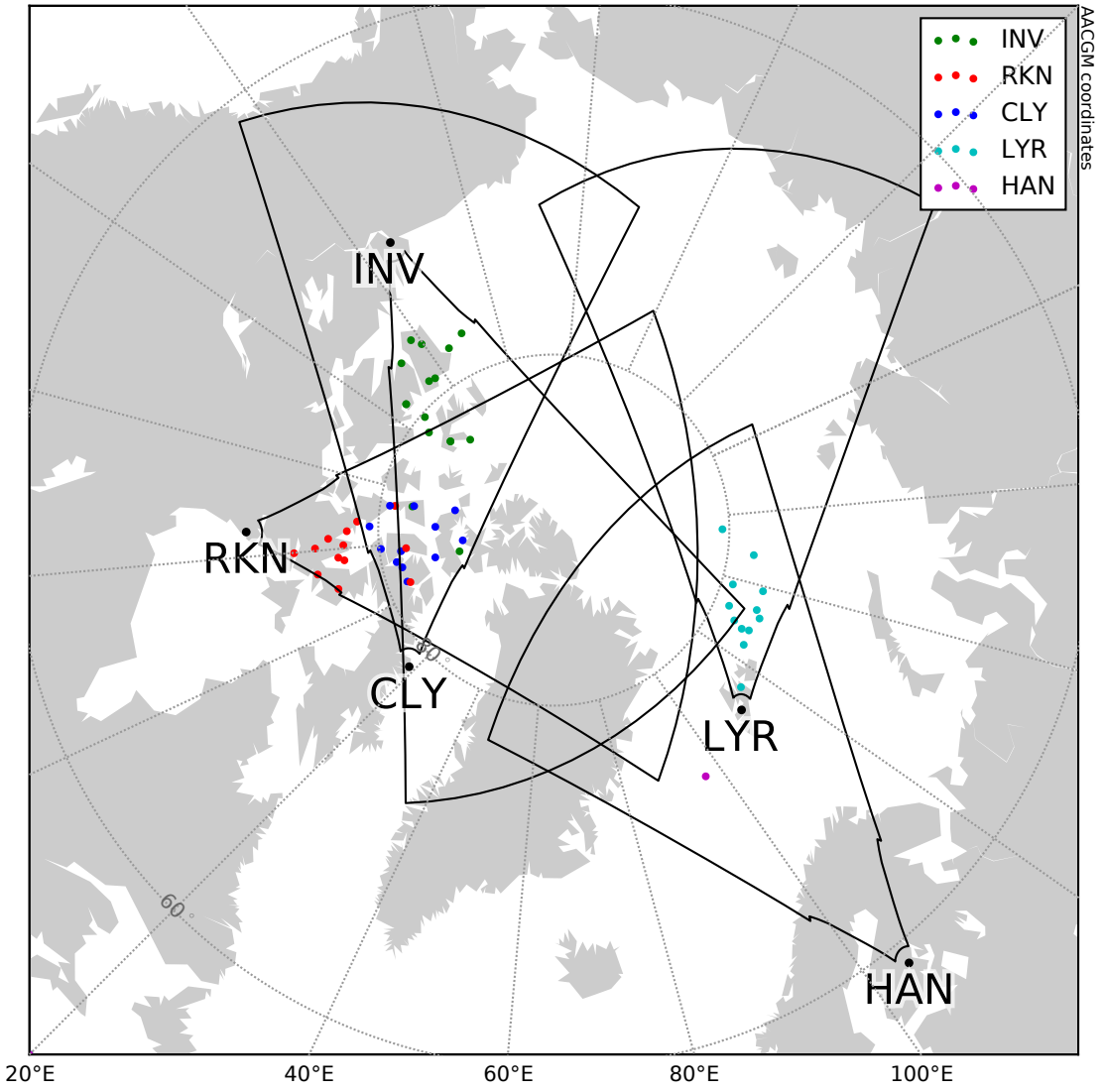

Figure 4.1: Location of the observed RFEs in the radar's field of view. Each point represents the centre of the RFE at the beginning of its discovery, and the color indicates which radar detected the RFE.

It should be noted that all reversed flows that fulfil the velocity and spatial RFE conditions as defined by *Rinne et al.* [2007] will be called RFEs in this chapter. The specific 21 RFEs found by *Rinne et al.* [2007] will be called Rinne-RFEs. However, since *Rinne et al.* [2007] only looked for RFEs close to local magnetic noon, they were all assumed to have the same physical origin. Our investigation has a less strict constraint, which allows us to identify RFE-like reversed flows during the full 24 hours of a day. As we will discuss later, the cusp RFEs might just be a small subcategory of a larger category of reversed flow channels that are found at different MLT.

Table 4.1: Summary of all RFEs found with the search algorithm during the targeted time intervals. Case studies presented is highlighted in bold. See Appendix B for full details about detected RFEs.

Nr.	Radar	Start time [yyyy/mm/dd]	UT [hh:mm]	Dur. [min]	Nr.	Radar	Start time [yyyy/mm/dd]	UT [hh:mm]	Dur. [min]
1	cly	2014/12/20	23:40	7	30	cly	2014/12/14	14:58	1
2	**inv**	**2014/12/16**	**00:14**	**49**	31	cly	2014/12/17	21:04	16
3	inv	2014/12/16	21:16	5	32	cly	2014/12/19	23:19	19
4	rkn	2015/12/10	18:39	1	33	han	2014/12/14	05:56	3
5	rkn	2015/12/11	13:53	9	34	inv	2014/12/01	11:42	9
6	rkn	2015/12/12	13:36	1	35	inv	2014/12/01	12:18	6
7	rkn	2015/12/12	17:32	1	36	inv	2014/12/01	15:35	25
8	rkn	2015/12/13	14:55	4	37	inv	2014/12/03	11:19	5
9	inv	2015/12/09	23:01	17	38	inv	2014/12/03	15:27	8
10	inv	2014/12/15	00:37	12	39	inv	2014/12/03	15:46	5
11	inv	2014/12/18	21:33	45	**40**	**inv**	**2014/12/04**	**07:10**	**22**
12	inv	2014/12/20	19:31	6	41	inv	2014/12/04	07:56	7
13	**rkn**	**2014/12/15**	**00:19**	**24**	**42**	**inv**	**2014/12/04**	**18:39**	**11**
14	inv	2014/12/01	16:07	15	43	inv	2014/12/08	14:00	11
15	rkn	2014/12/15	01:07	5	44	rkn	2014/12/10	11:00	9
16	rkn	2014/12/17	14:57	9	45	rkn	2014/12/11	10:19	1
17	rkn	2014/12/17	16:00	1	46	lyr	2016/12/01	07:46	7
18	rkn	2014/12/18	14:05	1	47	lyr	2016/12/04	01:44	1
19	rkn	2014/12/20	17:11	18	48	lyr	2016/12/04	11:06	9
20	cly	2014/12/03	11:12	31	49	lyr	2016/12/16	10:27	8
21	cly	2014/12/03	10:46	4	50	lyr	2016/12/17	03:24	11
22	cly	2014/12/03	21:32	9	51	lyr	2016/12/17	07:19	7
23	cly	2014/12/04	07:43	3	52	lyr	2016/12/17	08:57	17
24	cly	2014/12/04	10:31	10	53	lyr	2016/12/20	10:58	8
25	cly	2014/12/06	10:08	5	54	lyr	2016/12/22	04:16	6
26	cly	2014/12/08	22:01	5	55	lyr	2016/12/24	06:25	1
27	cly	2014/12/11	21:49	8	56	lyr	2016/12/25	04:42	3
28	**cly**	**2014/12/13**	**00:18**	**97**	57	lyr	2016/12/29	06:13	1
29	cly	2014/12/14	14:04	9					

4.1 Case studies

In the following section we will highlight the most interesting findings among the RFEs that we have discovered in the SuperDARN data sets. This includes an RFE lasting especially long, two simultaneously RFEs, and one event seen on the nightside, rather than the typical dayside Rinne-RFEs.

4.1.1 RFE seen with multiple radars

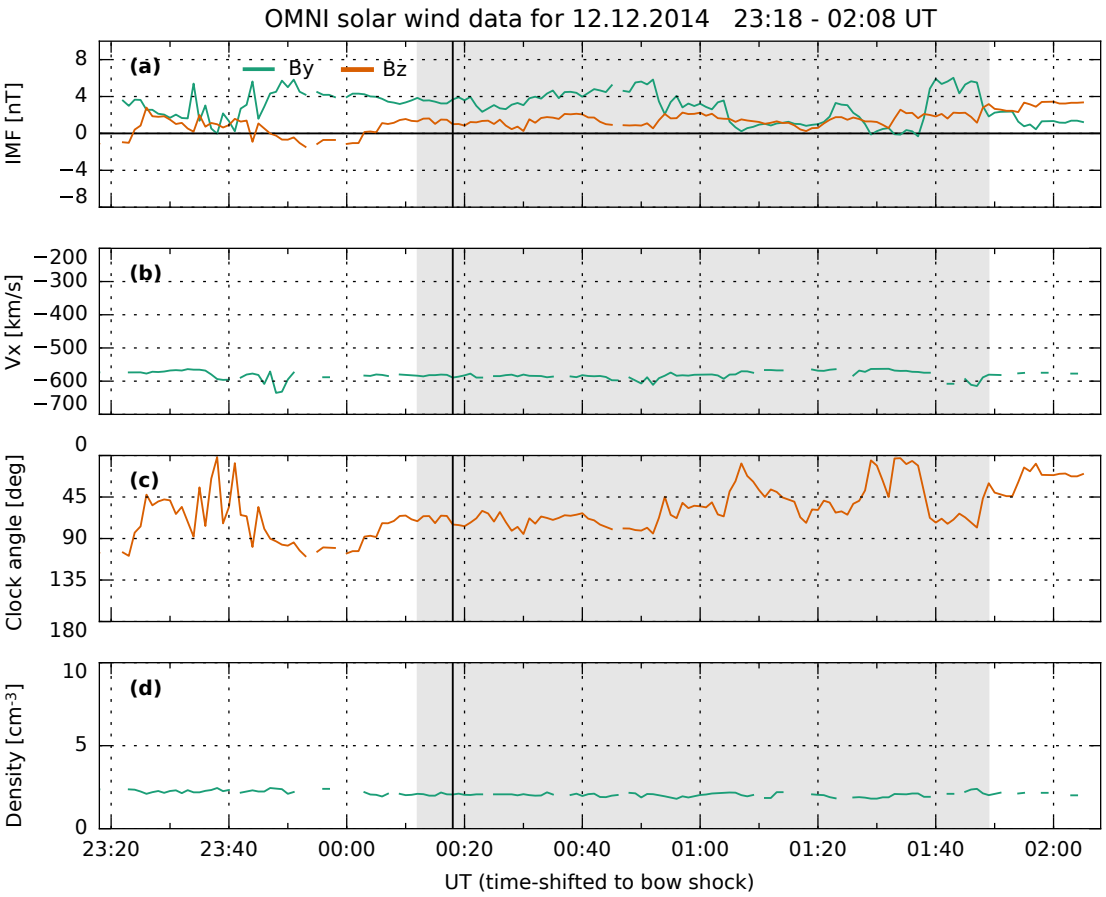

Figure 4.2: Solar wind conditions for RFE 28. Panel (a) shows the IMF B_y (green) and B_z (orange) components. Panel (b) shows the solar wind speed. Panel (c) shows the clock angle as defined in the text. Panel (d) shows the proton density of the incoming solar wind. All data are time shifted from L1 to the Earth's bow shock.

The first event we will discuss is a reversed flow seen simultaneously by several of the polar cap radars from 00:18 - 01:54 UT on 13 December 2014. This is the longest lasting RFE in our dataset lasting 97 minutes.

Figure 4.2 shows the OMNI solar wind conditions as recorded by the ACE satellite and time shifted to the bow shock. The solid vertical line marks the onset of the event in UT, while the grey shaded area shows the duration of the event when we apply a 6 minute time-shift to account for a conservative estimate for the propagation from the bow shock to the ionospheric responses [*Moen et al.*, 1999; *Jackel et al.*, 2012]. Panel (a) displays IMF B_y and B_z. B_y is positive between 0 and 5 nT during the entire event,

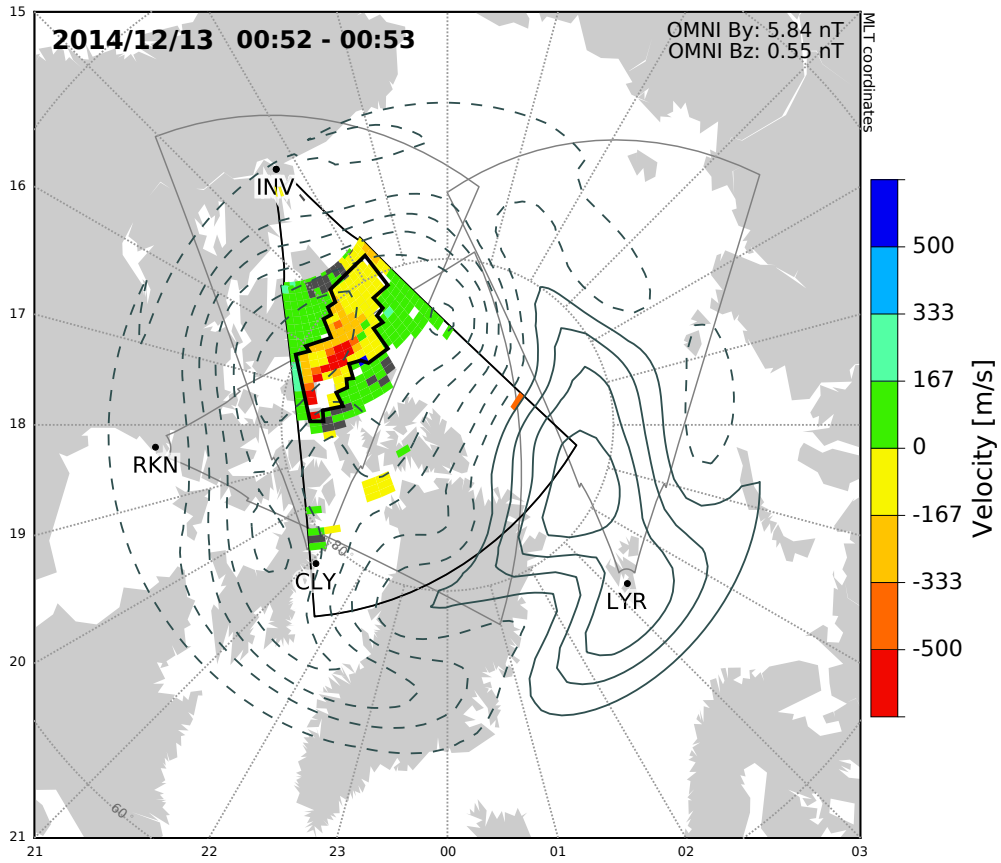

Figure 4.3: RFE 28 in red and yellow color flows in the sunward direction seen by the Clyde River (CLY) radar on 18 December 2014 at 00:52 UT. A black outline highlights the RFE. The data is plotted in magnetic coordinates with noon MLT pointing up. The equipotential contours of the large-scale convection pattern are overlaid using black solid and dashed lines.

as well as up to an hour before the event. B_z is only slightly positive and fluctuating slightly negative around 30 minutes before the onset of the event.

Panel (b) shows the solar wind speed. The speed V_x is stable at -600 km/s indicating relatively fast solar wind towards the Earth.

Panel (c) shows the clock angle of the IMF. The clock angle is defined as $\theta = tan^{-1}(|B_y/B_z|)$ for $B_z > 0$ and $\theta = 180° - tan^{-1}(|B_y/B_z|)$ for $B_z < 0$. Consequently southward IMF will be shown as $\theta > 90°$. For this event we see that the IMF is mostly B_y dominated with shortly due north IMF ($\theta < 45°$) around 20 minutes before the radar observations of the RFE.

Panel (d) shows the proton density N_i in the solar wind. The density is low between 2-3 particles per cm^3, but is related to the fast speed, which results in lower density.

The data gaps are usually a result of insufficient data coverage, but can also be a consequence of fluctuations in solar wind speed causing anomalies in the time shifting from L1 to the bow shock.

Figure 4.3 shows an example of a RFE from the Inuvik (INV) SuperDARN radar when also the radars Clyde River (CLY) and Rankin Inlet (RKN) had good data coverage. We can see the line of sight velocity of the backscattered ionospheric signal where blue indicates fast flow (300-500 m/s) towards the radar and green slower speed (less

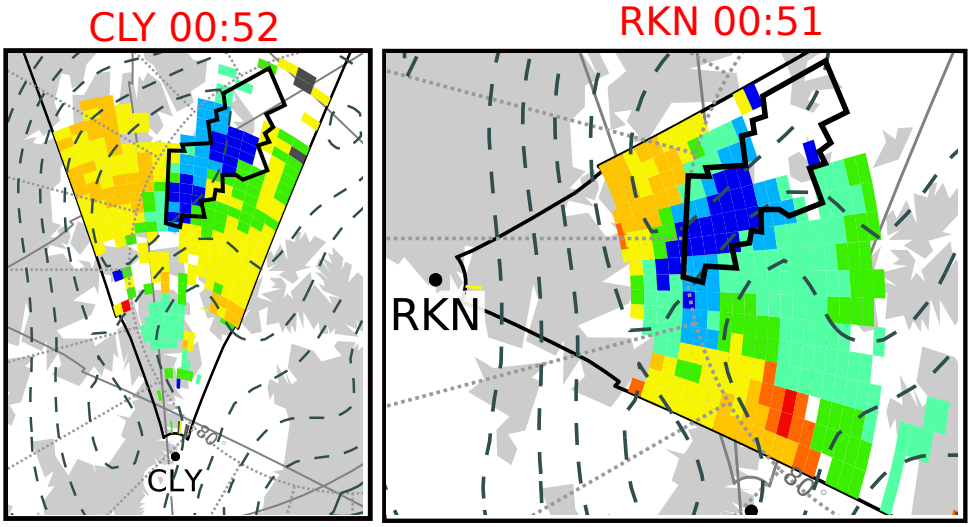

Figure 4.4: Comparison of RFE from Figure 4.3 also seen by the Clyde River (CLY) and Rankin Inlet (RKN) radars simultaneously. Blue color indicates southward flow. We see that the location of the flow channel is matching well across the radars. The black outline from the INV radar is overlaid on top of both the CLY and RKN fields of view.

than 300 m/s) towards the radar. Red represents fast flow (300-500 m/s) away from the radar. The radar data is plotted in magnetic AACGM coordinates, see Appendix A. The orientation of the map is Magnetic Local Time (MLT) with local noon always pointing up. The local time is displayed around the edges of the figure. Backscatter resulting from ground scatter rather than the intended ionospheric scatter is marked with grey color in the scans. Overlaid are also the equipotential contours of the cross polar potential, which indicates the direction of the large scale plasma convection due to $\mathbf{E}\times\mathbf{B}$ drift. These contours are based on all available radar data at the time as well as the solar wind conditions. In areas of little data the contour is based on large-scale static models. The flow contours therefore don't take into account any small-scale features in the flow, but it gives an indication of the large-scale convection. For reference, the field of view of the other polar radars are also shown on the map. The date and time of the scan in UT, as well as IMF conditions, are also shown on top of the figure.

From Figure 4.3 we see that there is a flow channel moving away from the radar in red overlaid with a black outline. The channel is located in the post noon inflow region between 14 -17 MLT at $\sim 83°$ magnetic latitude. The speed inside the flow channel is up to 500 m/s in the opposite direction of the large-scale flow and therefore categorized as an RFE. The surrounding flow is slower(around 100 m/s in opposite direction). According to the definition by *Rinne et al.* [2007] the flow channel in this particular scan therefore does not fulfil the RFE criteria, but in earlier and subsequent scans the background flow is also larger than 250 m/s. As we will see from scans from other radars, this low speed is also a result of the radar only measuring line of sight, while the flow in reality might be much larger, but in a direction somewhat perpendicular to the radar field of view.

Figure 4.4 shows the same flow channel from the two other radars RKN and CLY at approximately the same time. The color scaling is the same as in Figure 4.3. We can see that the flow channel is visible in both the CLY and RKN radars. The black outlining

is the position seen with the INV radar in Figure 4.3, which confirms the coexistence of the flow channel in all three radars. The RKN radar also confirms that there is an east-west component of the flow of around 300 m/s equatorward of the radar. This makes it a good candidate for testing the location determination of the backscattered signal, since the three radars are operating independently of each other. It shows very good agreement with the observations, which suggests that the SuperDARN range determination is working well in accordance with studies by *Yeoman et al.* [2001] and *Chen et al.* [2016].

Because of the slightly positive B_z during the event, this is most likely an example of two flow reversals seen in a post-noon lobe cell, as represented in panel A) of Figure 2.17.

DMSP and SWARM intersecting the RFE

For this particular event the SWARM-B spacecraft passed directly through the RFE at the beginning of the event from 00:20 to 00:21 UT as seen in Figure 4.5b. In this projection red color represents flow towards the radar and blue color away. The RFE channel is the encircled blue channel with flow towards dayside noon. The projection is the same as in the previous SuperDARN scans, with noon MLT pointing up.

At 00:15 UT, around 15 minutes prior to the SuperDARN scan the DMSP F18 satellite also passes slightly equatorward of the RFE. The observed UV aurora is overlaid in Figure 4.5b in green color with radiance represented in Rayleigh (R) shown by the bottom colorbar. The outer green auroral oval shows that the RFE is well inside the polar cap.

The ground tracks of both spacecrafts are shown with a blue line for DMSP and red line for SWARM-B with circles marking every minute along the trajectory.

The field-aligned current density measured from the SWARM-B spacecraft is shown in Figure 4.5a. The time of the RFE is highlighted by grey shading. The current determined from magnetic field measurements using Amperes law shows downward Field Aligned Current density as positive values, represented by the blue line. The uncertainty in the measurements is represented with the red line. We see that there are weak currents in the shape of thin current sheets alternating between downward and upward FAC in association with the RFE.

The current sheets are easiest to see on the equatorward side of the RFE, from 00:21:00 to 00:21:30 UT. In Figure 4.5a, upward currents are shown with positive values. *Southwood* [1987] and *Oksavik et al.* [2004] have described that the RFEs should be associated with FACs. However, the SWARM data are so fine structured that it is difficult to see a simple relationship like the one described by *Southwood* [1987]. It could be that the RFE has internal fine-structure when it comes to currents, or the flow may be structured at smaller spatial scales than the SuperDARN can resolve. Rocket data [*Oksavik et al.*, 2012] have identified structures in the plasma flow down to spatial scales of just a few kilometers, and it is possible that this is what SWARM is also seeing. It should be pointed out that the strongest currents are seen around 00:22 UT, when the SWARM-B enters the postnoon auroral oval.

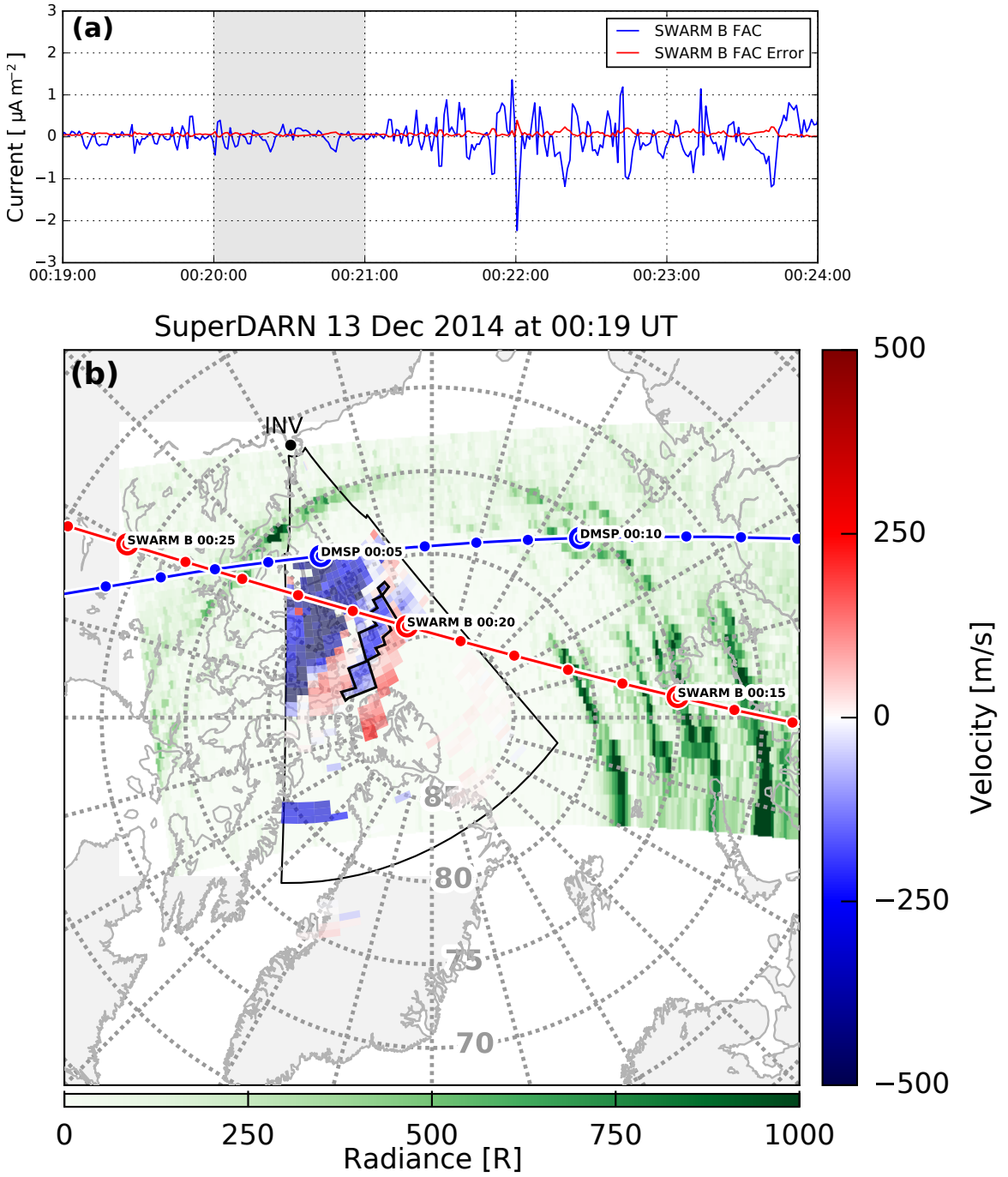

Figure 4.5: SWARM B in Panel (a) shows the Field Aligned Currents (FACs) when the spacecraft intersect RFE 28. Blue represents the measured current, while red is the error of the measurements. It is seen that there are weak filaments of upward and downward currents in connection with the RFE from 00:21-00:22 UT corresponding to the equatorward side of the RFE. The strongest currents are found when the spacecraft enters the postnoon auroral oval around 00:22 UT. In panel (b) the blue RFE 28 seen by the Inuvik (INV) radar on 13 December 2014 at 00:19 UT is shown using a black contour. Red represents flow towards the radar in this map. Trajectories from SWARM B and DMSP F18 are overlaid.

MetOp-A intersecting the RFE

Towards the end of RFE 28 the MetOp-A spacecraft passed directly over the RFE from 00:36-00:39 UT. The spacecraft ground track is shown in green with markers every minute along the track in Figure 4.6b. The DMSP F18 spacecraft with UV auroral imaging passes approximately simultaneous and its orbit is shown in blue.

Particle measurements from the MetOp-A MEPED instrument are shown in panel (a). The > 30 keV electron sensor is the most important for our purpose of identifying the OCB (shown with solid vertical lines in Figure 4.6a). Poleward of the OCB there are no magnetopsheric particles, indicating open magnetic field lines. There is very little electron and proton flux in the area where the RFE is located. The OCB is marked with red crosses in Figure 4.6b, which confirms that the RFE is well within the polar cap. From the DMSP data we see that there is a polar cap arc stretching equatorward on the dusk side of Figure 4.6b. Due to DMSPs long recurrence rate (101 mins) and limited ground observation we have not been able to confirm whether the arc is moving.

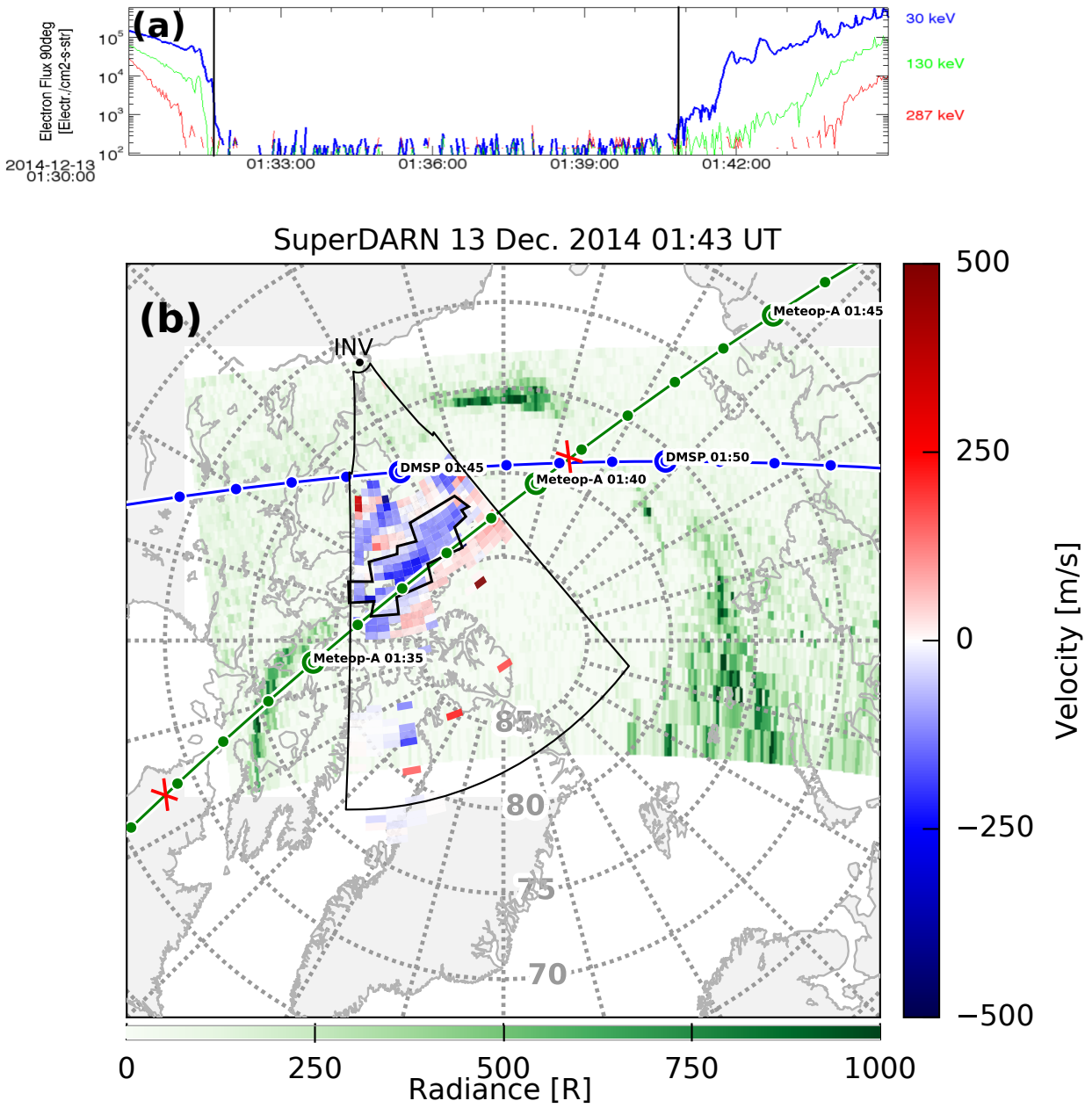

Figure 4.6: (a) shows MEPED data for energetic > 30 keV electron precipitation for the event. In (b) the blue RFE 28 is seen by the Inuvik (INV) radar on 13 December 2014 at 01:43 UT is shown using a black contour. Red represents flow towards the radar. Trajectories from MetOp-A and DMSP F18 are overlaid onto the map. Two red marks in (b) are used to indicate the OCB based on the MetOp-A data.

4.1.2 Lobe cell RFE

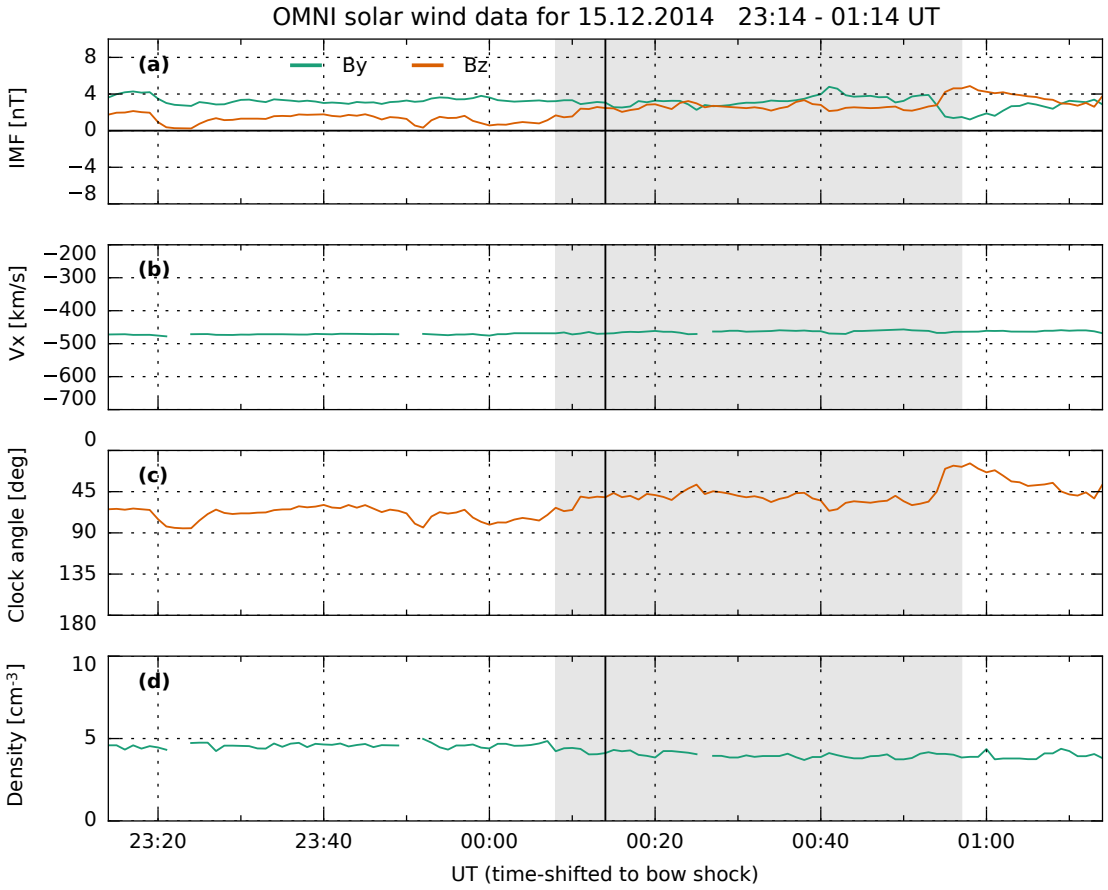

Figure 4.7: Solar wind conditions for RFE 2. Panel (a) shows the IMF B_y (green) and B_z (brown) components. Panel (b) shows the solar wind speed. Panel (c) shows the clock angle. Panel (d) shows the particle density in the incoming solar wind. All data are time shifted from L1 to the Earth's bow shock.

The following event shows RFE 2 seen by the SuperDARN INV radar on 16 December 2014 which lasted 49 minutes from 00:14 to 01:03 UT. The event occurred for stable positive IMF B_y and B_z conditions as seen in Figure 4.7. A clock angle between $45° - 90°$ up to an hour before the event means the solar wind conditions is B_y dominated for northward IMF. The conditions are therefore ideal for lobe reconnection. The solar wind flow speed is stable around 490 km/s with a density around 4 cm^{-3}. This means that the dayside reconnection region most likely will be shifted prenoon because of the magnetic tension force [*Cowley et al.*, 1991]. This is also confirmed by the large-scale convection pattern that has been overlaid in Figure 4.8.

Figure 4.8b shows the LOS velocity for the Inuvik (INV) radar on 16 December 2014 at 00:38 UT. This is in the middle of the event, and around the time the reversed flow is at it's strongest. Blue color denotes flow towards the radar, while red denotes flow away. The coordinate system is using magnetic AACGM latitude and MLT longitude. We can see that there is strong sunward flow against the background flow towards the dayside seen as blue color in the radar plot outlined with a black contour. On either side of the radar there is strong poleward flow away from the radar seen in red.

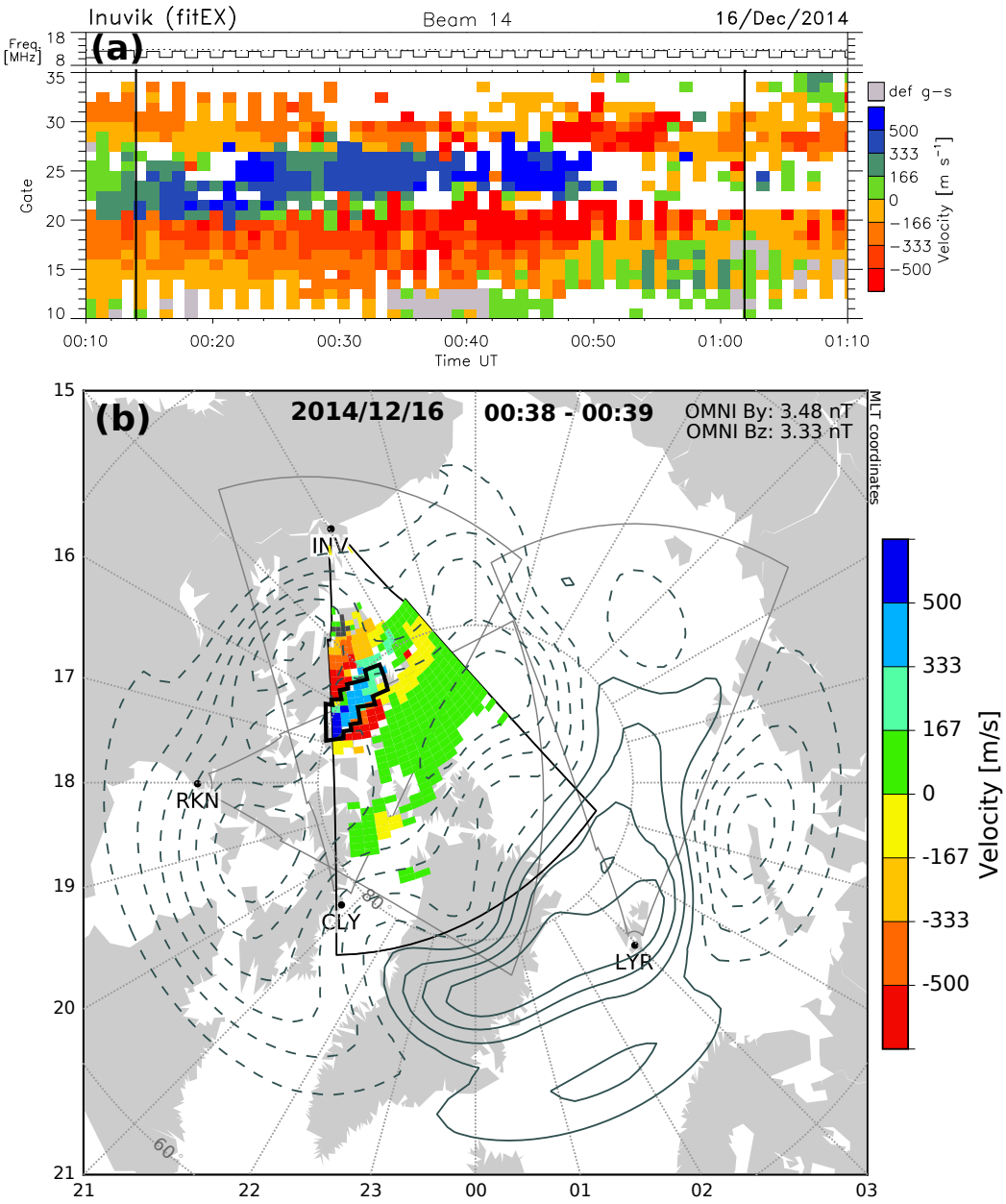

Figure 4.8: Panel (b) shows RFE 2 indicated by a black contour in the Inuvik (INV) SuperDARN radar scan on 16 December 2014 at 00:38 UT. The RFE is located in the postnoon sector between 14-17 MLT. B_y and B_z are positive, which for northward IMF is favourable a lobe cell in the postnoon sector. Panel (a) shows the velocity data from beam 14 as a function of range gate. The RFE is clearly seen in blue between the start and end times marked with vertical lines.

This is an example of an event that fulfils the RFE criteria, but is still consistent with the flow direction based on large scale convection associated with lobe cells, which has reconnection north of the equatorial plane due to positive B_z, and thus causes a sunward flow different from the normal two cell convection [*Reiff and Burch*, 1985]. This configuration resembles the cell configuration from panel A) in 2.17. We will discuss this phenomena in more depth later.

Figure 4.8a shows the LOS velocity data for Beam 14 for the full duration of the RFE. The beginning and end of the RFE is indicated by vertical lines. Here we can clearly see the RFE in blue color in gate 21-27 from 00:15-00:50 UT. The reason why the RFE disappears at the very end is most likely due to missing backscatter for this area. In other beams the RFE is visible at the end as well. When looking closely at the backscatter in panel (a) it can be seen that the backscatter is somewhat alternating for every second scan. This is a result of the radar alternating between two frequencies of 12.2 MHz and 12.4 MHz which has different propagation characteristics in the ionosphere.

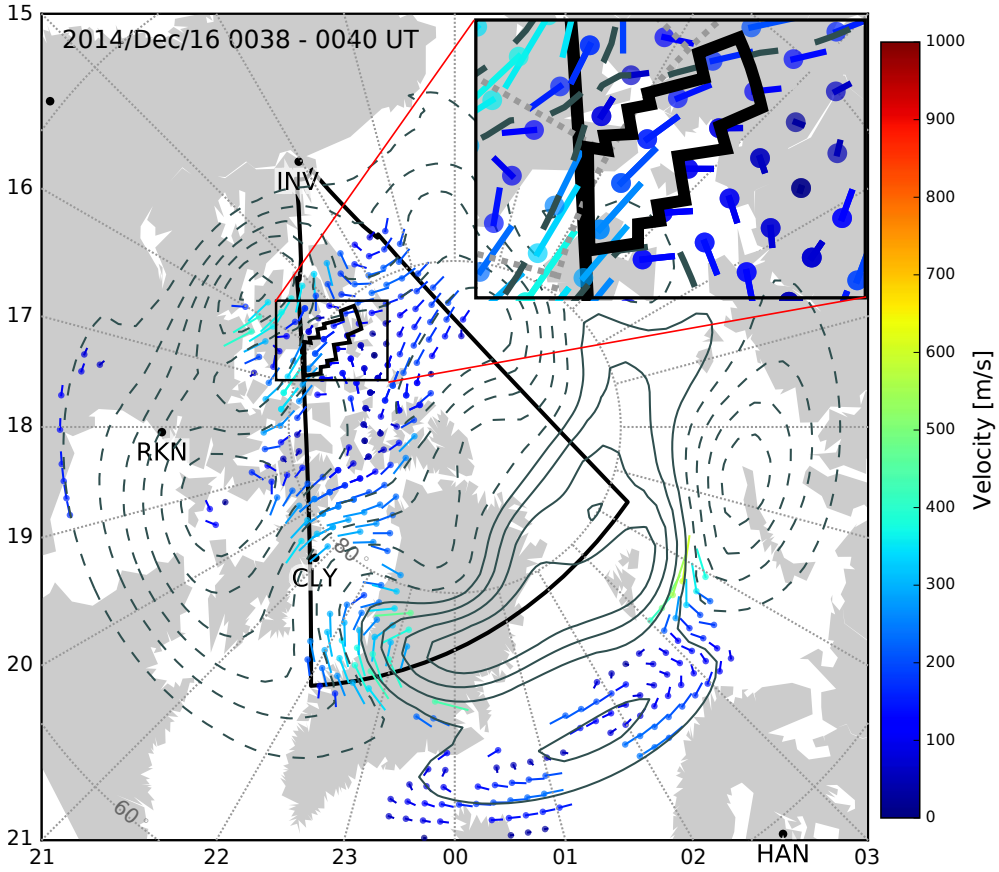

Figure 4.9: Fitted velocity vectors for all available SuperDARN radars for RFE 2. Overlaid the map is the black contour from Figure 4.8. The arrows show movement starting from the arrowhead onwards. The enlarged clip in the upper right corner shows the area surrounding the RFE. We see that the fitted velocities agree with the LOS velocities from the INV radar.

Figure 4.9 shows the fitted vector velocities for all available SuperDARN radars at the same time as the scan for RFE 2 at 00:38 UT. The arrows show movement starting from the arrowhead onwards. As we can see from the Figure, there are several velocity

shears within the polar cap justifying the existence of an RFE. The enlarged clip in the upper right corner shows the area surrounding the RFE. We can see that inside the RFE contour there are sunward flow of ∼300 m/s while on the poleward side the flow is ∼200 m/s poleward. On the sunward side of the RFE is somewhat more towards the dusk side with speeds reaching 400 m/s. Overall we notice that the fitted velocities agree well with the LOS velocities from the INV radar.

Satellite passes

RFE 2 is located in the polar cap close to the dayside open closed boundary (OCB) as seen in panel (c) of Figure 4.10. There is an auroral arc located directly underneath the centre flux of the RFE flow which is outlined in black. Shown are also the trajectories from DMSP, SWARM-A and MetOp-A. The OCB from the electron particle flux is shown in panel (b) and marked with red crosses in panel (c). The dayside boundary seems consistent with the auroral oval seen in the same region by DMSP around 1 minute earlier, which means the two measurements are very comparable.

SWARM A and C fly around 200-300 km away from the RFE and towards the dayside. The two trajectories are more or less similar and at the same time, so only SWARM-A is marked with a red line in panel (c). The field-aligned current (FAC) from the two SWARM spacecrafts are seen in panel (a) of Figure 4.10. Although there are no available radar coverage across the SWARM track, the flow channel of RFE 2 is likely extending towards the area passed by SWARM. The SWARM data shows that there are strong sheets of FAC as the satellites intersect the OCB from 00:47 -00:49 UT. The blue line shows the downward current density measured by SWARM A, the green line SWARM C, and the red line is a combination of the two datasets. This data has smaller uncertainty, but at the cost of less temporal resolution. The data from SWARM A and C correlate with a few seconds delay, showing consistence of the two datasets. Figure 4.10a shows there is a positive (downward) current on the poleward side of the auroral oval, and a negative (upward) current equatorward of the oval.

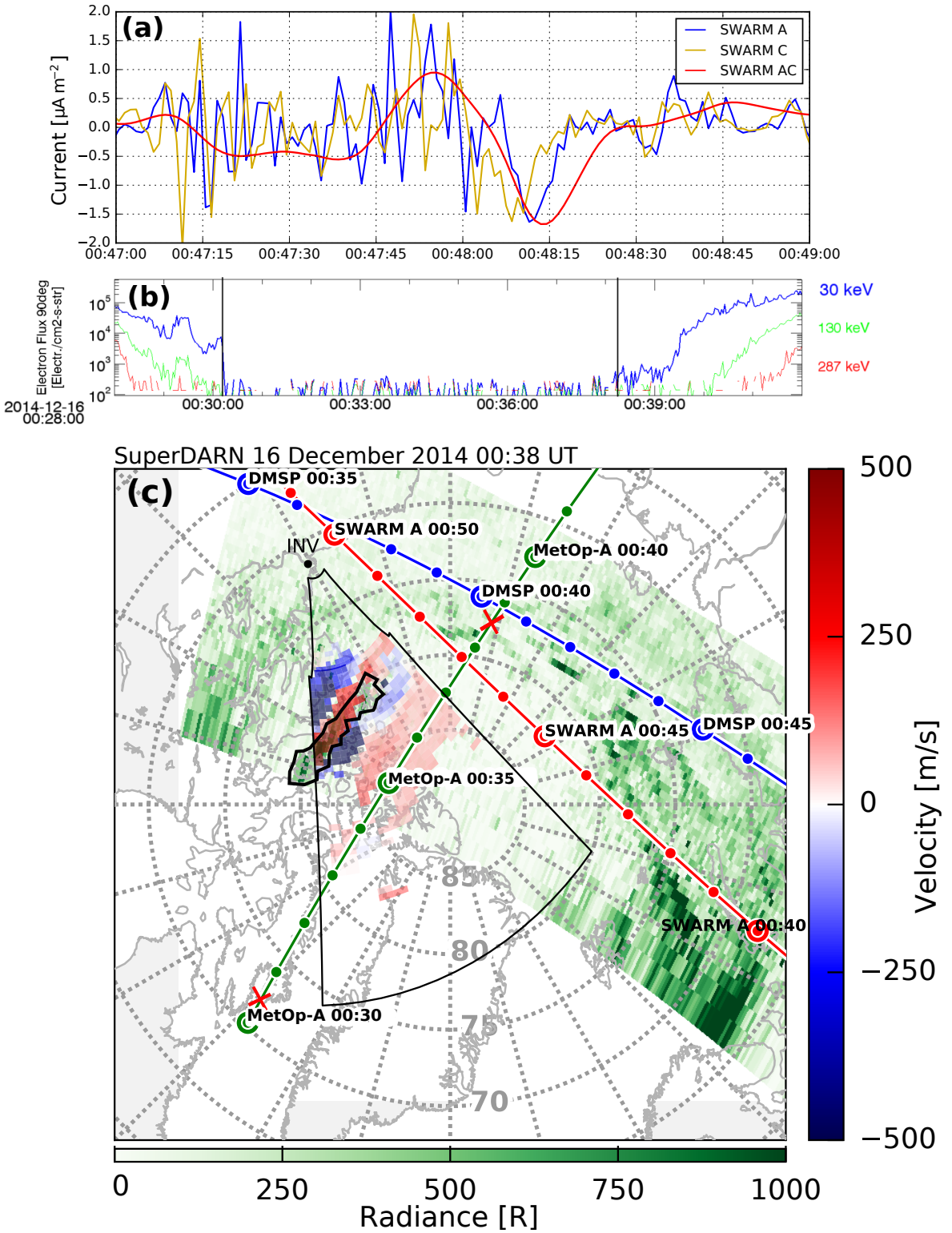

Figure 4.10: RFE 2 seen simultaneously by MetOp-A and SWARM spacecrafts. Panel (a) shows the Field-Aligned Currents (FAC) as recorded by the SWARM A and C spacecraft. Downward currents are shown positive in the graph. Panel (b) shows trapped $>$ 30 keV electrons by the MetOp-A MEPED instrument. Panel (c) shows the RFE in red overlaid on top of the UV aurora as recorded by the DMSP F16 satellite. Red is sunward flow as seen by the INV SuperDARN radar. There is a clear correspondence between the green auroral arc and the flow channel. Fluctuations in the FAC can be seen as SWARM passes equatorward of the RFE.

Backscatter power

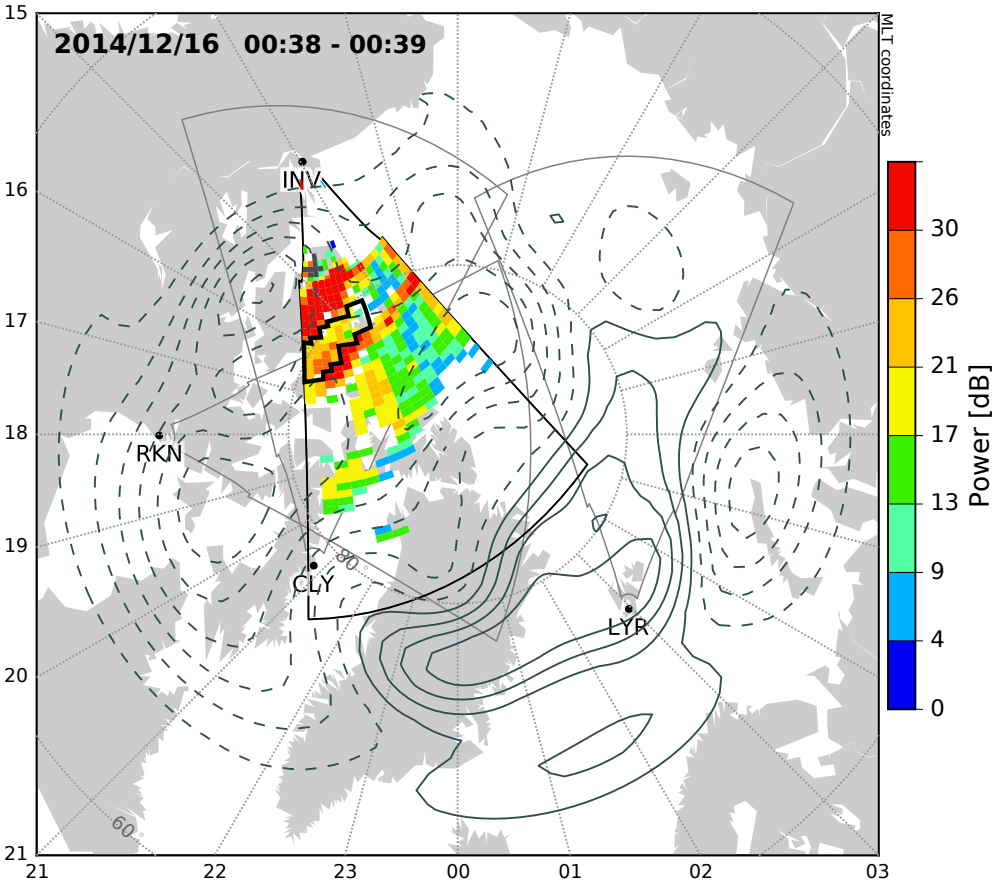

Figure 4.11: SuperDARN backscatter power associated with RFE 2 which is indicated by the black contour. We note that the backscattered power is smaller in the outlined black area than in the area surrounding the RFE.

For RFE 2 there is a weakening in the backscatter power as we can see in Figure 4.11 where the backscattered power for the RFE is shown inside the black contour line around 17 -21 dB, while the enhanced flows on each side of the RFE have backscatter power stronger than 30 dB. This enhanced backscatter on the boundaries is in agreement with the findings of *Oksavik et al.* [2011] which studied decameter irregularities set up by the flow shear from the RFE. As the SuperDARN backscatter is a result of plasma irregularities, it is expected to see enhanced backscatter at the flow reversals.

4.1.3 Nightside RFE

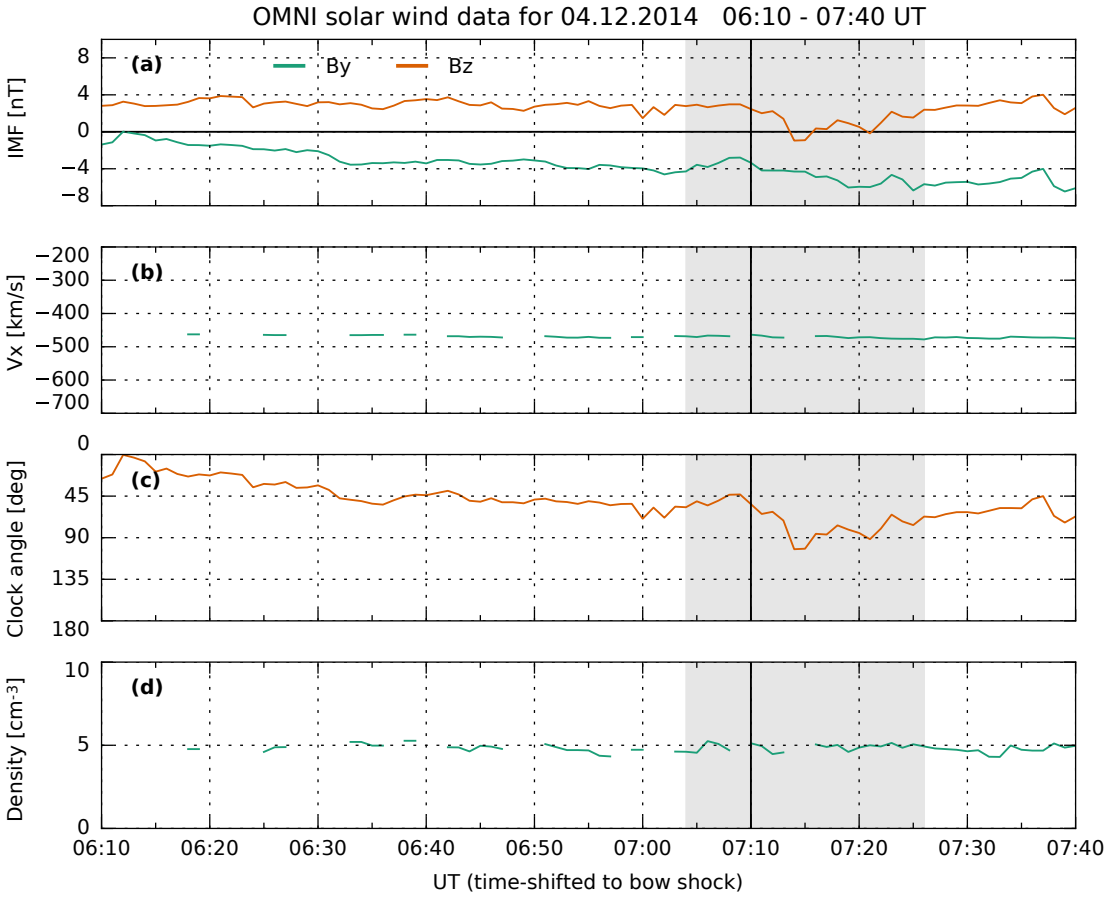

Figure 4.12: Solar wind conditions for RFE 40. Panel (a) shows the IMF B_y (green) and B_z (brown) components. Panel (b) shows the solar wind speed. Panel (c) shows the clock angle as defined in the text. Panel (d) shows the density of the incoming solar wind. All data are time shifted from L1 to the Earth's bow shock.

Figure 4.13 shows an example of a nightside RFE with sunward flow (orange) of $\sim$ 300 m/s opposing the large scale flow at $\sim$ 500 m/s as observed by the INV SuperDARN radar. This happens at a time of predominantly positive IMF B_z as well as strongly negative B_y as seen in Figure 4.12. The clock angle is close to 45° up to an hour before the event, which indicates $|B_y| \approx |B_z|$ and B_y strongly negative. The solar wind speed was around 500 m/s, and the particle density 5 cm^{-3}, which is representative of average solar wind conditions. The event lasts 22 minutes before it fades away. Overlaid Figure 4.13 is also UV aurora from DMSP F17 $\sim$20 minutes after the RFE has ended. From the UV data we can see that there is a strong auroral oval in the post-noon sector. Due to the RFEs location poleward of the auroral, the RFE is most likely on open field lines.

This event would have been ideal to check for optical imaging, to see if there is any auroral streamers related to auroral streamers as observed by *Sergeev et al.* [2004]. Unfortunately it is cloudy over northern Canada at the time of the RFE, so the otherwise available all-sky auroral cameras are unable to confirm this. There are also no DMSP satellites passing directly over the RFE which could confirm the existence of an auroral

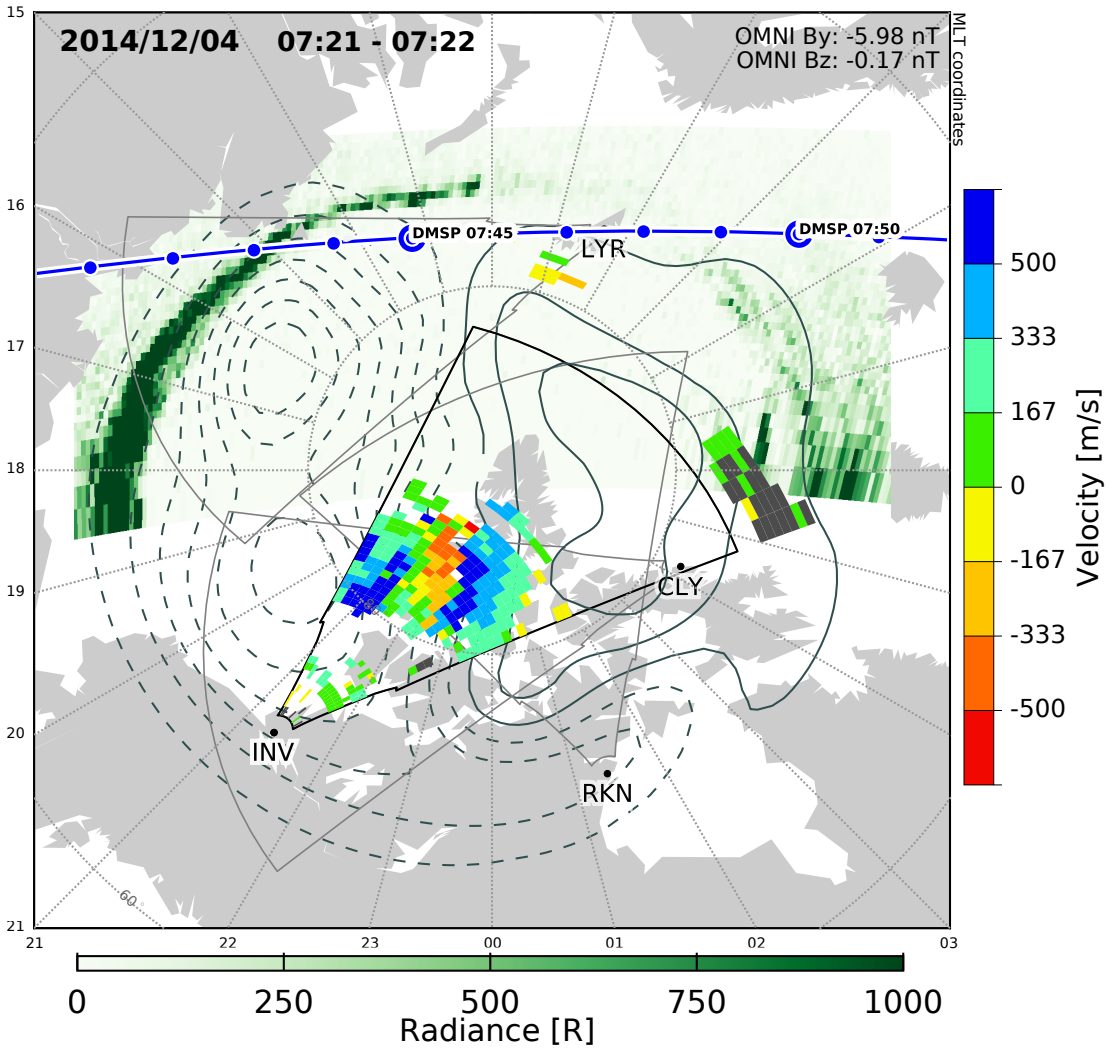

Figure 4.13: RFE 40 from the Inuvik (INV) radar near 22 MLT. The RFE is the yellow/orange area of sunward flow (away from the radar), which is located between strong anti-sunward flow (blue) which is expected for old open flux in the nightside polar cap. The auroral oval from DMSP F17 pass ∼20 min later indicates that the RFE is located on open field lines.

streamer.

4.1.4 Two Simultaneously RFEs

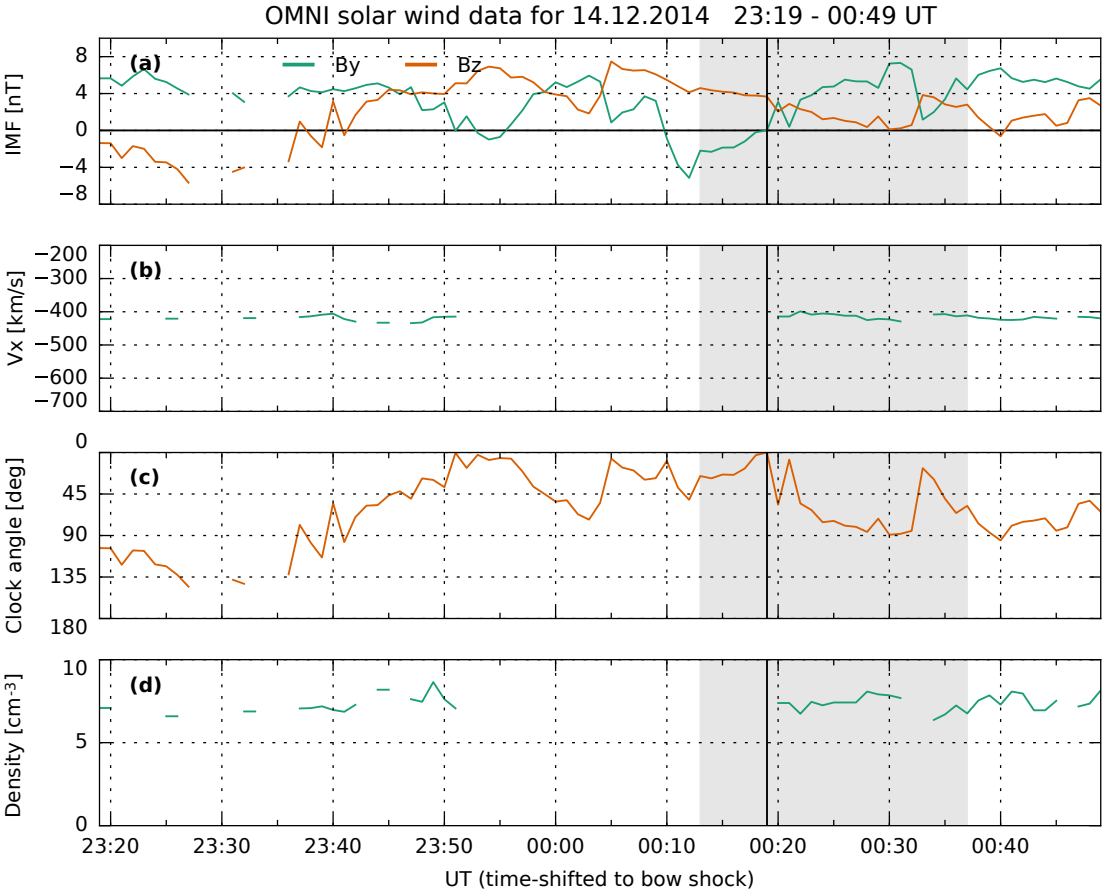

Figure 4.14: Solar wind conditions for RFE 13. Panel (a) shows the IMF B_y (green) and B_z (brown) components. Panel (b) shows the solar wind speed. Panel (c) shows the clock angle as defined in the text. Panel (d) shows the density in the incoming solar wind. All data are time shifted from L1 to the Earth's bow shock.

Figure 4.15 shows an example of a double RFE observed in the dusk sector around 15 MLT. In panel (a) of Figure 4.15 we can see a centre flow channel in red color at 00:29 UT on 15 December 2014 observed by the RKN radar. This flow is away from the radar in the polar cap at 81° magnetic latitude (MLAT). Simultaneously as the centre flux develops, we can see two reversed flows on each side in blue color moving towards the RKN radar. The flow intensifies until 00:31 UT as seen in panel (b), before it starts fading around 00:39 UT. The event was observed for a total of around 25 minutes.

From Figure 4.14 we can see that both IMF B_y and B_z are highly turbulent both before and during the event. B_z has been positive for an extended time period prior to this event, but approaches zero around the time the RFE is seen in the SuperDARN scans. B_y was positive before the event, but around 00:10 UT it dropped quickly negative, which indicates a rapid change in the location of the reconnection site at the magnetopause from pre-noon to post-noon where this event is observed. The clock angle is mostly $< 45°$ and on several occasions reaching 0°. This means the IMF is due north, with dominant component alternating between $|B_y|$ and $|B_z|$.

The velocity is relatively stable at 400 m/s which is rather slow. The density

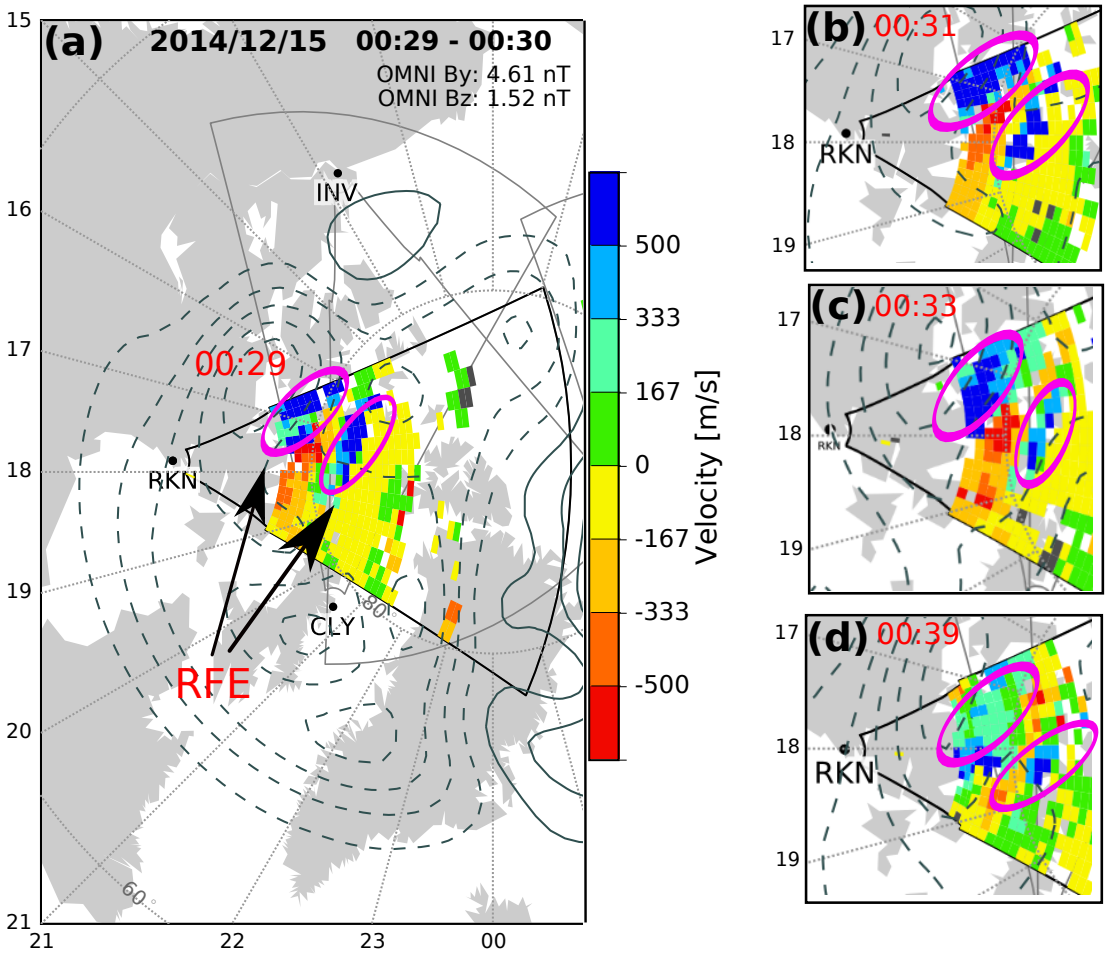

Figure 4.15: RFE 13 from the Inuvik (INV) radar consisting of two anti-sunward flow channels (blue) that are opposed to the large scale background flow. The event is located in the postnoon sector, in an area of flow towards the inflow region, which is expected at this local time and magnetic latitude. From panel (a) we can see how two simultaneously RFEs develop at 00:29 UT, separated by a strong centre flux in the opposite direction (red color). It intensifies in panel (b) at 00:31 UT which sustains until 00:33 UT in panel (c). Eventually the RFE and centre flux fades away around 00:39 UT as seen in panel (d).

reaching the bow shock is high, between 7-9 cm^{-3}. It is also worth noting that the particle density is not stable, but somewhat turbulent compared with the other events.

Unfortunately, there are no satellite passes during this event, so there is no data to confirm the location of the OCB. The location at 81° magnetic latitude makes the RFE however very likely to be deep inside the polar cap.

Due to its far location post-noon, this is most likely an example of lobe cell reconnection. Nevertheless, due to the simultaneous growth and decay of both reversed flow channels, it can also possibly be the ionospheric response of an Southwood FTE where the centre flux represents a newly reconnected field line [*Southwood*, 1987]. Since the IMF B_y is positive prior to the event it also makes the inflow region shift post-noon [*Ruohoniemi and Greenwald*, 2005]. We will assess this issue further in the discussion chapter.

4.1.5 Non-stationary RFE

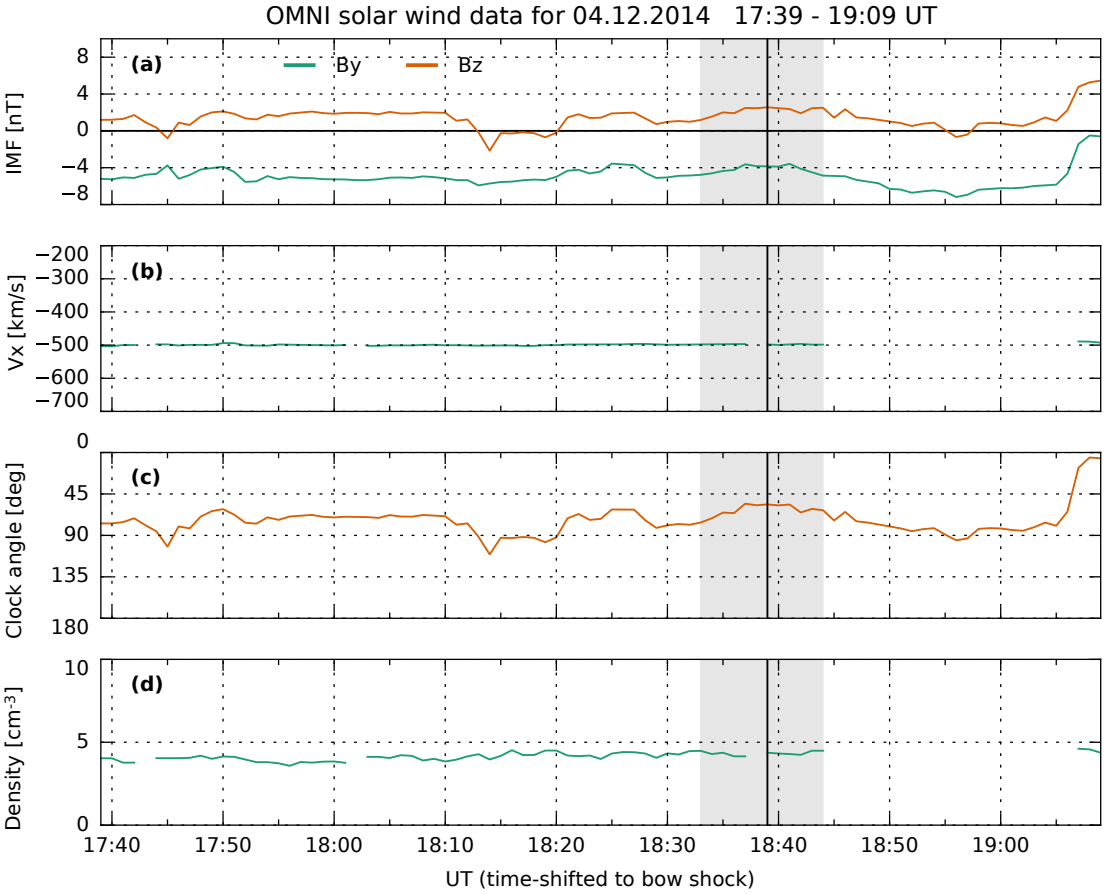

Figure 4.16: Solar wind conditions for RFE 42. Panel (a) shows the IMF B_y (green) and B_z (brown) components. Panel (b) shows the solar wind speed. Panel (c) shows the clock angle. Panel (d) shows the particle density in the incoming solar wind. All data are time shifted from L1 to the Earth's bow shock.

Figure 4.16 shows that the IMF conditions for RFE 42 is fairly stable with a weakly positive IMF B_z, and a strongly negative B_y. This is reflected in the clock angle between $45° - 90°$ indicating B_y dominated IMF. The solar wind speed V_x is almost constant at 500 km/s while the density is $\sim$4 cm^{-3}. RFE 42 starts to appear around 18:39 UT and displayed in Figure 4.17 panel (a) from 18:41 UT. At 18:46 UT it has moved westward and slightly poleward. Since this is close to the dayside inflow region, for negative B_y we expect flow away from the radar. However, around 8:30 MLT the flow is in a direction strongly against the inflow direction. At 18:48 UT we see that the RFE is expanding before it starts fading away at 18:49 UT, which is a frequently observed feature of RFEs. The original position of the RFE is outlined by the black contour in panels (c) and (d). The relative motion of the RFE is in the order of 200-300 km, and a duration of 11 minutes gives it a propagation speed of around 400 m/s. This is consistent with typical convection speeds in the polar ionosphere and of the same order of magnitude as the speed in the flow channel itself.

Due to the RFEs location between 08-09 MLT this is possibly too far towards the dawn side to represent an dayside RFE. It is at least outside the MLT range studies by

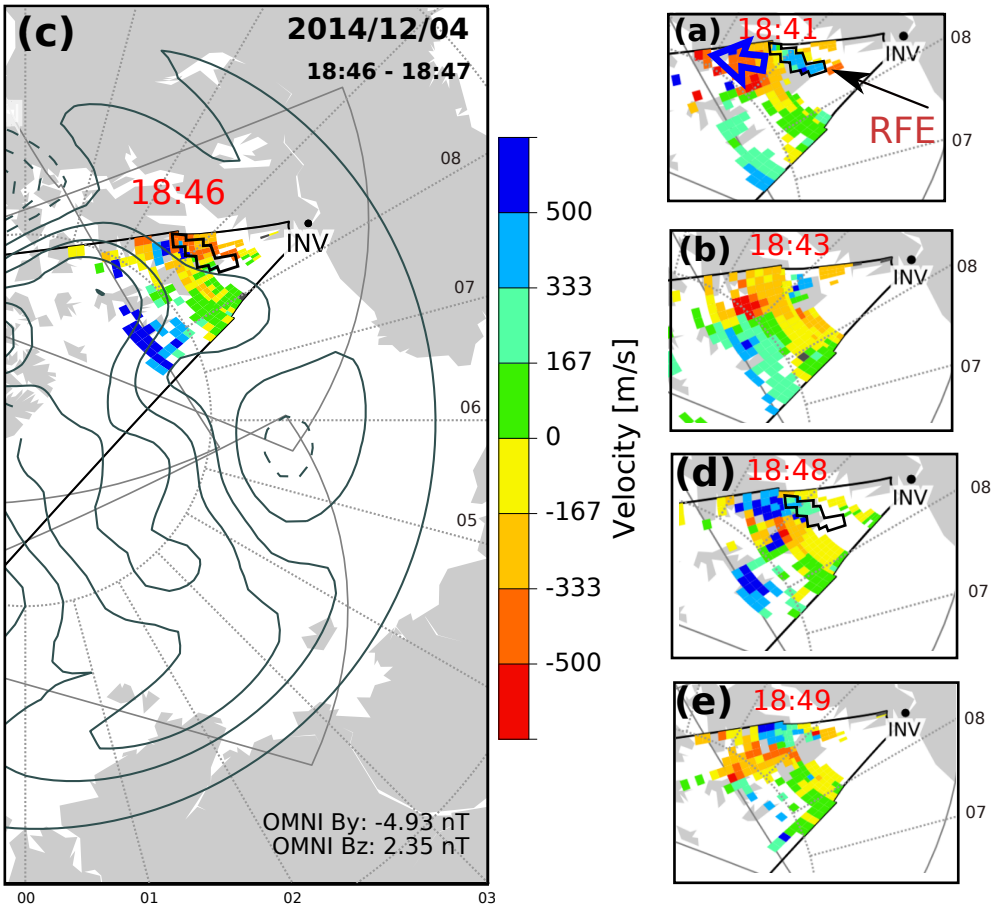

Figure 4.17: RFE 42 seen from the Inuvik (INV) SuperDARN radar between 18:39-18:49 UT, here seen from 18:41 UT. In panel (a) we see the development of the RFE around 09 MLT in the prenoon inflow region. Through panels (b) and (c) we see the RFE moving eastward towards the inflow region denoted by the large blue arrow in panel (a). Note that the flow inside the blue coloured RFE is westward the entire time. Blue denotes flow towards the radar and red away from it. The contour outline in panels (c) and (d) show the position of the RFE at 18:41 UT. In panel (e) at 18:49 UT the RFE starts fading away.

Rinne et al. [2007]. Slightly positive IMF also favours reconnection in the lobe cells. However, with limited data from other ground-based instruments and satellites, no final conclusions can be reached. The flow channel's location at 77° magnetic latitude (MLAT) also gives it the possibility to be located both inside and outside the polar cap.

4.2 Overview of results

The presented case studies are only a small portion of the dataset we have studied. In the following we will try to summarize our results by giving an overview of the time duration and IMF distribution of the analysed RFEs. It has to be emphasized that this study is rather limited with 57 RFEs analysed in total. Any statistical findings should therefore rather be seen as indications instead of solid conclusions.

4.2.1 Time duration

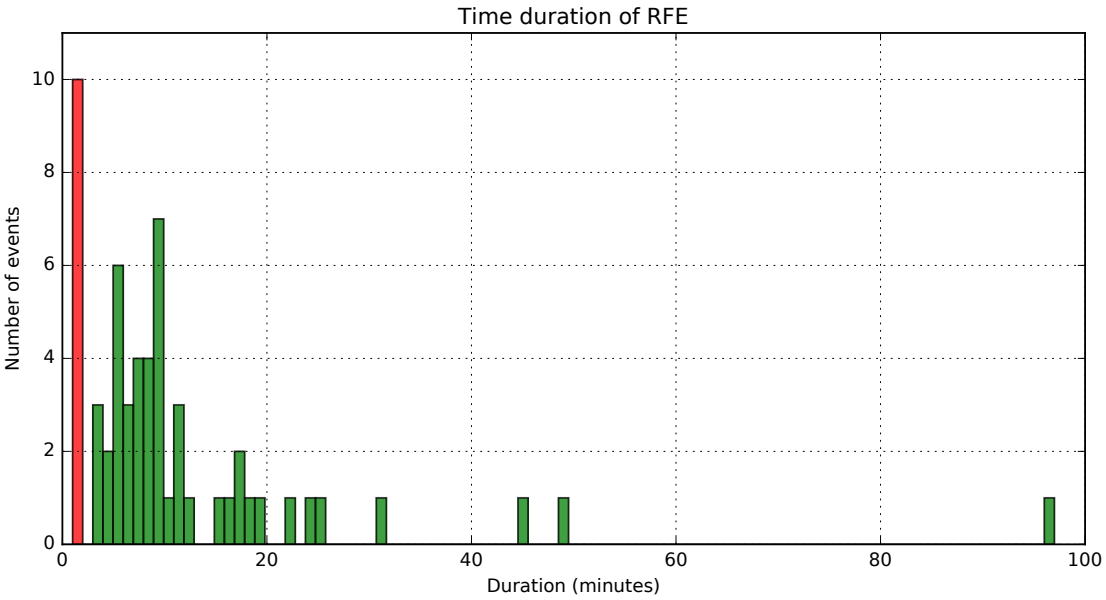

Figure 4.18: Overview of the time duration of the 57 RFEs that we identified in our analysis. We see that the vast majority of events lasted shorter than 20 minutes.

Figure 4.18 shows an overview of the time duration of all 57 reversed flow events that we have identified. The vast majority of the RFEs lasted less than 20 minutes. Marked in red are all events only seen in one radar scan, which amounts to 10 RFEs. The average duration of our events is 11.4 minutes. This is, however, affected by the inclusion of a few very long lasting events. The calculated median value is 8 minutes, which indicated the typical event duration. This is in contrast to the RFEs found by *Rinne et al.* [2007], which had a lifetime of $\sim$ 19 minutes in average.

4.2.2 IMF and MLT dependency

Figure 4.19 shows the polar distribution of magnetic latitude (MLAT) versus magnetic local time (MLT) for the observed Reversed Flow Events (RFEs). Local noon is up, with MLT time written around the polar plots. The plots are sorted by IMF components and coloured based on the sign of the average IMF values in a period of 15 minutes before each RFE event. This is to see whether the IMF polarity affects the distribution of RFEs versus local time. The interval of 15 minutes is chosen to take into account the propagation time from the bow shock to the ionosphere, as well as including more

measurements than just a snapshot. The size of the circles represents the absolute magnetic field strength, but not to scale.

Most RFEs are found on the dawn and dusk sides with 26 events in the 4-10 MLT dawn region (46%) and 14 in the 14-20 MLT dusk region (25 %). 12 RFEs are identified within the 10-14 MLT dayside region (21%) and only 5 in the 20-4 MLT nightside region from (9%). The dayside boundaries are chosen where the majority of the *Rinne et al.* [2007] RFEs are found. The dawn and dusk regions are located where the ionospheric response of lobe reconnection is thought to occur [*Imber et al.*, 2006]. The nightside region is covering the largest MLT span (8 hours) but account for the lowest number of RFEs with only 5. The polar plots in Figure 4.19 have boundaries for the polar cap regions marked.

As we see for IMF B_x in panel (a) and B_y in panel (b), there is a clear trend for the location of RFE depending on their magnetic field polarity. IMF B_x is usually positive when $B_y < 0$ and vice versa due to the Parker spiral geometry of the emitted solar wind.

Most RFEs with $B_y > 0$ in Figure 4.19b are found from slightly pre-noon (8 MLT) until 18 MLT, while RFEs with $B_y < 0$ are predominantly found on the nightside (20-7 MLT). For strong B_y this is not unexpected, since $B_y > 0$ will shift the dayside inflow region post-noon [*Cowley et al.*, 1991]. There is no significant spread in MLT based on IMF B_z shown in panel (b), but in our study 26 RFEs (45.6%) of the RFEs with stable B_z is observed during northward IMF, while only 6 RFEs (10.5%) were observed during southward IMF. The remaining either has poor data coverage or fluctuating IMF B_z prior to the RFE onset. This shows that for stable IMF conditions, RFEs are more likely to occur for northward IMF.

Figure 4.19d shows the RFEs with stable IMF sorted by clock angle. We see that all events with $\theta < 45^\circ$ and thereby IMF north dominated are located in the dawn and dusk regions. All RFEs with IMF due south ($\theta > 135^\circ$) can be seen on the dawn side.

Panel (e) shows the RFEs with stable B_y and B_z displayed as IMF strength versus MLT. Events with both B_y and B_z stable are thus displayed with two dots of red and blue. We see that at the dayside both B_y and B_z are positive for these events. For dawn/dusk events there is more spread but with predominantly positive IMF B_z. In the nightside region all events have strongly northward IMF as well as strongly negative IMF B_y. However it should be noted that these events are only a small subset of all the RFEs with stable IMF for 15 minutes prior to the events, so not all events are represented here.

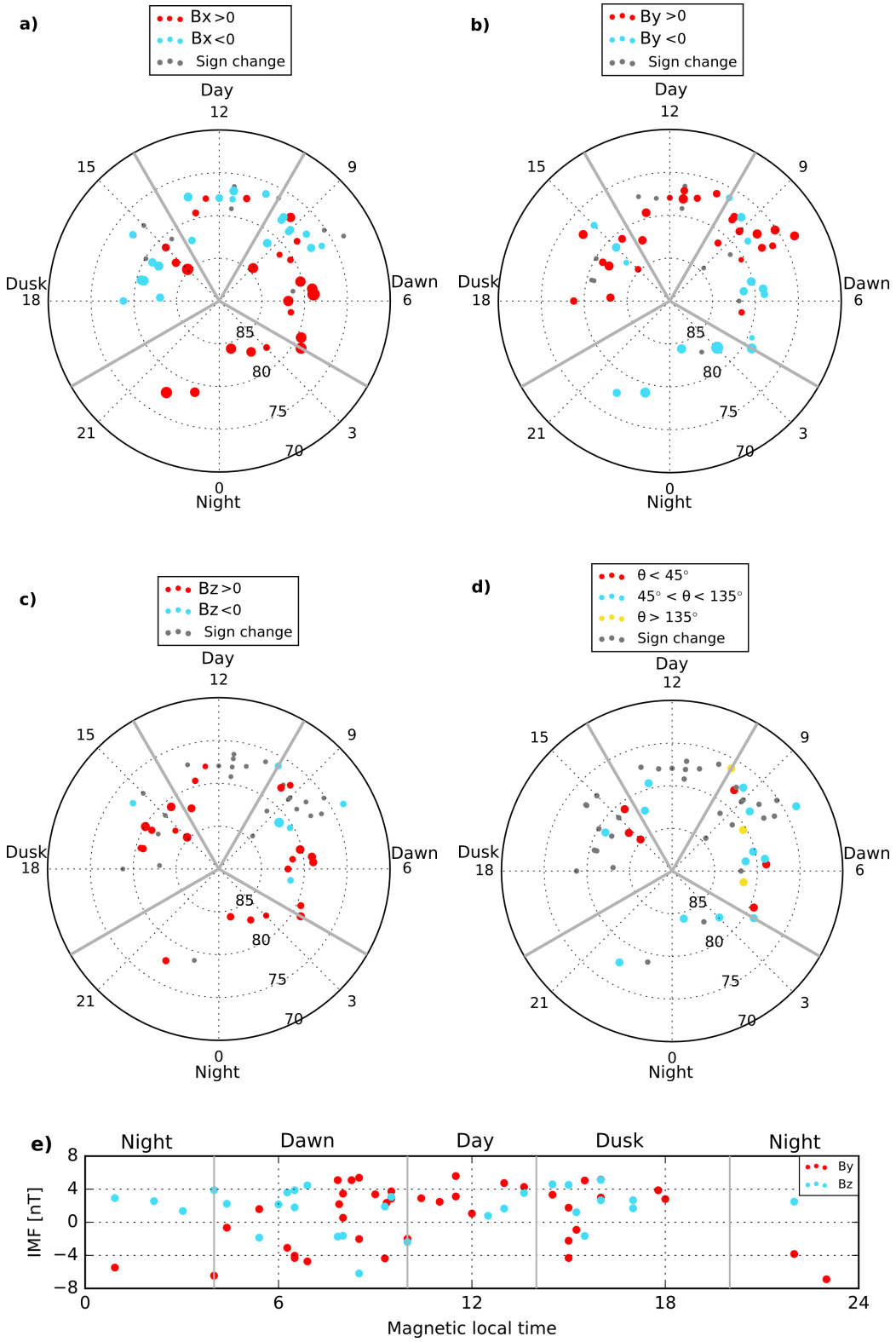

Figure 4.19: Panels a), b) and c) show the MLT distribution of IMF B_x, B_y, B_z respectively in a polar plot. The events are coloured with positive values red and negative blue. The magnetic pole represents the centre with magnetic noon up. Grey dots represent changing IMF sign. d) shows the clock angle sorted by due north (red), B_y dominated (blue) and due south (yellow). All polar plots have boundaries for polar cap regions marked. In panel (e) we see B_y and B_z sorted by their IMF strength versus MLT.

Chapter 5

Discussion

In this chapter we will discuss our results and present plausible explanations for the observations. Based on the observational features and source regions, we will attempt to categorize the reversed flow events. First we will discuss some biases in the radar data, and the validity of the spacecraft measurements.

5.1 Data validity

In order to make sure the results of our data is reliable we have taken a closer look at the fitting of individual range gates within the SuperDARN data. We will briefly assess how it is done, and the reliability of the velocity fittings. Afterwards we will highlight a few challenges with the SWARM field aligned currents, and how it affects our results.

Figure 5.1 takes a closer look at the FITEX results from the Inuvik (INV) SuperDARN beam 14 at 00:38:48 UT, which is the same beam and time as from RFE 2 in Figure 4.8. The figure shows power, velocity and the number of good lags for different range gates. The RFE is observed in range gate 22-26 and outlined in black. There is relatively strong backscatter power during the event, as well as 10-15 good lags which ensures smaller uncertainties when the velocity is determined. Figure 5.2 shows the fitted results of range gates 21, 22 and 24, which is just before the flow reversal, during, and after. From panel (a) we can observe that the velocity is calculated to -708 $\pm$ 12 m/s. From the model phase comparison we see that there is little fluctuation in the phases, which means there is little uncertainty in the data. There are, however, two secondary minima in the least square fit, marked 1) and 2) that are indicative of multiple velocity signals inside the volume of range gate 21. It could indicate turbulent convection near the RFE.

Figure 5.2b shows that the flow has changed direction to +84 $\pm$ 43 m/s. From the model phase comparison we see there are a lot more fluctuations in the phase error, which indicates that in this range gate there is not one decisive velocity, but rather a combination of multiple speeds superimposed. We can see that this is an increase in turbulence form panel (a). From a single range gate, the autocorrelation function can therefore give an indication of turbulent flows, possibly giving rise to the growth of plasma irregularities. In literature there are two fundamental mechanisms for producing F-region irregularities at high latitudes [*Carlson et al.*, 2007], the Kelvin-Helmholtz (KH) instability [*Basu et al.*, 1988], and the E×B Gradient Drift (GD) instability [*Tsunoda*, 1988].

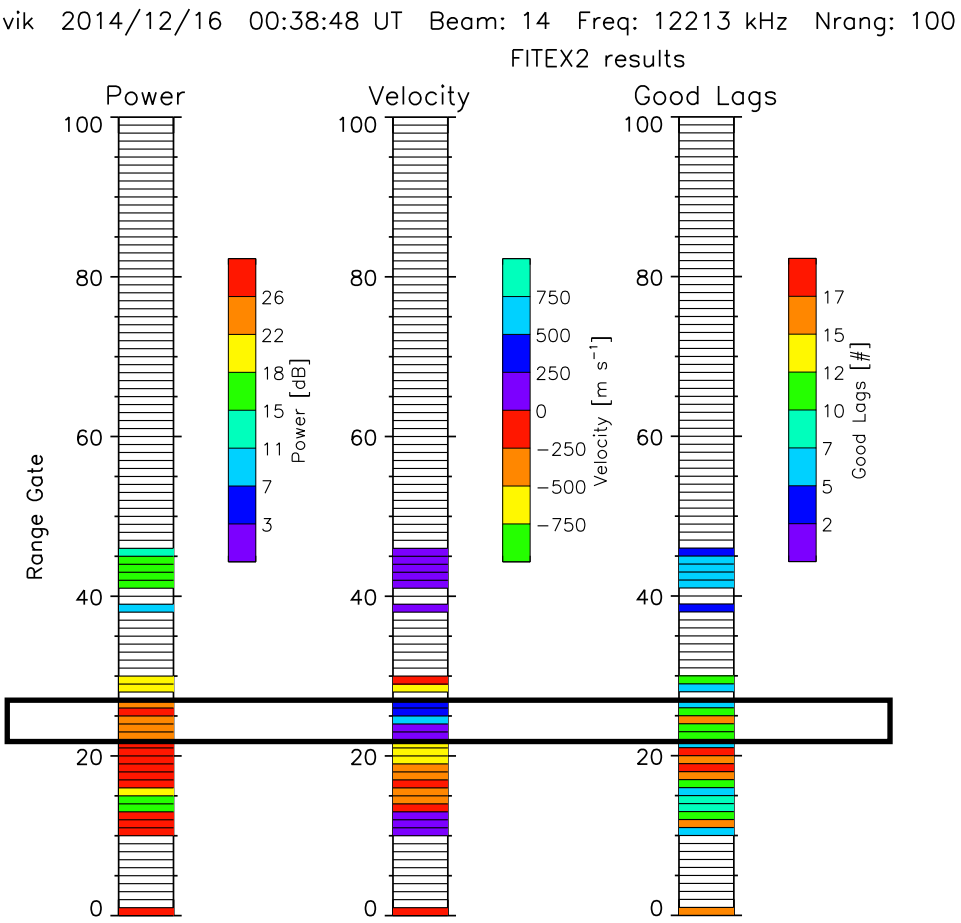

Figure 5.1: Overview of the number of good lags at each range gate for beam 14 of the INV radar on 16 December 2014 at 00:38:48 UT. The range gates containing the RFE 2 is highlighted with a black contour.

The KH instability is thought to occur when there are severe velocity shears transverse to the magnetic field. The GD instability is a cross-field instability happening when a charge separation takes place, and which is due to the induced electric field in the presence of a magnetic field increases the disturbance.

To our knowledge, this is the first time that someone has pointed out the structure of the flow within one single range gate of SuperDARN in connection with the edge of a RFE.

Figure 5.2c displays the subsequent range gate further inside the RFE, and the data shows that the flow turbulence is smaller. This can be seen by a velocity of 502 ± 36 m/s and a more stable model phase comparison. Overall we can conclude that the number of good lags is sufficient for determining an accurate flow velocity inside and outside the RFE.

Similar investigations have been made for other beams and RFEs reported in this thesis, in order to verify the data quality.

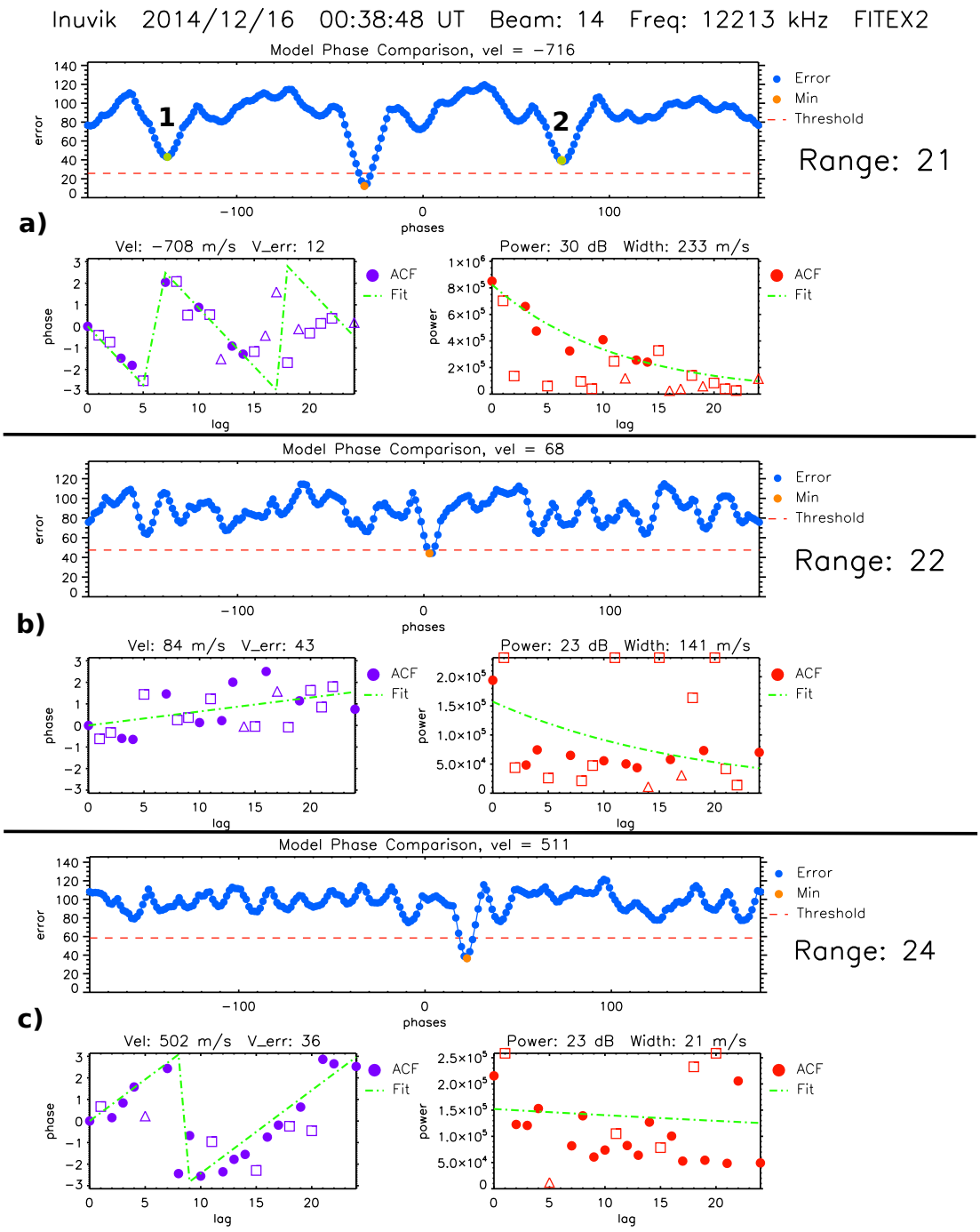

Figure 5.2: A look at the quality of the fit for range gates 21-24 in beam 14 of the INV radar on 16 December 2014 at 00:38:48 UT, which corresponds to RFE 2. For the velocity it is seen that the error is relatively small. [Panels generated with the ACF diagnostic tools from Virginia Tech's sites, `http://vt.superdarn.org/`]

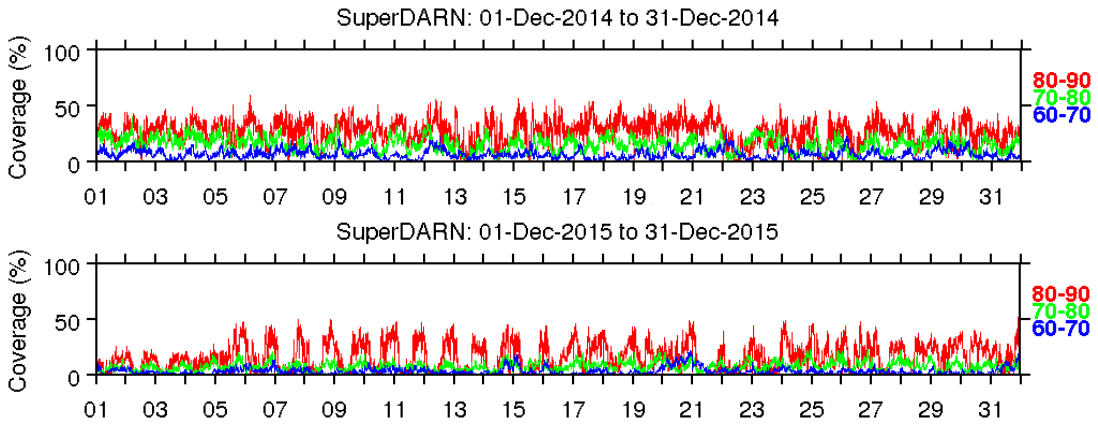

Figure 5.3: Relative SuperDARN coverage for different magnetic latitudes in December 2014 and December 2015, from which the majority of our data is collected. There is more coverage at midnight UT when the polar radars are close to noon MLT [statistics made by Kjellmar Oksavik].

5.1.1 Biases is SuperDARN data coverage

Figure 5.3 shows the relative coverage of all radars in the northern hemisphere sorted by magnetic latitude of 60-70°, 70-80° and 80-90°. Our events are all above 70°, and most above 80°, which corresponds to green and red color in the plot. There is generally more coverage in 2014, which is closer to solar maximum and resulting higher ionization in the ionosphere [*Balan et al.*, 1994]. This further results in better conditions for SuperDARN backscatter [*Imber et al.*, 2013]. In the 2015 panel we can see that there is a periodic oscillation of coverage following a 24 hour cycle. This is a result of the Canadian radars RKN, INV and CLY that are close to noon MLT at midnight UT when the coverage shows most activity. Higher backscatter at dayside than the nightside is a result of stronger ionizing particle precipitation and solar EUV radiation resulting in higher plasma density [*Milan et al.*, 1997].

The fact that most of our RFEs are observed in the dawn/dusk or dayside polar cap might be related to the fact that this is where there is best data coverage, but our data also indicates higher occurrence in the dayside when the data coverage is taken into account. For 2014 this was not a dominating factor, as most observed RFEs occurred in the dayside polar cap.

5.1.2 SWARM Field Aligned Currents

Due to SWARMs large orbital speed of ~ 7.6 m/s and sampling frequency of 1 Hz, the resolution of individual measurements will be ~ 10 km. Small scale currents extend up to 150 km and are commonly associated with kinetic Alfvén waves [*Stasiewicz et al.*, 2000], which give correlation up to 20 seconds. These are the features shown in Figure 4.5a and thought to originate from reconnection events at the dayside magnetopause, or in the magnetospheric lobes. It has to be noted that large-scale FACs are not visible on this scale due to fluctuations from the small scale current sheets. These large-scale currents can be seen in the combined dataset in the red line in Figure 4.10a which shows currents while the spacecraft passes equatorward of the RFE through the OCB. Efforts to filter out small scale current sheets has therefore been done to study the temporal and spatial variations of large scale FAC [*Lühr et al.*, 2015]. Studying time variation of

small scale current sheets is a new opportunity with SWARM due to the constellation of several spacecrafts.

There are, however, a few problems with the current density calculated from Ampere's law in equation (3.1). The magnetometer measures the complete geomagnetic field, so there are models applied to subtract the main field from the readings. The spacecraft only measures gradients of the magnetic field along the orbit, so cross-track gradients are assumed to be insignificant. As discussed in the theory, the calculation of current density assumes that field-aligned currents are perpendicular to the flight direction, which is only the case when the magnetic field lines are perpendicular too. This is only true at very high magnetic latitudes, which is not the case for the entire polar cap. As discussed by *Lühr et al.* [2015], small changes in the assumptions of the main magnetic field and the algorithm used for calculating the current density results in large variations of the final current density. A lot of caution should therefore be taken when interpreting the actual currents.

For the single satellite FAC shown in Figure 4.5 the actual value of the current is of less importance since we are not intending to make estimates of e.g. the ionospheric conductivity, but rather the existence of small scale current sheets during periods of ionospheric flow channels. Indeed our results confirm this finding with several upward and downward current filaments down to around to 5 seconds duration, resulting in $\sim$40 km spacial extent. There is no dominant direction of the current, with the current filaments alternating direction every 40 km equatorward of the flow channel. It should be noted that all these currents are on open field lines and not related to the large-scale Region-1 and 2 currents. To our knowledge this is the first time small-scale field aligned currents have been reported in relation to reversed flow channels in the polar ionosphere.

5.2 Algorithm challenges

The search algorithm only detects strong velocity shears, and principally does not distinguish between an RFE and for instance a flow reversal. As we know, an RFE needs at least two regions of strong shear flow, i.e. both clockwise and counter-clockwise flow reversals. The actual RFEs therefore have to be manually sorted to remove false hits by the algorithm.

As of now, only around one of every 50 scans flagged by the algorithm turns out to be actual RFE, which means that some manual work is still needed done to analyse a large dataset for occurrence of RFE. However, for this master thesis the goal has mainly been to extend the list of RFEs seen by SuperDARN. For future projects, it is therefore critical to advance the algorithm to obtain a higher success ratio for the detection of RFEs.

This problem is a good example where machine learning algorithms and image recognition can effectively be used to improve the search algorithm. However, that is far beyond the scope of this master project.

Another question is also whether the RFE definition set by *Rinne et al.* [2007] and stated in 2.6.1 is the best to detect transient reversed flows in the ionosphere. The criteria were mainly set based on the restrictions of the EISCAT radar used in their study. For the physical processes responsible, the specifications of the instruments is irrelevant. For instance, if RFEs are the observable return-flow of FTEs, what if many

return flows do not develop into fully reversed flows, but rather as a weakening in the large scale convection? By the RFE definition of minimum 250 m/s flow in opposite direction of the large-scale flow this weakening will not be detected as an RFE even if it has the same physical origin as fully developed RFEs.

Since RFEs only had been observed in one SuperDARN study [*Oksavik et al.*, 2011] prior to our work, we primarily focused on identifying strongly developed flow channels. For further studies however, care should be taken with setting too strict criteria, as many observable signatures otherwise might be discarded due to arbitrary limits.

5.3 Location dependent generation mechanism

As it is clear from the MLT distribution in Figure 4.19, reversed flows are not only limited to magnetic noon and the dayside inflow region. In contrast, all the events reported by *Rinne et al.* [2007] happened between 10:30 and 13:30 MLT. However, this is related to the fact that their scans were constrained between 09:00 and 14:30 MLT, with the majority of their scans occurring between 10:15 and 12:45 MLT.

In our study we placed no restrictions on MLT for the dataset we analysed, because SuperDARN radars operate 24 hours a day. From Figure 4.19 we see that most RFEs are detected at the dayside, but not all. There were also several nightside RFEs.

We have sorted our events depending on Magnetic Local Time (MLT), and sorted the RFEs in Table 5.1. We observe that there are 12 events in the dayside region, 5 in the nightside, and 40 in the dawn and dusk sides combined.

Both *Rinne et al.* [2007] and *Moen et al.* [2008] explain RFEs as a result of dayside reconnection in terms of Southwood FTEs or MI current systems. This might be the case for RFEs near the OCB in the dayside inflow region. However, it does not cover all RFEs that otherwise satisfy the RFE selection criteria of *Rinne et al.* [2007]. Therefore we will now discuss three main categories of RFEs and categorize them depending on their location and generation mechanisms:

Dayside RFE: This is the original observation of RFEs that was detected by *Rinne et al.* [2007], and further investigated by *Moen et al.* [2008] and *Oksavik et al.* [2011]. These RFEs are thought to occur near the dayside OCB as an ionospheric response to magnetic reconnection at the dayside magnetopause.

Lobe cell RFE: This is the most frequent observation in our SuperDARN dataset. Based on IMF conditions it is thought to originate from flow reversals set up by lobe cells during positive IMF B_z.

Table 5.1: Distribution on RFEs according to their location in the polar.

Region	MLT	Number of events	Average Duration (min)
Dawn	04-10	26	7.9
Dayside	10-14	12	10.1
Dusk	14-20	14	19.7
Nightside	20-04	5	9.2

Nightside RFE: This is one of the least understood types of RFE like flows and is most likely set up by bursty bulk flows [*Angelopoulos et al.*, 1992] in association with nightside reconnection.

5.3.1 Dayside RFE

This is the best documented type of RFE. Originally only seen by the EISCAT Svalbard Radar by *Rinne et al.* [2007], *Oksavik et al.* [2011] observed the first RFE with the SuperDARN Hankalasmi (HAN) radar. Dayside RFEs have been thought to originate from magnetic reconnection on the dayside magnetopause. It has however been a problem to identify which mechanisms are responsible for generation. For a long time it was thought to be related to flux transfer events through the Southwood FTE model [*Southwood*, 1987], but there has been a constant issue that the observed RFEs only contain one return flow channel. According to the Southwood model there should be a strong centre flux with two return flows on either side for each FTE event. Furthermore, RFEs cannot represent the centre flux, since the flow direction is opposite to the magnetic tension force. *Rinne et al.* [2007] therefore presented a modified version of the Southwood FTE model which only contains the poleward side of the return flow. This was an effort to explain why only one reversed flow is observed.

Moen et al. [2008] took a step back from the Southwood FTE explanation, and described RFEs as a result of two consecutive FTEs connecting through a poorly conducting ionosphere. These FTEs are independent and map to different reconnection sites in the magnetosphere. Two independent magnetosphere-ionosphere current loops will therefore be set up giving rise to the large electric field resulting in a RFE.

Alternatively *Moen et al.* [2008] suggested that RFEs might be the ionospheric footprint of an inverted V-type coupling region because of the quasi-stationary and bipolar form of the RFEs observed in their study. Inverted Vs are events related to accelerated trapped electrons observed on the equatorward side of the dayside OCB. *Moen et al.* [2012] observed a close relationship between PMAFs and FTEs, as well as inverted Vs and FTEs. Their studies conclude that both RFEs and PMAFs therefore are ionospheric signatures of an inverted V- type coupling region.

Our study indicate that these explanations by *Moen et al.* [2008] might not be the case for all observed dayside RFEs. As shown in Section 4.1.4, we have observed at least one case of a dual RFE existing in the dayside polar cap near the open closed boundary. As Figure 4.15 reveals, both the centre flux and the reversed flows develop together and thus should be treated as signatures of one event. The simultaneous growth and decay makes it evident that these structures must result from the same event. However, due to the positive IMF B_z for this event, it also makes an FTE explanation questionable. A recent study by *Wang et al.* [2006], which observed 3 years FTEs from Cluster data emphasizes that a large portion of the FTEs can also occur for northward IMF. Accordingly the FTE explanation cannot be excluded for northward IMF.

It might be the case that the equatorward return flow is sometimes underdeveloped as explained by *Rinne et al.* [2007], but the lack of two return flows may also be a result of the relatively limited field of view of the EISCAT Svalbard Radar, and thus imposing limitations of seeing the larger picture. In addition, EISCAT radars only operate on a campaign basis. With the SuperDARN radars we have studied RFEs over thousands of kilometres, with larger temporal resolution and continuous coverage. In this way

we have more opportunities to see the ionospheric response resulting in reversed flow channels. The disadvantage is that SuperDARN has lower spatial resolution, so we cannot see the smallest RFEs with SuperDARN.

Our SuperDARN data shows 12 RFEs happening in the dayside polar cap inflow region. Due to limited conjugate satellite passes and ground observations our data does not make any final conclusions on the generation mechanism, but the observation of simultaneous RFEs close to the inflow region still makes the Southwood FTE mechanism relevant.

5.3.2 Lobe cell RFE

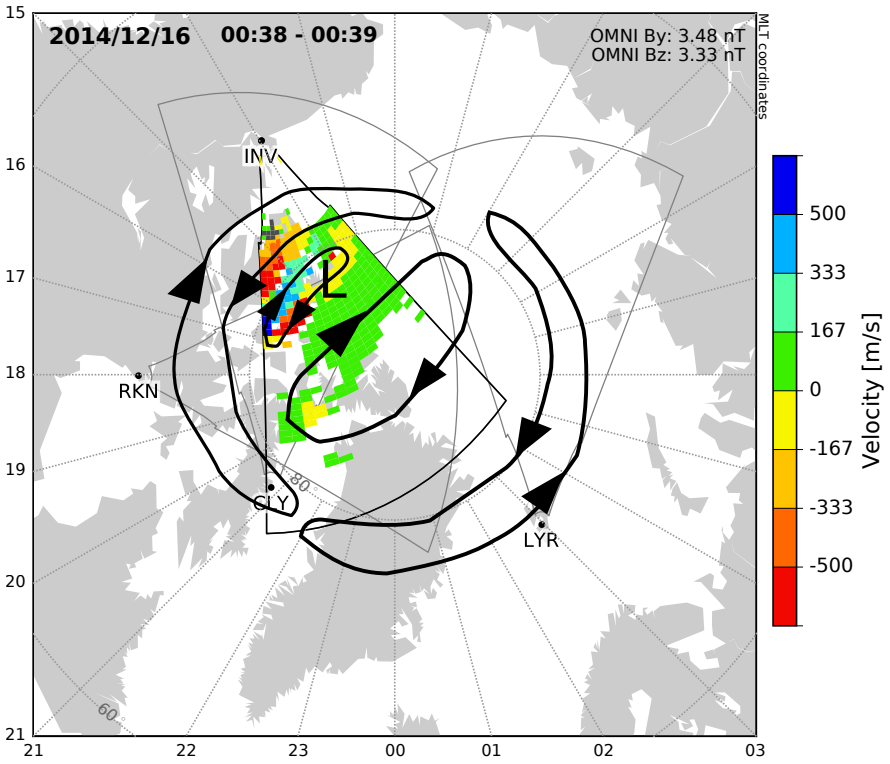

Figure 5.4: A sketch of the convection pattern for northward IMF B_y and B_z after *Reiff and Burch* [1985] overlaid on top of the line of sight velocity data from the INV SupperDARN radar. The lobe cell is marked with an 'L'.

40 of our RFEs are determined to originate from the dawn/dusk section. Due to their far distance from the cusp inflow region, an FTE explanation seems less likely. Of course these are not strict locations, and the inflow region can be shifted due to IMF B_y, so in boundary regions between dayside and dawn/dusk there could potentially be other mechanisms responsible for the observed reversed flows.

As presented in Chapter 4.1.2, the RFEs observed in the dawn and dusk section are thought to originate from lobe reconnection giving rise to lobe convection cells in the polar ionosphere [*Reiff and Burch*, 1985]. Based on the continuous northward IMF prior to most of our observed events, this makes the lobe cell explanation preferable.

When evaluating ionospheric signatures of lobe cell reconnection for northward IMF, we have to separate between single and dual lobe cell reconnection [*Imber et al.*, 2006].

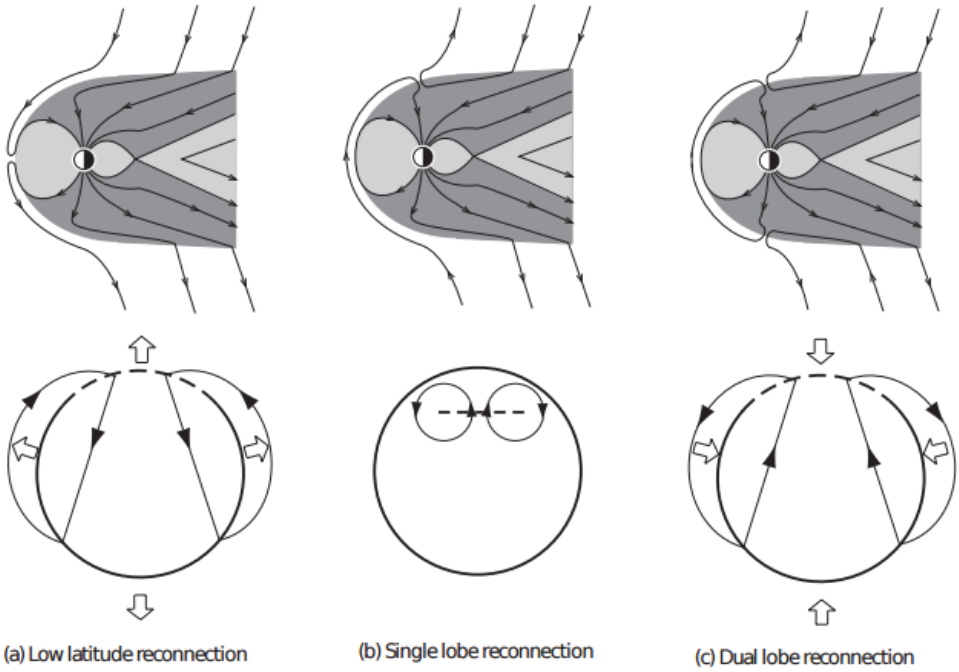

Figure 5.5: Schematic representation of reconnection for different values of IMF. (a) shows low-latitude dayside magnetopause reconnection for southward IMF, which is the one giving two cell convection. (b) shows single lobe cell reconnection for northward IMF with IMF $By \neq 0$. This gives independent reconnection in the hemispheres and no change of OCB. (c) shows dual lobe reconnection for northward IMF with $B_y \approx 0$. This results in two lobe cells and contraction of the polar cap due to closing of open field lines. In the convection patterns the solid circle is the OCB and solid arrows are flow streamlines [from *Imber et al.*, 2006].

For IMF B_y values either strongly positive or negative we get independent reconnection in the northern and southern hemispheres, and the reconnection will not produce any closed field lines. The location of the OCB and the size of the polar cap will therefore be unchanged, and the open shear flux in the polar cap is said to be stirred [*Crooker*, 1992]. An illustration of this scenario is shown in Figure 5.5b.

For IMF B_y close to zero during northward IMF is we get dual lobe reconnection, caused by simultaneous reconnection in both hemispheres and closing of open field lines in the polar cap [*Imber et al.*, 2006; *Milan et al.*, 2000]. This happens because there will be simultaneous but independent reconnected field lines in the two hemispheres for IMF $By \neq 0$. For IMF B_y close to zero the two reconnection sites will be on the same interplanetary magnetic field line in a way such that this will be closed, see Figure 5.5c. For this dual lobe reconnection there will be sunward flow across the OCB and the polar cap will contract due to a loss of open magnetic flux.

Hot Flow Anomaly

We have also searched for reversed flows in relation to Hot Flow Anomalies (HFA) in the solar wind. HFAs are temporary reversals of the solar wind that move past the Earth and result in strong density variations, plasma heating, and flow deflection [*Schwartz et al.*, 1985; *Thomsen et al.*, 1986]. The transient magnetopause deformation caused by the HFA gives ionospheric responses in the form of convection vortices that

move from the dayside to the nightside [*Sibeck et al.*, 2003]. During a HFA observed by the THEMIS spacecrafts, *Jacobsen et al.* [2009] observed ionospheric flow opposite to the large-scale convection.

The reversed flow seen by *Jacobsen et al.* [2009] due to HFA was observed in the prenoon MLT sector and could be a possible generation mechanism for our dawn/dusk RFEs. Unfortunately, the OMNI data did not reveal any strong pressure gradients for our events. However, the SuperDARN coverage has improved substantially since the study by *Jacobsen et al.* [2009], and it may be possible to observe signatures in the ionosphere of separate HFAs in the future.

5.3.3 Nightside RFE

Nightside RFEs have in common with the lobe cell RFEs that the reversed flow channels are observed in the sunward direction. However, they are distinguished by their location, which around midnight MLT makes the lobe reconnection explanation unlikely. Strong sunward flow is often seen in relation to Bursty Bulk Flows (BBFs) [*Angelopoulos et al.*, 1992]. These flows are thought to originate from nightside reconnection [*Nagai et al.*, 1998], but the full details are still unknown. BBFs are most often observed during the growth and expansion phase of auroral substorms for southward IMF [*Sergeev et al.*, 1996]. However, one of the issues with a substorm explanation of BBFs is that they are also observed during quiet conditions, as investigated by *Zhang et al.* [2016]. For these events IMF is predominantly northward.

Senior et al. [2002] observed westward flow bursts by SuperDARN just south of auroral streamers observed in relation to BBFs for northward quiet IMF conditions. The auroral streamers are attributed to earthward injection of high velocity plasma from the near-earth plasma sheet.

Recent studies by *Lyons et al.* [2011] shows that narrow flow bursts from far within the polar cap directed equatorward towards the nightside polar cap boundary can trigger BBFs in the plasma sheet which then leads to auroral poleward boundary intensification (PBIs) and streamers. Hence it is a rather open question what triggers the bursty bulk flows in the plasma sheet, and whether they are caused by ionospheric flow channels, or if the flow channels are caused by BBFs [*Pitkänen et al.*, 2013].

4 out of 5 of our nightside observations of reversed flow channels occur during prolonged period of northward IMF. Additionally, 4 of them occur during negative IMF B_y conditions. Based on the results of *Zhang et al.* [2016] it is therefore no reason to believe that the observed nightside RFEs are related to substorm onset, since BBFs during northward IMF are not closely related substorms. Further investigations with magnetospheric observations will be needed to determine the exact cause and effects.

Transpolar arcs

As described in 2.5.6, TPAs are observed to occur simultaneously with azimuthal flow towards magnetic midnight [*Fear and Milan*, 2012b] for northward IMF. This east-west elongated flow is reversed in terms of the return flow seen for symmetric tail reconnection at midnight MLT. As most of our RFEs are observed during northward IMF, some of the them could potentially be related to TPAs and twisted tail reconnection. This would primarily apply to events observed near the nightside auroral oval on closed field

lines. These events should consequentially also be observable together with the actual transpolar arc.

Of our 5 observed nightside RFEs only one was observed during an optical satellite pass by the DMSP spacecraft, RFE 40 presented in 5.3.3. This enhanced flow is however sunward far into the polar cap, not longitudinally towards midnight MLT. The UV auroral oval seen ∼10 minutes after the RFE ends also does not show any signs of a TPA in this case.

Without having systematically searched for reversed flows in relation to TPAs our study has not excluded them either. By examining the other 4 nightside RFEs, they all appear to be north-south aligned far into the polar cap. This favours a BBF explanation as described above, but it does not mean that the TPAs cannot be responsible for RFEs. One reason why we didn't see any TPAs in our study might be related to the fact that the three polar radar mainly used, RKN, CLY and INV are looking far into the polar cap, and have no or little coverage directly at the equatorward side of the nightside OCB where the flows are expected. By including more lower latitude SuperDARN radars, it is possible that this category might be more frequently observed.

Chapter 6

Summary and Conclusion

This chapter concludes our study into the phenomena of Reversed Flow Events (RFEs) in the polar cap ionosphere. We have performed an comprehensive multi-instrument study comparing ground based radar measurements (SuperDARN) with satellite based magnetic (SWARM), particle (NOAA and MetOp) and optical (DMSP) instruments. Overall RFEs seem to be a frequent phenomena happening during all local times. We have shown that there are most likely several different generation mechanisms that can result in the same signatures in the ionosphere.

RFE occurrence

By using our custom made search algorithm a total of 57 previously unidentified RFEs were found in data from the high latitude SuperDARN radars from primarily December of 2014-2016. We found a distribution of RFEs lasting up to 97 minutes, with an average duration of 11.4 minutes. Most RFEs were found in the dawn and dusk regions with 26 events in the 04-10 MLT dawn region (46%) and 14 in the 14-20 MLT dusk region (25%). 12 RFEs were identified within the 10-14 MLT dayside region (21%) and only 5 RFEs in the 20-04 MLT nightside region (9%).

Our data shows no limitations within the northern hemisphere polar cap regarding where reversed flows are observed. The observational occurrence rate is rather determined by the radar's viewing direction and ionospheric conditions for radio wave propagation.

Local time and IMF dependency of RFEs

The observations of RFEs are strongly dependent on the IMF conditions and local time. Most nightside RFEs occur during both negative IMF B_y and B_z. There was no significant spread in MLT based on IMF B_z, but in our study 79% of the RFEs with stable IMF prior to onset were observed during positive IMF B_z. For B_y there was a strong preference towards dawn and night for negative values, and day and dusk for positive values.

Depending on their location we have classified the reversed flow channels as either dayside RFEs, lobe cell RFEs, or nightside RFEs. RFEs previously reported by *Rinne et al.* [2007] are all in the first category, but with our search algorithm we have also been able to observe reversed flows at all local times, hence the two new categories.

The IMF conditions show correlation with this categorization, as mostly northward IMF is observed for the lobe cell RFEs.

In this study we have seen the first clear example of current sheets on the equatorward side of the RFE. This agrees with the predictions of *Moen et al.* [2008] that there should be upward Region-1 FAC on the equatorward side of the RFE. However the current density data from the SWARM spacecrafts show that the currents are not uniform in one direction, but that several smaller both upward and downward current sheets exists.

Most RFEs appeared stationary, while at least one event (RFE 42), was seen moving poleward. This is contrary to the study by *Rinne et al.* [2007], which in 30% of their RFEs observed poleward latitudinal movement.

SuperDARN data validity

Some RFEs have been simultaneously observed with multiple radars, and are found to overlap. This is convincing and shows good accuracy in the SuperDARN range determination. In our assessment of the SuperDARN data validity we were able to see the existence of several velocities superimposed inside a single range gate scatter volume. This is a strong indication of smaller flow features within the usual 45 km range gate resolution. To our knowledge, this is the first time SuperDARN has been used to reveal spatial features of smaller scale sizes than the length of an range gate.

RFE generation mechanisms

Our results show indications of several different generation mechanisms of RFEs dependent on observation region and IMF conditions. Dayside and nightside RFEs are most likely responses to transient reconnection in their respective regions.

The dayside RFEs observed near the dayside inflow region have both fluctuating IMF B_y and B_z, giving rise to shifting reconnection sites necessary for the Southwood FTE and MI-current loop explanations presented by *Rinne et al.* [2007] and *Moen et al.* [2008] to occur. Our results are therefore in agreement with their findings.

Nightside RFEs are much less frequently observed. However, the ionosphere in northern hemisphere during winter time has generally less backscatter in the night [*Milan et al.*, 1997], so this might rather be a problem with less favourable SuperDARN observation conditions during night time. In literature, nightside flow transients have frequently been observed in relation to Bursty Bulk Flows (BBFs) [*Senior et al.*, 2002], and Transpolar Arcs (TPAs) [*Fear and Milan*, 2012a]. However, due to all of our nightside RFEs being north-south aligned, this makes the BBF explanation more likely.

Dawn and dusk RFEs are attributed to be a consequence of lobe reconnection for northward IMF. Depending on IMF B_y strength this can happen on both open and closed field lines [*Imber et al.*, 2006]. This is confirmed in our results with optical and particle measurements, but the resolution of the data are often insufficient to explicitly determine the location of the OCB. This will require further investigations with higher spatial resolution.

Chapter 7

Future Work

The work of this thesis covered a limited number of days analysed by the SuperDARN radars close to winter solecistic. With a larger dataset and multi-instrument observations a statistical study over several years, and at different seasons can be carried out. The available SuperDARN datasets from the last two decades opens up the possibility for large statistical studies of occurrence and distribution of RFEs.

With small modifications the developed search algorithm for RFEs can also be used to detect enhanced flow channels and other specific features in the SuperDARN line of sight data. We have only applied the algorithm on data from the polar cap radars in the northern hemisphere, but it can similarly be used for the mid-latitude and southern hemisphere radars. However this was out of reach for this master thesis.

The upcoming EISCAT_3D incoherent scatter radar [*McCrea et al.*, 2015] is also a new possibility to investigate reversed flow channels and instabilities with far better resolution. Since this is a phased array radar, it enables the possibility to study the movement of RFEs with higher both spatial and temporal resolution.

Assessing the relationship between RFEs, PMAFs, ion-upflow, and inverted-Vs is also something that we did not study too deeply, but that is of crucial importance for understanding the generation of RFEs and the magnetosphere-ionosphere coupling [*Moen et al.*, 2012]. This is important because these features serve as observable proxies for determining the location of magnetic reconnection, the direction of current systems, and regions of particle precipitation. More ground and rocket based measurements in co-existence with RFEs would therefore provide valuable insight to reveal these relationships. It would also be interesting to study if RFEs exists in the daylit summertime to check for ionospheric summer-winter asymmetries as suggested by *Moen et al.* [2008] and *Koustov et al.* [2017].

Some of the remaining unsolved scientific questions related to RFEs are listed below:

- Is there a seasonal variability in the occurrence of RFEs?
- Can RFEs be observed in conjugate hemispheres simultaneously?
- What role does RFEs play for the generation of plasma irregularities that affects human communication and navigation?
- Can underdeveloped RFEs possibly be more frequent and observable than the actual RFEs?

Appendix A

Coordinate systems

Two coordinate systems have been used in this thesis, and here we give an overview.

A.1 Geocentric Solar Magnetospheric (GSM)

For solar wind data we use the Geocentric Solar Magnetospheric (GSM) coordinate system, which has its X axis pointing towards the Sun, and the Z axis being the projection of the Earth magnetic dipole axis (positive North) perpendicular to the X axis [*Russell*, 1971]. The Y coordinate is orthogonal to both X and Z. When the solar wind hits the Earth's magnetosphere, it is aligned with the Earth's dipole axis, which makes this a good coordinate system for investigating the solar wind's interaction with the Earth.

A.2 AACGM

A mathematical model of the Earth's magnetic field, there is the International Geomagnetic Reference Field (IGRF) published every fifth year since 1965 [*Zmuda*, 1971], with the last being the 12th revision released in 2015 [*Thébault et al.*, 2015]. This model represents the Earth's magnetic field in terms of spherical harmonics based on ground and space-based observations. The spherical harmonic coefficients are updated every five years to take into account that the Earth's magnetic field is changing over time.

The Corrected Geomagnetic Coordinates (CGM) system is one system often used, which are tracing along the magnetic field lines of the IGRF model. For our purpose, we use a special version of the CGM system called Altitude Adjusted Corrected Geogmagnetic Coordinates (AACGM), originally defined by *Baker and Wing* [1989] and later updated by *Shepherd* [2014], which ensures that different points along the same magnetic field line will have the same coordinate. This is practical for mapping events in the ionosphere to a common grid.

Most data in this thesis will use Magnetic Local Time (MLT). Here the longitude is oriented such that magnetic noon (MLT=12hr) is the meridian pointing towards the Sun. The MLT coordinates are fixed in the Sun-Earth system, while the Earth is rotating. The magnetic latitude (MLAT) is the same as for the AACGM, system where 90° N will be at the magnetic pole in the northern hemisphere.

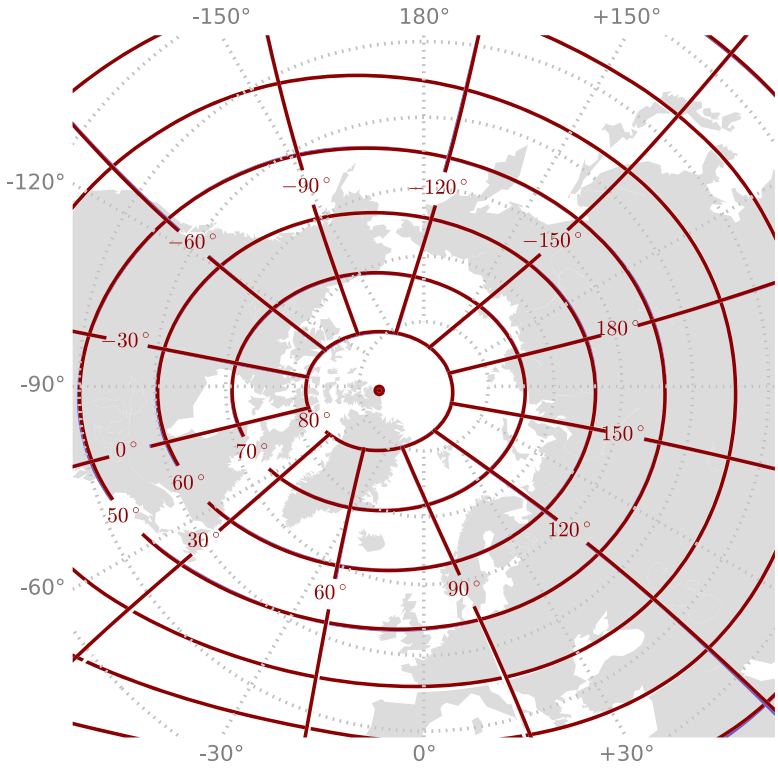

Figure A.1: AACGM coordinates plotted over the northern hemisphere in red color with geographical coordinates in grey background [from *Laundal and Richmond*, 2016].

Appendix B

List of RFEs

The following list gives extended details about all the Reversed Flow Events (RFEs) found during our study. The events are numbered after when they were detected, so they are not necessarily in chronological order. Date and start time in UT for all the events are given. Then follows the duration as well as gate and beam for which the event was observed. The magnetic local time and magnetic latitude for each event as used in the summary plots is also showed following the average IMF B_y and B_z in a time span of 15 minutes prior to the detection of each event.

Some events were located manually when looking through scans of other events, and do not always have all details calculated. 'A' in IMF values means 'Alternating' and denotes those events where IMF changes sign during the 15 minute averaging period.

Table B.1: List of all RFEs found in this study

Nr.	**Radar**	**Start Date** [yyyy/mm/dd]	**Start UT** [hh:mm]	**Dur.** [min]	**Beam**	**Gate**	**MLT**	**MLAT**	**IMF** B_y [nT]	**IMF** B_z [nT]
1	cly	2014/12/20	23:40	7	11	13	17.8	83.1	3.87	A
2	inv	2014/12/16	00:14	49	11	22	16.0	81.0	2.99	2.65
3	inv	2014/12/16	21:16	5	8	9	11.5	77.0	3.11	A
4	rkn	2015/12/10	18:39	1	14	14	13.1	77.3	A	A
5	rkn	2015/12/11	13:53	9	11	4	8.3	75.2	5.09	A
6	rkn	2015/12/12	13:36	1	9	7	7.9	76.4	2.19	A
7	rkn	2015/12/12	17:32	1	10	14	12.0	78.0	1.05	A
8	rkn	2015/12/13	14:55	4	6	13	9.0	78.2	A	A
9	inv	2015/12/09	23:01	17	9	24	13.6	82.2	4.27	3.54
10	inv	2014/12/15	00:37	12	14	31	16.0	81.8	5.16	A
11	inv	2014/12/18	21:33	45	10	8	11.5	76.5		
12	inv	2014/12/20	19:31	6	4	14	9.5	78.1	2.86	3.07
13	rkn	2014/12/15	00:19	24	4	22	17.0	80.9	A	2.66
14	inv	2014/12/01	16:07	15			6.5	80		
15	rkn	2014/12/15	01:07	5	5	16	18.0	78.8	2.8	A
16	rkn	2014/12/17	14:57	9	10	11	9.5	77.6	3.74	A
17	rkn	2014/12/17	16:00	1	14	8	10.4	76.3	2.9	A
18	rkn	2014/12/18	14:05	1	7	9	8.5	77.2	5.38	A
19	rkn	2014/12/20	17:11	18	8	12	11.5	78.0	5.58	A

Nr.	Radar	Start Date [yyyy/mm/dd]	Start UT [hh:mm]	Dur. [min]	Beam	Gate	MLT	MLAT	IMF B_y [nT]	IMF B_z [nT]
20	cly	2014/12/03	11:12	31			4.5	84.0		
21	cly	2014/12/03	10:46	4	7	20	6.0	81.9	A	2.15
22	cly	2014/12/03	21:32	9	14	18	15.0	84.8	1.76	4.52
23	cly	2014/12/04	07:43	3	12	21	0.9	84.3	-5.48	2.92
24	cly	2014/12/04	10:31	10	1	18	4.4	79.5	-0.65	2.23
25	cly	2014/12/06	10:08	5			3.5	84.0		
26	cly	2014/12/08	22:01	5	10	18	15.2	83.2	-0.91	1.21
27	cly	2014/12/11	21:49	8	6	8	15.0	81.2	-4.32	A
28	cly	2014/12/13	00:18	97	4	20	17.0	80.6	A	1.68
29	cly	2014/12/14	14:04	9	5	10	8.5	81.1	A	-6.19
30	cly	2014/12/14	14:58	1	5	13	9.4	81.2	2.34	A
31	cly	2014/12/17	21:04	16	4	11	14.5	80.9	3.33	4.59
32	cly	2014/12/19	23:19	19	2	15	16.0	80.1	A	5.11
33	han	2014/12/14	05:56	3	4	36	7.8	73.6	5.09	-1.7
34	inv	2014/12/01	11:42	9	9	24	3.0	82.2	-10.9	1.36
35	inv	2014/12/01	12:18	6	13	18	4.0	79.0	-6.46	3.88
36	inv	2014/12/01	15:35	25	9	16	6.3	78.9	-3.09	3.6
37	inv	2014/12/03	11:19	5	7	25	2.1	83.0	A	2.55
38	inv	2014/12/03	15:27	8	8	16	6.5	79.0	-4.32	3.87
39	inv	2014/12/03	15:46	5	11	20	6.9	80.2	-4.73	4.45
40	inv	2014/12/04	07:10	22	1	14	22.0	77.6	-3.84	2.49
41	inv	2014/12/04	07:56	7	13	18	23.0	79.0	-6.9	A
42	inv	2014/12/04	18:39	11	13	11	9.3	77.2	-4.37	1.9
43	inv	2014/12/08	14:00	11	11	38	8.9	84.5	A	A
44	rkn	2014/12/10	11:00	9	8	23	5.4	81.5	1.59	-1.86
45	rkn	2014/12/11	10:19	1	11	24	6.5	81.3	-4.05	1.8
46	lyr	2016/12/01	07:46	7	7	14	13.0	79.3	4.74	1.66
47	lyr	2016/12/04	01:44	1	6	22	8.0	80.4	0.54	-1.62
48	lyr	2016/12/04	11:06	9	10	5	15.5	77.4	A	-1.65
49	lyr	2016/12/16	10:27	8	11	7	15.0	77.5	-2.24	A
50	lyr	2016/12/17	03:24	11	10	19	8.5	78.5	-2.03	0.42
51	lyr	2016/12/17	07:19	7	6	10	11.5	79.1	A	A
52	lyr	2016/12/17	08:57	17	9	7	12.5	77.9	A	0.78
53	lyr	2016/12/20	10:58	8	13	9	15.5	77.3	5.05	A
54	lyr	2016/12/22	04:16	6	12	10	8.0	77.6	3.46	A
55	lyr	2016/12/24	06:25	1	11	0	10.0	76.1	-2	-2.39
56	lyr	2016/12/25	04:42	3	7	8	9.0	78.5	3.37	A
57	lyr	2016/12/29	06:13	1	12	15	11.0	77.6	-2.47	A

Appendix C

Search algorithm

```
def rfeFinder(velMatrix):
    """
    A function to locate RFEs in an entire scan of SuperDARN LOS data

    Parameters:
    VelMatrix (Array):
        Matrix with dimensions of gates x beams

    Returns:
    n,i (int):
        Index of location of sucessful located RFE
    None, None:
        Returns None if there is no RFE in the current scan


    Written by Kristian Reed 2017

    """

    [cols,rows]=shape(velMatrix)

    #Loop through beams
    for i in range(1,rows-1):

        #Loop through gates
        for n in range(cols-3):

            #Check for speed greater than 250 m/s in each direction
            if (velMatrix[n+2,i]>250 and velMatrix[n,i]<-250) or \
               (velMatrix[n+2,i]<-250 and velMatrix[n,i]>250):

                #Check for min 2 gate rfe
                if (abs(velMatrix[n,i]-velMatrix[n+1,i])<200):

                    #Check for strong gradient drift
                    if (abs(velMatrix[n,i]-velMatrix[n+3,i])>500):

                        #Check neighbour beam for same flow speed
                        if  (abs(velMatrix[n,i]-velMatrix[n,i+1])<200 or \
                            abs(velMatrix[n,i]-velMatrix[n+1,i+1])<200) and \
                            (abs(velMatrix[n,i]-velMatrix[n,i-1])<200 or \
                            abs(velMatrix[n,i]-velMatrix[n+1,i-1])<200):


                             #Check neighbour beam for gradient drift
                             if (abs(velMatrix[n,i]-velMatrix[n+2,i+1])>500 or \
                                abs(velMatrix[n,i]-velMatrix[n+3,i+1])>500) and \
                                (abs(velMatrix[n,i]-velMatrix[n+2,i-1])>500 or \
                                abs(velMatrix[n,i]-velMatrix[n+3,i-1])>500):

                                #If all requirements passes, return index of RFE
                                return n,i

    #If any condition fails, return None
    return None,None
```

Bibliography

Alfvèn, H. (1942), Existence of Electromagnetic-Hydrodynamic Waves, *Nature*, *150*(3805), 405–406, doi:10.1038/150405d0.

Angelopoulos, V., W. Baumjohann, C. F. Kennel, F. V. Coroniti, M. G. Kivelson, R. Pellat, R. J. Walker, H. Lühr, and G. Paschmann (1992), Bursty bulk flows in the inner central plasma sheet, *Journal of Geophysical Research*, *97*(A4), 4027, doi:10.1029/91JA02701.

Arnoldy, R. L. (1974), Auroral particle precipitation and Birkeland Currents, *Reviews of Geophysics*, *12*(2), 217, doi:10.1029/RG012i002p00217.

Bahcivan, H., R. Tsunoda, M. Nicolls, and C. Heinselman (2010), Initial ionospheric observations made by the new Resolute incoherent scatter radar and comparison to solar wind IMF, *Geophysical Research Letters*, *37*(15), doi:10.1029/2010GL043632.

Baker, K. B., and S. Wing (1989), A new magnetic coordinate system for conjugate studies at high latitudes, *Journal of Geophysical Research*, *94*(A7), 9139, doi:10.1029/JA094iA07p09139.

Baker, K. B., J. R. Dudeney, R. A. Greenwald, M. Pinnock, P. T. Newell, A. S. Rodger, N. Mattin, and C.-I. Meng (1995), HF radar signatures of the cusp and low-latitude boundary layer, *Journal of Geophysical Research*, *100*(A5), 7671, doi:10.1029/94JA01481.

Balan, N., G. J. Bailey, B. Jenkins, P. B. Rao, and R. J. Moffett (1994), Variations of ionospheric ionization and related solar fluxes during an intense solar cycle, *Journal of Geophysical Research*, *99*(A2), 2243, doi:10.1029/93JA02099.

Barthes, L., R. Andre, J.-C. Cerisier, and J.-P. Villain (1998), Separation of multiple echoes using a high-resolution spectral analysis for SuperDARN HF radars, *Radio Science*, *33*(4), 1005–1017, doi:10.1029/98RS00714.

Basu, S., et al. (1988), Simultaneous density and electric field fluctuation spectra associated with velocity shears in the auroral oval, *Journal of Geophysical Research*, *93*(A1), 115, doi:10.1029/JA093iA01p00115.

Baumjohann, W., and R. A. Treumann (1999), *Basic space plasma physics*, Imperial College Press, UK.

Baumjohann, W., G. Paschmann, and C. A. Cattell (1989), Average plasma properties in the central plasma sheet, *Journal of Geophysical Research: Space Physics*, *94*(A6), 6597–6606, doi:10.1029/JA094iA06p06597.

Berkey, F. T., L. L. Cogger, S. Ismail, and Y. Kamide (1976), Evidence for a correlation between Sun-aligned arcs and the interplanetary magnetic field direction, *Geophysical Research Letters*, *3*(3), 145–147, doi:10.1029/GL003i003p00145.

Birkeland, K. (1908), *The Norwegian aurora polaris expedition 1902-1903*, vol. 1, H. Aschelhoug & Company.

Boakes, P. D., S. E. Milan, G. A. Abel, M. P. Freeman, G. Chisham, B. Hubert, and T. Sotirelis (2008), On the use of IMAGE FUV for estimating the latitude of the open/closed magnetic field line boundary in the ionosphere, *Annales Geophysicae*, *26*(9), 2759–2769, doi:10.5194/angeo-26-2759-2008.

Brekke, A. (2013), *Physics of the Upper Polar Atmosphere*, Springer Atmospheric Sciences, Springer Berlin Heidelberg, Berlin, Heidelberg, doi:10.1007/978-3-642-27401-5.

Burch, J. L., and J. F. Drake (2009), Reconnecting Magnetic Fields: The huge amounts of energy released from the relinking of magnetic fields in outer space are both mysterious and potentially destructive, *Source: American Scientist*, *97*(5), 392–399.

Burch, J. L., M. J. D., and J. A. Slavin (1990), Dayside auroral particle acceleration mechanisms derived from dynamics explorer data., *Journal of geomagnetism and geoelectricity*, *42*(12), 1365–1378, doi:10.5636/jgg.42.1365.

Burch, J. L., T. E. Moore, R. B. Torbert, and B. L. Giles (2016), Magnetospheric Multiscale Overview and Science Objectives, *Space Science Reviews*, *199*(1-4), 5–21, doi:10.1007/s11214-015-0164-9.

Carlson, H. C., J. Moen, K. Oksavik, C. P. Nielsen, I. W. McCrea, T. R. Pedersen, and P. Gallop (2006), Direct observations of injection events of subauroral plasma into the polar cap, *Geophysical Research Letters*, *33*(5), L05,103, doi:10.1029/2005GL025230.

Carlson, H. C., T. Pedersen, S. Basu, M. Keskinen, and J. Moen (2007), Case for a new process, not mechanism, for cusp irregularity production, *Journal of Geophysical Research: Space Physics*, *112*(11), doi:10.1029/2007JA012384.

Chapman, S., and V. C. A. Ferraro (1931), A new theory of magnetic storms, *Journal of Geophysical Research*, *36*(2), 77, doi:10.1029/TE036i002p00077.

Chaston, C. C., C. W. Carlson, J. P. McFadden, R. E. Ergun, and R. J. Strangeway (2007), How important are dispersive Alfvén waves for auroral particle acceleration?, *Geophysical Research Letters*, *34*(7), L07,101, doi:10.1029/2006GL029144.

Chen, X.-C., D. A. Lorentzen, J. I. Moen, K. Oksavik, L. J. Baddeley, and M. Lester (2016), F region ionosphere effects on the mapping accuracy of SuperDARN HF radar echoes, *Radio Science*, *51*(5), 490–506, doi:10.1002/2016RS005957.

Chisham, G., M. Pinnock, and A. S. Rodger (2000), Poleward-moving HF radar flow bursts in the cusp: Transient changes in flow speed or direction?, *Geophysical Research Letters*, *27*(7), 919–922, doi:10.1029/1999GL010760.

Chisham, G., et al. (2007), A decade of the Super Dual Auroral Radar Network (SuperDARN): scientific achievements, new techniques and future directions, *Surveys in Geophysics*, *28*(1), 33–109, doi:10.1007/s10712-007-9017-8.

Christensen, A. B., et al. (2003), Initial observations with the Global Ultraviolet Imager (GUVI) in the NASA TIMED satellite mission, *Journal of Geophysical Research*, *108*(A12), 1451, doi:10.1029/2003JA009918.

Cousins, E. D. P., and S. G. Shepherd (2010), A dynamical model of high-latitude convection derived from SuperDARN plasma drift measurements, *Journal of Geophysical Research: Space Physics*, *115*(A12329), doi:10.1029/2010JA016017.

Cowley, S. W. H., and M. Lockwood (1992), Excitation and decay of solar wind-driven flows in the magnetosphere-ionosphere system, *Annales geophysicae*, *10*, 103–115.

Cowley, S. W. H., J. P. Morelli, and M. Lockwood (1991), Dependence of convective flows and particle precipitation in the high-latitude dayside ionosphere on the X and Y components of the interplanetary magnetic field, *Journal of Geophysical Research*, *96*(A4), 5557, doi:10.1029/90JA02063.

Crooker, N. U. (1992), Reverse convection, *Journal of Geophysical Research*, *97*(A12), 19,363, doi:10.1029/92JA01532.

Daglis, I. A. (2012), *Space storms and space weather hazards*, vol. 38, Springer Science & Business Media.

de Larquier, S., P. Ponomarenko, A. J. Ribeiro, J. M. Ruohoniemi, J. B. H. Baker, K. T. Sterne, and M. Lester (2013), On the spatial distribution of decameter-scale subauroral ionospheric irregularities observed by SuperDARN radars, *Journal of Geophysical Research: Space Physics*, *118*(8), 5244–5254, doi:10.1002/jgra.50475.

Dorelli, J. C., and A. Bhattacharjee (2009), On the generation and topology of flux transfer events, *Journal of Geophysical Research: Space Physics*, *114*(A6), doi:10.1029/2008JA013410.

Dungey, J. W. (1961), Interplanetary magnetic field and the auroral zones, *Physical Review Letters*, *6*(2), 47–48, doi:10.1103/PhysRevLett.6.47.

Escoubet, C. P., A. Masson, H. Laakso, and M. L. Goldstein (2015), Recent highlights from Cluster, the first 3-D magnetospheric mission, *Ann. Geophys*, *33*, 1221–1235, doi:10.5194/angeo-33-1221-2015.

Evans, D. S., and M. S. Greer (2000), *Polar Orbiting Environmental Satellite Space Environment Monitor-2: Instrument Description and Archive Data Documentation*, US Department of Commerce, National Oceanic and Atmospheric Administration, Oceanic and Atmospheric Research Laboratories, Space Environment Center.

Farley, D. T. (1972), Multiple-Pulse Incoherent-Scatter Correlation Function Measurements, *Radio Science*, *7*(6), 661–666, doi:10.1029/RS007i006p00661.

Farris, M. H., and C. T. Russell (1994), Determining the standoff distance of the bow shock: Mach number dependence and use of models, *Journal of Geophysical Research*, *99*(A9), 17,681, doi:10.1029/94JA01020.

Farrugia, C. J., P. E. Sandholt, N. C. Maynard, R. B. Torbert, and D. M. Ober (2003), Temporal variations in a four-sheet field-aligned current system and associated aurorae as observed during a Polar-ground magnetic conjunction in the midmorning sector, *Journal of Geophysical Research*, *108*(A6), 1230, doi:10.1029/2002JA009619.

Farrugia, C. J., et al. (2004), Pulsed flows at the high-altitude cusp poleward boundary, and associated ionospheric convection and particle signatures, during a Cluster - FAST - SuperDARN-Søndrestrøm conjunction under a southwest IMF, *Annales Geophysicae*, *22*(8), 2891–2905, doi:10.5194/angeo-22-2891-2004.

Fasel, G. J. (1995), Dayside poleward moving auroral forms: A statistical study, *Journal of Geophysical Research*, *100*(A7), 11,891, doi:10.1029/95JA00854.

Fear, R., S. Milan, R. Maggiolo, A. Fazakerley, I. Dandouras, and S. Mende (2014), Direct observation of closed magnetic flux trapped in the high-latitude magnetosphere, *Science*, *346*(6216), 1506–1510.

Fear, R. C., and S. E. Milan (2012a), Ionospheric flows relating to transpolar arc formation, *Journal of Geophysical Research: Space Physics*, *117*(A9), doi:10.1029/2012JA017830.

Fear, R. C., and S. E. Milan (2012b), The IMF dependence of the local time of transpolar arcs: Implications for formation mechanism, *Journal of Geophysical Research: Space Physics*, *117*(A3), doi:10.1029/2011JA017209.

Feldman, U., E. Landi, and N. A. Schwadron (2005), On the sources of fast and slow solar wind, *Journal of Geophysical Research*, *110*(A7), A07,109, doi:10.1029/2004JA010918.

Frank, L. A., and J. D. Craven (1988), Imaging results from Dynamics Explorer 1, *Reviews of Geophysics*, *26*(2), 249, doi:10.1029/RG026i002p00249.

Frank, L. A., J. D. Craven, J. L. Burch, and J. D. Winningham (1982), Polar views of the Earth's aurora with Dynamics Explorer, *Geophysical Research Letters*, *9*(9), 1001–1004, doi:10.1029/GL009i009p01001.

Friis-Christensen, E., H. Lühr, and G. Hulot (2006), Swarm: A constellation to study the Earth's magnetic field, *Earth, Planets and Space*, *58*(4), 351–358, doi:10.1186/BF03351933.

Galand, M., and D. Evans (2000), Radiation damage ofthe proton meped detector on poes (tiros/noaa) satellites, *NOAA Technical Report OAR 456-SEC 42*.

Gosling, J. T., M. F. Thomsen, S. J. Bame, R. C. Elphic, and C. T. Russell (1991), Observations of reconnection of interplanetary and lobe magnetic field lines at the high-latitude magnetopause, *Journal of Geophysical Research: Space Physics*, *96*(A8), 14,097–14,106, doi:10.1029/91JA01139.

Greenwald, R. A., K. B. Baker, R. A. Hutchins, and C. Hanuise (1985), An HF phased-array radar for studying small-scale structure in the high-latitude ionosphere, *Radio Science*, *20*(1), 63–79, doi:10.1029/RS020i001p00063.

Greenwald, R. A., et al. (1995), DARN/SuperDARN, *Space Science Reviews*, *71*(1-4), 761–796, doi:10.1007/BF00751350.

Greenwald, R. A., K. Oksavik, R. Barnes, J. M. Ruohoniemi, J. Baker, and E. R. Talaat (2008), First radar measurements of ionospheric electric fields at sub-second temporal resolution, *Geophysical Research Letters*, *35*(3), L03,111, doi:10.1029/2007GL032164.

Heelis, R. A. (1984), The effects of interplanetary magnetic field orientation on dayside high-latitude ionospheric convection, *Journal of Geophysical Research*, *89*(A5), 2873, doi:10.1029/JA089iA05p02873.

Heppner, J. P., and N. C. Maynard (1987), Empirical high-latitude electric field models, *Journal of*, *92*, 4467–4489, doi:10.1029/JA092iA05p04467.

Iijima, T., and T. A. Potemra (1976), Field-aligned currents in the dayside cusp observed by Triad, *Journal of Geophysical Research*, *81*(34), 5971–5979, doi:10.1029/JA081i034p05971.

Imber, S. M., S. E. Milan, and B. Hubert (2006), The auroral and ionospheric flow signatures of dual lobe reconnection, *Annales Geophysicae*, *24*(11), 3115–3129, doi:10.5194/angeo-24-3115-2006.

Imber, S. M., S. E. Milan, and M. Lester (2013), Solar cycle variations in polar cap area measured by the superDARN radars, *Journal of Geophysical Research: Space Physics*, *118*(10), 6188–6196, doi:10.1002/jgra.50509.

Jackel, B. J., B. McKiernan, and H. J. Singer (2012), Geostationary magnetic field response to solar wind pressure variations: Time delay and local time variation, *Journal of Geophysical Research: Space Physics*, *117*(A5), doi:10.1029/2011JA017210.

Jacobsen, K. S., et al. (2009), THEMIS observations of extreme magnetopause motion caused by a hot flow anomaly, *Journal of Geophysical Research: Space Physics*, *114*(A8), doi:10.1029/2008JA013873.

Jacobsen, K. S., J. I. Moen, and A. Pedersen (2010), Quasistatic electric field structures and field-aligned currents in the polar cusp region, *Journal of Geophysical Research: Space Physics*, *115*(A10), doi:10.1029/2010JA015467.

Johnson, C. Y. (1969), Ion and neutral composition of the ionosphere., *Annals of the IQSY*, *5*, 197–213.

Karlson, K. A., M. Øieroset, J. Moen, and P. E. Sandholt (1996), A statistical study of flux transfer event signatures in the dayside aurora: The IMF By-related prenoon-postnoon symmetry, *Journal of Geophysical Research: Space Physics*, *101*(A1), 59–68, doi:10.1029/95JA02590.

Kelley, M. C. (2009), *The earth's ionosphere : plasma physics and electrodynamics*, 556 pp., Academic Press.

King, J. H., and N. E. Papitashvili (2005), Solar wind spatial scales in and comparisons of hourly Wind and ACE plasma and magnetic field data, *Journal of Geophysical Research*, *110*(A2), A02,104, doi:10.1029/2004JA010649.

Kivelson, M. G. M. G., and C. T. C. T. Russell (1995), *Introduction to space physics*, 568 pp., Cambridge University Press.

Koustov, A. V., K. N. Yakymenko, and P. V. Ponomarenko (2017), Seasonal effect for polar cap sunward plasma flows at strongly northward IMF Bz, *Journal of Geophysical Research: Space Physics*, *122*(2), 2530–2541, doi:10.1002/2016JA023556.

Laundal, K. M., and A. D. Richmond (2016), Magnetic Coordinate Systems, *Space Science Reviews*, pp. 1–33, doi:10.1007/s11214-016-0275-y.

Le, G., J. A. Slavin, and R. J. Strangeway (2010), Space Technology 5 observations of the imbalance of regions 1 and 2 field-aligned currents and its implication to the cross-polar cap Pedersen currents, *Journal of Geophysical Research: Space Physics*, *115*(A7), doi:10.1029/2009JA014979.

Lester, M., S. E. Milan, G. Provan, and J. A. Wild (2006), Review of Ionospheric Effects of Solar Wind Magnetosphere Coupling in the Context of the Expanding Contracting Polar Cap Boundary Model, *Space Science Reviews*, *124*(117), 117–130, doi:10.1007/s11214-006-9132-8.

Lin, C., and R. Hoffman (1982), Observations of inverted-V electron precipitation, *Space Science Reviews*, *33*(4), 415–457, doi:10.1007/BF00212420.

Liu, J., H. Hu, D. Han, H. Yang, and M. Lester (2015), Simultaneous ground-based optical and SuperDARN observations of the shock aurora at MLT noon, *Earth, Planets and Space*, *67*(1), 120, doi:10.1186/s40623-015-0291-2.

Lockwood, M., P. Sandholt, A. Farmer, S. Cowley, B. Lybekk, and V. Davda (1990), Auroral and plasma flow transients at magnetic noon, *Planetary and Space Science*, *38*(8), 973–993, doi:10.1016/0032-0633(90)90043-P.

Lockwood, M., J. Moen, S. W. H. Cowley, A. D. Farmer, U. P. Løvhaug, H. Lühr, and V. N. Davda (1993), Variability of dayside convection and motions of the cusp/cleft aurora, *Geophysical Research Letters*, *20*(11), 1011–1014, doi:10.1029/93GL00846.

Lockwood, M., S. E. Milan, T. Onsager, C. H. Perry, J. A. Scudder, C. T. Russell, and M. Brittnacher (2001), Cusp ion steps, field-aligned currents and poleward moving auroral forms, *Journal of Geophysical Research: Space Physics*, *106*(A12), 29,555–29,569, doi:10.1029/2000JA900175.

Lofthus, A., and P. H. Krupenie (1977), The spectrum of molecular nitrogen, *Journal of Physical and Chemical Reference Data*, *6*(1), 113–307, doi:10.1063/1.555546.

Lorentzen, D. A., C. S. Deehr, J. I. Minow, R. W. Smith, H. C. Stenbaek-Neielsen, F. Sigernes, R. L. Arnoldy, and K. Lynch (1996), SCIFER-Dayside auroral signatures of magnetospheric energetic electrons, *Geophysical Research Letters*, *23*(14), 1885–1888, doi:10.1029/96GL00593.

Lorentzen, D. A., J. Moen, K. Oksavik, F. Sigernes, Y. Saito, and M. G. Johnsen (2010), In situ measurement of a newly created polar cap patch, *Journal of Geophysical Research: Space Physics*, *115*(A12), doi:10.1029/2010JA015710.

Lühr, H., J. Park, J. W. Gjerloev, J. Rauberg, I. Michaelis, J. M. G. Merayo, and P. Brauer (2015), Field-aligned currents' scale analysis performed with the Swarm constellation, *Geophysical Research Letters*, *42*(1), 1–8, doi:10.1002/2014GL062453.

Lyons, L. R., et al. (2011), Possible connection of polar cap flows to pre- and post-substorm onset PBIs and streamers, *Journal of Geophysical Research: Space Physics*, *116*(A12), doi:10.1029/2011JA016850.

McCrea, I., et al. (2015), The science case for the EISCAT_3D radar, *Progress in Earth and Planetary Science*, *2*(1), 21, doi:10.1186/s40645-015-0051-8.

McWilliams, K. A., T. K. Yeoman, and G. Provan (2000), A statistical survey of dayside pulsed ionospheric flows as seen by the CUTLASS Finland HF radar, *Annales Geophysicae*, *18*(4), 445–453, doi:10.1007/s00585-000-0445-8.

Meier, R. R. (1991), Ultraviolet spectroscopy and remote sensing of the upper atmosphere, *Space Science Reviews*, *58*(1), 1–185, doi:10.1007/BF01206000.

Mende, S., et al. (2000), Far ultraviolet imaging from the image spacecraft: 1. system design, in *The Image Mission*, pp. 243–270, Springer.

Milan, S. E., T. K. Yeoman, M. Lester, E. C. Thomas, and T. B. Jones (1997), Initial backscatter occurrence statistics from the CUTLASS HF radars, *Annales Geophysicae*, *15*(6), 703–718, doi:10.1007/s00585-997-0703-0.

Milan, S. E., M. Lester, S. W. H. Cowley, and M. Brittnacher (2000), Convection and auroral response to a southward turning of the IMF: Polar UVI, CUTLASS, and IMAGE signatures of transient magnetic flux transfer at the magnetopause, *J. Geophys. Res.*, *105*(A7), 15,741–15,755, doi:10.1029/2000JA900022.

Milan, S. E., M. Lester, S. W. H. Cowley, K. Oksavik, M. Brittnacher, R. A. Greenwald, G. Sofko, and J.-P. Villain (2003), Variations in the polar cap area during two substorm cycles, *Annales Geophysicae*, *21*(5), 1121–1140, doi:10.5194/angeo-21-1121-2003.

Milan, S. E., B. Hubert, and A. Grocott (2005), Formation and motion of a transpolar arc in response to dayside and nightside reconnection, *Journal of Geophysical Research*, *110*(A1), A01,212, doi:10.1029/2004JA010835.

Moen, J., P. E. Sandholt, M. Lockwood, W. F. Denig, U. P. Løvhaug, B. Lybekk, A. Egeland, D. Opsvik, and E. Friis-Christensen (1995), Events of enhanced convection and related dayside auroral activity, *Journal of Geophysical Research*, *100*(A12), 23,917, doi:10.1029/95JA02585.

Moen, J., D. Evans, H. C. Carlson, and M. Lockwood (1996), Dayside moving auroral transients related to LLBL dynamics, *Geophysical Research Letters*, *23*(22), 3247–3250, doi:10.1029/96GL02766.

Moen, J., H. C. Carlson, and P. E. Sandholt (1999), Continuous observation of cusp auroral dynamics in response to an IMF By polarity change, *Geophysical Research Letters*, *26*(9), 1243–1246, doi:10.1029/1999GL900224.

Moen, J., H. C. Carlson, S. E. Milan, N. Shumilov, B. Lybekk, P. E. Sandholt, and M. Lester (2000), On the collocation between dayside auroral activity and coherent HF radar backscatter, *Annales Geophysicae*, *18*(12), 1531–1549, doi:10.1007/s00585-001-1531-2.

Moen, J., I. K. Walker, L. Kersley, and S. E. Milan (2002), On the generation of cusp HF backscatter irregularities, *Journal of Geophysical Research*, *107*(A4), 1044, doi:10.1029/2001JA000111.

Moen, J., M. Lockwood, K. Oksavik, H. C. Carlson, W. F. Denig, A. P. Van Eyken, and I. W. Mccrea (2004), The dynamics and relationships of precipitation, temperature and convection boundaries in the dayside auroral ionosphere, *Annales Geophysicae*, *22*, 1432–576.

Moen, J., Y. Rinne, H. C. Carlson, K. Oksavik, R. Fujii, and H. Opgenoorth (2008), Flow channels in the winter cusp/cleft ionosphere, *Journal of Geophysical Research: Space Physics*, *113*(9), doi:10.1029/2008JA013061.

Moen, J., H. Carlson, Y. Rinne, and Å. Skjæveland (2012), Multi-scale features of solar terrestrial coupling in the cusp ionosphere, *Journal of Atmospheric and Solar-Terrestrial Physics*, *87-88*, 11–19, doi:10.1016/j.jastp.2011.07.002.

Moore, T. E., M. Lockwood, M. O. Chandler, J. H. Waite, C. R. Chappell, A. Persoon, and M. Sugiura (1986), Upwelling O+ ion source characteristics, *Journal of Geophysical Research*, *91*(A6), 7019, doi:10.1029/JA091iA06p07019.

Nagai, T., et al. (1998), Structure and dynamics of magnetic reconnection for substorm onsets with Geotail observations, *Journal of Geophysical Research: Space Physics*, *103*(A3), 4419–4440, doi:10.1029/97JA02190.

Nakamura, R., W. Baumjohann, R. Schödel, M. Brittnacher, V. A. Sergeev, M. Kubyshkina, T. Mukai, and K. Liou (2001), Earthward flow bursts, auroral streamers, and small expansions, *Journal of Geophysical Research: Space Physics*, *106*(A6), 10,791–10,802, doi:10.1029/2000JA000306.

Newell, P. T. (2000), Reconsidering the inverted-V particle signature: Relative frequency of large-scale electron acceleration events, *Journal of Geophysical Research: Space Physics*, *105*(A7), 15,779–15,794, doi:10.1029/1999JA000051.

Nishimura, Y., L. R. Lyons, V. Angelopoulos, T. Kikuchi, S. Zou, and S. B. Mende (2011), Relations between multiple auroral streamers, pre-onset thin arc formation, and substorm auroral onset, *Journal of Geophysical Research: Space Physics*, *116*(A9), doi:10.1029/2011JA016768.

Oksavik, K., J. Moen, and H. C. Carlson (2004), High-resolution observations of the small-scale flow pattern associated with a poleward moving auroral form in the cusp, *Geophysical Research Letters*, *31*(11), 11,807, doi:10.1029/2004GL019838.

Oksavik, K., J. Moen, H. C. Carlson, R. a. Greenwald, S. E. Milan, M. Lester, W. F. Denig, and R. J. Barnes (2005), Multi-instrument mapping of the small-scale flow dynamics related to a cusp auroral transient, *Annales Geophysicae*, *23*(2000), 2657–2670, doi:10.5194/angeo-23-2657-2005.

Oksavik, K., J. I. Moen, E. H. Rekaa, H. C. Carlson, and M. Lester (2011), Reversed flow events in the cusp ionosphere detected by SuperDARN HF radars, *Journal of Geophysical Research: Space Physics*, *116*(12), 1–12, doi:10.1029/2011JA016788.

Oksavik, K., J. Moen, M. Lester, T. A. Bekkeng, and J. K. Bekkeng (2012), In situ measurements of plasma irregularity growth in the cusp ionosphere, *Journal of Geophysical Research: Space Physics*, *117*(A11), doi:10.1029/2012JA017835.

Østgaard, N., S. B. Mende, H. U. Frey, and J. B. Sigwarth (2005), Simultaneous imaging of the reconnection spot in the opposite hemispheres during northward IMF, *Geophysical Research Letters*, *32*(21), doi:10.1029/2005GL024491.

Parker, E. N. (1958), Dynamics of the Interplanetary Gas and Magnetic Fields., *The Astrophysical Journal*, *128*, 664, doi:10.1086/146579.

Paschmann, G., G. Haerendel, I. Papamastorakis, N. Sckopke, S. J. Bame, J. T. Gosling, and C. T. Russell (1982), Plasma and magnetic field characteristics of magnetic flux transfer events, *Journal of Geophysical Research*, *87*(A4), 2159, doi:10.1029/JA087iA04p02159.

Paxton, L. J., et al. (1992), Special sensor ultraviolet spectrographic imager: an instrument description, *Instrumentation for Planetary and Terrestrial Atmospheric Remote Sensing, 2*, pp. 2–15, doi:10.1117/12.60595.

Pinnock, M., A. S. Rodger, J. R. Dudeney, K. B. Baker, P. T. Neweli, R. A. Greenwald, and M. E. Greenspan (1993), Observations of an Enhanced Convection Channel in the Cusp Ionosphere, *J Geophys Res-Space Phys*, *98*(A3), 3767–3776, doi:10.1029/92JA01382.

Pinnock, M., A. S. Rodger, J. R. Dudeney, F. Rich, and K. B. Baker (1995), High spatial and temporal resolution observations of the ionospheric cusp, *Annales Geophysicae*, *13*(9), 919–925, doi:10.1007/s00585-995-0919-9.

Pitkänen, T., A. T. Aikio, and L. Juusola (2013), Observations of polar cap flow channel and plasma sheet flow bursts during substorm expansion, *Journal of Geophysical Research: Space Physics*, *118*(2), 774–784, doi:10.1002/jgra.50119.

Pollock, C. J., M. O. Chandler, T. E. Moore, J. H. Waite, C. R. Chappell, and D. A. Gurnett (1990), A survey of upwelling ion event characteristics, *Journal of Geophysical Research*, *95*(A11), 18,969, doi:10.1029/JA095iA11p18969.

Ponomarenko, P. V., and C. L. Waters (2006), Spectral width of SuperDARN echoes: measurement, use and physical interpretation, *Annales Geophysicae*, *24*(1), 115–128, doi:10.5194/angeo-24-115-2006.

Provan, G., and T. K. Yeoman (1999), Statistical observations of the MLT, latitude and size of pulsed ionospheric flows with the CUTLASS Finland radar, *Annales Geophysicae*, *17*(7), 855–867, doi:10.1007/s00585-999-0855-1.

Provan, G., T. K. Yeoman, and S. E. Milan (1998), CUTLASS Finland radar observations of the ionospheric signatures of flux transfer events and the resulting plasma flows, *Annales Geophysicae*, *16*(11), 1411–1422, doi:10.5194/angeo-16-1411-1998.

Provan, G., S. E. Milan, M. Lester, T. K. Yeoman, and H. Khan (2002), Simultaneous observations of the ionospheric footprint of flux transfer events and dispersed ion signatures, *Annales Geophysicae*, *20*(2), 281–287.

Reiff, P. H., and J. L. Burch (1985), IMF By-dependent plasma flow and Birkeland currents in the dayside magnetosphere: 2. A global model for northward and southward IMF, *Journal of Geophysical Research*, *90*(A2), 1595, doi:10.1029/JA090iA02p01595.

Ribeiro, A. J., J. M. Ruohoniemi, P. V. Ponomarenko, L. B. N. Clausen, J. B. H. Baker, R. A. Greenwald, K. Oksavik, and S. de Larquier (2013), A comparison of SuperDARN ACF fitting methods, *Radio Science*, *48*(3), 274–282, doi:10.1002/rds.20031.

Rietveld, M. T., P. N. Collis, and J.-P. St.-Maurice (1991), Naturally enhanced ion acoustic waves in the auroral ionosphere observed with the EISCAT 933-MHz radar, *Journal of Geophysical Research*, *96*(A11), 19,291, doi:10.1029/91JA01188.

Rinne, Y., J. Moen, K. Oksavik, and H. C. Carlson (2007), Reversed flow events in the winter cusp ionosphere observed by the European Incoherent Scatter (EISCAT) Svalbard radar, *Journal of Geophysical Research: Space Physics*, *112*(10), doi:10.1029/2007JA012366.

Rinne, Y., J. Moen, H. C. Carlson, and M. R. Hairston (2010), Stratification of east-west plasma flow channels observed in the ionospheric cusp in response to IMF By polarity changes, *Geophysical Research Letters*, *37*(13), doi:10.1029/2010GL043307.

Ritter, P., H. Lühr, and J. Rauberg (2013), Determining field-aligned currents with the Swarm constellation mission, *Earth, Planets and Space*, *65*(11), 1285–1294, doi:10.5047/eps.2013.09.006.

Roberts, P. H., et al. (2013), On the genesis of the Earth's magnetism, *Reports on Progress in Physics*, *76*(9), 096,801, doi:10.1088/0034-4885/76/9/096801.

Ruohoniemi, J. M., and K. B. Baker (1998), Large-scale imaging of high-latitude convection with Super Dual Auroral Radar Network HF radar observations, *Journal of Geophysical Research: Space Physics*, *103*(A9), 20,797–20,811, doi:10.1029/98JA01288.

Ruohoniemi, J. M., and R. A. Greenwald (2005), Dependencies of high-latitude plasma convection: Consideration of interplanetary magnetic field, seasonal, and universal time factors in statistical patterns, *Journal of Geophysical Research: Space Physics*, *110*(A9), doi:10.1029/2004JA010815.

Russell, C. (1971), *"Geophysical Coordinate Transformations"*, vol. 2, pp. 184–196, D. Reidel, Publishing Company Dordrecht-Holland.

Russell, C., and R. Elphic (1978), Initial ISEE magnetometer results: magnetopause observations, *Space Science Reviews*, *22*(6), 681–715, doi:10.1007/BF00212619.

Russell, C. T. (1993), Magnetic fields of the terrestrial planets, *Journal of Geophysical Research*, *98*(E10), 18,681, doi:10.1029/93JE00981.

Sandanger, M. I., L.-K. G. Ødegaard, H. Nesse Tyssøy, J. Stadsnes, F. Søraas, K. Oksavik, and K. Aarsnes (2015), In-flight calibration of NOAA POES proton detectors-Derivation of the MEPED correction factors, *Journal of Geophysical Research: Space Physics*, *120*(11), 9578–9593, doi:10.1002/2015JA021388.

Sandholt, P. E., and C. J. Farrugia (2007), Role of poleward moving auroral forms in the dawn-dusk auroral precipitation asymmetries induced by IMF B y, *Journal of Geophysical Research: Space Physics*, *112*(A04203), doi:10.1029/2006JA011952.

Sandholt, P. E., and P. T. Newell (1992), Ground and satellite observations of an auroral event at the cusp/cleft equatorward boundary, *Journal of Geophysical Research*, *97*(A6), 8685, doi:10.1029/91JA02995.

Sandholt, P. E., M. Lockwood, T. Oguti, S. W. H. Cowley, K. S. C. Freeman, B. Lybekk, A. Egeland, and D. M. Willis (1990), Midday Auroral Breakup Events and Related Energy and Momentum Transfer from the Magnetosheath, *Journal of Geophysical Research*, *95*(A2), 1039–1060, doi:10.1029/JA095iA02p01039.

Sandholt, P. E., C. J. Farrugia, J. Moen, Ø. Noraberg, B. Lybekk, T. Sten, and T. Hansen (1998), A classification of dayside auroral forms and activities as a function of interplanetary magnetic field orientation, *Journal of Geophysical Research: Space Physics*, *103*(A10), 23,325–23,345, doi:10.1029/98JA02156.

Sandholt, P. E., C. J. Farrugia, and W. F. Denig (2004), Detailed dayside auroral morphology as a function of local time for southeast IMF orientation: implications for solar wind-magnetosphere coupling, *Annales Geophysicae*, *22*, 3537–3560.

Sandholt, P. E., Y. Andalsvik, and C. J. Farrugia (2010), Polar cap flow channel events: spontaneous and driven responses, *Ann. Geophys*, *28*, 2015–2025, doi:10.5194/angeo-28-2015-2010.

Schwartz, S. J., et al. (1985), An active current sheet in the solar wind, *Nature*, *318*(6043), 269–271, doi:10.1038/318269a0.

Senior, C., J.-C. Cerisier, F. Rich, M. Lester, and G. K. Parks (2002), Strong sunward propagating flow bursts in the night sector during quiet solar wind conditions: SuperDARN and satellite observations, *Annales Geophysicae*, *20*(6), 771–779, doi:10.5194/angeo-20-771-2002.

Sergeev, V. A., V. Angelopoulos, J. T. Gosling, C. A. Cattell, and C. T. Russell (1996), Detection of localized, plasma-depleted flux tubes or bubbles in the midtail plasma sheet, *Journal of Geophysical Research: Space Physics*, *101*(A5), 10,817–10,826, doi:10.1029/96JA00460.

Sergeev, V. A., K. Liou, P. T. Newell, S.-I. Ohtani, M. R. Hairston, and F. Rich (2004), Auroral streamers: characteristics of associated precipitation,convection and field-aligned currents, *Annales Geophysicae*, *22*(2), 537–548, doi:10.5194/angeo-22-537-2004.

Shelley, E. G., R. D. Sharp, and R. G. Johnson (1976), Satellite observations of an ionospheric acceleration mechanism, *Geophysical Research Letters*, *3*(11), 654–656, doi:10.1029/GL003i011p00654.

Shepherd, S. G. (2014), Altitude-adjusted corrected geomagnetic coordinates: Definition and functional approximations, *Journal of Geophysical Research: Space Physics*, *119*(9), 7501–7521, doi:10.1002/2014JA020264.

Sibeck, D. G., N. B. Trivedi, E. Zesta, R. B. Decker, H. J. Singer, A. Szabo, H. Tachihara, and J. Watermann (2003), Pressure-pulse interaction with the magnetosphere and ionosphere, *Journal of Geophysical Research: Space Physics*, *108*(A2), doi:10.1029/2002JA009675.

Smith, C. W., J. L'Heureux, N. F. Ness, M. H. Acuna, L. F. Burlaga, and J. Scheifele (1998), The ace magnetic fields experiment, in *The Advanced Composition Explorer Mission*, pp. 613–632, Springer.

Southwood, D. J. (1987), The ionospheric signature of flux transfer events, *Journal of Geophysical Research*, *92*(A4), 3207, doi:10.1029/JA092iA04p03207.

Stasiewicz, K., et al. (2000), Small Scale Alfvenic Structure in the Aurora, *Space Science Reviews*, *92*(3/4), 423–533, doi:10.1023/A:1005207202143.

Stausland, C. T. (2014), On the flow shear instability driven by reversed flow events in the polar ionosphere, Master's thesis, University of Oslo.

Stern, D. P. (1984), Magnetospheric dynamo processes, in *Magnetospheric Currents*, edited by T. A. Potemra, pp. 200–207, American Geophysical Union, doi:10.1029/GM028p0200.

Stone, E., A. Frandsen, R. Mewaldt, E. Christian, D. Margolies, J. Ormes, and F. Snow (1998), The Advanced Composition Explorer, *Space Science Reviews*, *86*(1/4), 1–22, doi:10.1023/A:1005082526237.

Störmer, C. (1955), *The polar aurora*, Clarendon Press.

Strickland, D. J., et al. (2004), Solar EUV irradiance variability derived from terrestrial far ultraviolet dayglow observations, *Geophysical Research Letters*, *31*(3), L03,801, doi:10.1029/2003GL018415.

Summons, R. E., et al. (2011), Preservation of Martian Organic and Environmental Records: Final Report of the Mars Biosignature Working Group, *Astrobiology*, *11*(2), 157–181, doi:10.1089/ast.2010.0506.

Sweet, P. A. (1958), 14. the neutral point theory of solar flares, in *Symposium-International Astronomical Union*, vol. 6, pp. 123–134, Cambridge Univ Press.

Thébault, E., et al. (2015), International Geomagnetic Reference Field: the 12th generation, *Earth, Planets and Space*, *67*(79), doi:10.1186/s40623-015-0228-9.

Thomsen, M. F., J. T. Gosling, S. A. Fuselier, S. J. Bame, and C. T. Russell (1986), Hot, diamagnetic cavities upstream from the Earth's bow shock, *Journal of Geophysical Research*, *91*(A3), 2961, doi:10.1029/JA091iA03p02961.

Trenchi, L., R. C. Fear, K. J. Trattner, B. Mihaljcic, and A. N. Fazakerley (2016), A sequence of flux transfer events potentially generated by different generation mechanisms, *Journal of Geophysical Research: Space Physics*, *121*(9), 8624–8639, doi:10.1002/2016JA022847.

Tsunoda, R. T. (1988), High-latitude F region irregularities: A review and synthesis, *Reviews of Geophysics*, *26*(4), 719, doi:10.1029/RG026i004p00719.

van Eyken, A. P., H. Rishbeth, D. M. Willis, and S. W. H. Cowley (1984), Initial EISCAT observations of plasma convection at invariant latitudes 70-77, *Journal of Atmospheric and Terrestrial Physics*, *46*(6-7), 635–641, doi:10.1016/0021-9169(84)90081-3.

Volland, H. (1978), A model of the magnetospheric electric convection field, *Journal of Geophysical Research*, *83*(A6), 2695, doi:10.1029/JA083iA06p02695.

Vorobjev, V., G. Gustafsson, G. Starkov, Y. Feldstein, and N. Shevnina (1975), Dynamics of day and night aurora during substorms, *Planetary and Space Science*, *23*(2), 269–278, doi:10.1016/0032-0633(75)90132-4.

Wang, Y. L., R. C. Elphic, B. Lavraud, M. G. G. T. Taylor, J. Birn, C. T. Russell, J. Raeder, H. Kawano, and X. X. Zhang (2006), Dependence of flux transfer events on solar wind conditions from 3 years of Cluster observations, *Journal of Geophysical Research*, *111*(A4), A04,224, doi:10.1029/2005JA011342.

Weimer, D. R. (1995), Models of high-latitude electric potentials derived with a least error fit of spherical harmonic coefficients, *Journal of Geophysical Research*, *100*(A10), 19,595, doi:10.1029/95JA01755.

Wild, J. A., et al. (2001), First simultaneous observations of flux transfer events at the high-latitude magnetopause by the Cluster spacecraft and pulsed radar signatures in the conjugate ionosphere by the CUTLASS and EISCAT radars, *Annales Geophysicae*, *19*(10/12), 1491–1508.

Yeoman, T. K., D. M. Wright, A. J. Stocker, and T. B. Jones (2001), An evaluation of range accuracy in the Super Dual Auroral Radar Network over-the-horizon HF radar systems, *Radio Science*, *36*(4), 801–813, doi:10.1029/2000RS002558.

Young, J. A., C. P. Malone, P. V. Johnson, J. M. Ajello, X. Liu, and I. Kanik (2010), Lyman–Birge–Hopfield emissions from electron-impact excited N2, *Journal of Physics B: Atomic, Molecular and Optical Physics*, *43*(13), 135,201, doi:10.1088/0953-4075/43/13/135201.

Zhang, L. Q., W. Baumjohann, C. Wang, L. Dai, and B. B. Tang (2016), Bursty bulk flows at different magnetospheric activity levels: Dependence on IMF conditions, *Journal of Geophysical Research: Space Physics*, *121*(9), 8773–8789, doi:10.1002/2016JA022397.

Zmuda, A. (1971), The international geomagnetic reference field: Introduction, *Bull Int Assoc Geomag Aeronomy*, *28*, 148–152.